

**RF MEMS SWITCHES WITH NOVEL MATERIALS AND
MICROMACHINING TECHNIQUES FOR SOC/SOP RF
FRONT ENDS**

A Thesis
Presented to
The Academic Faculty

by

Guoan Wang

In Partial Fulfillment
of the Requirements for the Degree
Doctor of Philosophy

School of Electrical and Computer
Engineering
Georgia Institute of Technology
December 2006

**RF MEMS SWITCHES WITH NOVEL MATERIALS AND
MICROMACHINING TECHNIQUES FOR SOC/SOP RF
FRONT ENDS**

Approved by:

Dr. John Papapolymerou, Advisor
School of Electrical and Computer
Engineering
Georgia Institute of Technology

Dr. Joy Laskar
School of Electrical and Computer
Engineering
Georgia Institute of Technology

Dr. John Cressler
School of Electrical and Computer
Engineering
Georgia Institute of Technology

Dr. Cliff Henderson
School of Chemical and Biomecular
Engineering
Georgia Institute of Technology

Dr. Shyh-Chiang Shen
School of Electrical and Computer
Engineering
Georgia Institute of Technology

Date Approved: July 26, 2006

To my beloved family!

ACKNOWLEDGEMENTS

First, I would like to express my deepest gratitude to my advisor, Professor John Pappolymerou, for his support, faith, superb and patient guidance, helping me to complete my Ph.D. study. I am grateful for spending time under his mentorship, and his model role also help to shape my research attitude.

I would like to thank Professor Cliff Henderson for his guidance, support and help throughout my Ph.D. study. I would also like to thank Professor Joy Laskar and Professor Emmanouil Tentzeris for their help and support during my study at Georgia Tech.

I gratefully acknowledge all my committee members, including my advisor, Professor John Cressler, Professor Cliff Henderson, Professor Joy Laskar and Professor Shyh-Chiang Shen for their time and help serving as my defense committee.

For their generous assistance and help, I would like to thank all the cleanroom staff at Georgia Tech, their work maintaining the operation of the cleanroom is extremely important for my research.

I would like to thank Dr. Guizhen Zheng, Dr. Dane Thompson, Pete Kirby, Nickolas Kingsley, Matt Morton, Cesar Lugo, Bo Pan, Ramanan Bairavasubramanian, Symeon Nikolaou, Yuan Li, Steve Horst, David Chung, Boyon Kim and Dr. Dimitrios Anagnostou. I really appreciate their help and friendship, I have learned a lot from the numerous discussions with them on the research, culture and future. I thank all the friends met in the cleanroom, I really enjoyed the innumerable hours spent in the cleanroom.

I gratefully thank my parents for their love and care. I owe them a huge debt of gratitude for their selfless support and encouragement. I also like to thank my brothers and sisters for their support and help.

Last but not the least, I would like to thank my wonderful wife and lifelong friend, Zheng Xia, for her love, faith, support and encouragement. Without them, I could not have made it through my Ph.D. study.

TABLE OF CONTENTS

DEDICATION	iii
ACKNOWLEDGEMENTS	iv
LIST OF TABLES	viii
LIST OF FIGURES	ix
SUMMARY	xiv
LIST OF SYMBOLS OR ABBREVIATIONS	xiv
I INTRODUCTION	1
II FINITE GROUND COPLANAR LINES ON CMOS GRADE SILICON WITH A THICK EMBEDDED SILICON DIOXIDE LAYER USING MICROMACHINING TECHNIQUES	14
2.1 Background	14
2.2 Fabrication and Measurements	16
2.3 Results and Discussion	18
2.4 Conclusions	20
III RF MEMS SWITCHES WITH PHOTODEFINABLE MIXED METAL OXIDE DIELECTRICS	23
3.1 Introduction to RF MEMS Switch	23
3.2 RF MEMS Design	28
3.2.1 Mechanical Design of RF MEMS Switch	28
3.2.2 Electrical Design of RF MEMS Switch	32
3.3 RF MEMS Switch with Photodefinable Mixed Oxide Dielectrics	35
3.3.1 Motivation and Introduction	35
3.3.2 Characterization of Metal Oxide Dielectrics	39
3.3.3 Conclusions	57
IV RF MEMS SWITCH WITH LCP SUBSTRATE	58
4.1 Introduction	58
4.2 Properties of LCP	59
4.3 RF MEMS Switches using LCP Substrate	60

4.4	Measured Results	64
4.5	Conclusions	68
V	TUNABLE MEMS SWITCHES WITH BARIUM STRONTIUM TITANTATE (BST) DIELECTRICS	69
5.1	Introduction	69
5.2	Design and Fabrication	72
5.2.1	Deposition and Properties of BST Thin Film	72
5.2.2	Fabrication of the Switches	73
5.3	Results	79
5.4	Conclusions	80
VI	TEMPERATURE STUDY OF THE DIELECTRIC POLARIZATION EFFECTS OF CAPACITIVE RF-MEMS SWITCHES	81
6.1	Introduction	81
6.2	Theoretical Analysis	83
6.3	MEMS Switch Fabrication and Measurement	85
6.4	Results and Discussion	87
6.4.1	Capacitance-Voltage Characteristics	87
6.4.2	Capacitance Transients	92
6.5	Conclusions	95
VII	MICROWAVE APPLICATIONS WITH RF MEMS SWITCHES	96
7.1	Introduction	96
7.2	Reconfigurable Dual Frequency Antenna with RF MEMS Switches	97
7.2.1	Introduction	97
7.2.2	Design and Fabrication	100
7.2.3	Measured Results	101
7.3	Frequency and Bandwidth Tunable Filter with RF MEMS Switch and Ferroelectric Capacitors	104
7.3.1	Introduction	105
7.3.2	Design and Fabrication	106
7.3.3	Results and Discussion	110
7.4	Conclusions	113

REFERENCES **114**

LIST OF TABLES

1	Dimensions of fabricated FGC lines	19
2	Attenuation comparison between FGC lines on embedded silicon dioxide island and FGC lines on CMOS grade silicon substrate with polyimide interface layer [77]	20
3	Comparison of theoretical, simulated, and measured pulldown voltage . . .	36
4	Capacitance, Inductance and Resistance of the RF MEMS switches with different support design	36
5	Dimensions of fabricated parallel plate capacitors	46
6	Measured capacitance for different capacitors with mixed oxide dielectrics .	46
7	Measured capacitance for parallel plate capacitors with silicon nitride as dielectric layer	49
8	Summary of the measured breakdown voltage for mixed oxide dielectrics and silicon nitride	51
9	XPS atomic composition of the mixed metal oxide film after plasma treatment	51
10	Summary of the measured results for switches with mixed oxide dielectrics on the down state	53
11	Summary of the measured results for switches with silicon nitride dielectrics on the down state	54
12	Measured s-parameter summary for the switch on different substrates . . .	63
13	Fitted capacitances for the measured results of the switches.	67

LIST OF FIGURES

1	Developmental concept of a RF-MEMS-SOC/SOP based on the hybrid integration of the MEMS.	2
2	Typical RF MEMS "food chain".	3
3	Structure of a typical RF MEMS capacitive shunt switch.	3
4	The cross section of cantilever DC contact RF MEMS switches [130].	5
5	(a) University of Michigan low-height high-spring-constant gold MEMS switch and (b) low spring-constant MEMS switch [64, 70].	6
6	a) Analog Devices MEMS-series switch (Courtesy Analog Devices) [63] and (b) the University of Michigan MEMS series switch [64].	7
7	Approaches for the implementation of tunable capacitors.	9
8	Demonstration of MEMS package with top covered layer	12
9	Configurations of a reconfigurable antenna: Open Configuration (left) and Close configuration (right).	12
10	Coplanar waveguide on low resistivity Si with polyimide interface layer [77].	16
11	Cross-sectional view of the Finite Ground Coplanar (FGC) waveguide fabricated on thick oxide islands inside the silicon substrate.	16
12	Fabrication process flow of the FGC lines with embedded thick silicon dioxide islands.	17
13	Cross section of 50 μm thick silicon dioxide embedded in low resistivity silicon substrate.	18
14	Photo of the fabricated FGC lines.	18
15	Photo of the fabricated transmission line.	19
16	Measured S-parameters of FGC lines on silicon oxide islands with silicon substrates.	20
17	Comparison of the measured and simulated S-parameters of FGC line with the length of 4000 μm on silicon oxide islands with silicon substrates.	21
18	Measured attenuation of FGC lines on CMOS grade Si ($\rho=0.0057 \Omega\text{-cm}$) with embedded thick SiO_2 island.	22
19	Fabricated patch antenna on embedded silicon dioxide.	22
20	Physical structure and operation of electrostatic type RF MEMS airbridge switch (top) and cantilever switch (bottom).	24
21	Equivalent circuit model for airbridge switch (top) and cantilever switch (bottom).	25

22	A coplanar waveguide implementation of RF MEMS capacitive switch [128].	25
23	Operation of a RF MEMS switch.	28
24	Illustration of dimensions.	30
25	Switch designs with different support structure.	31
26	3D simulated deflection profile of RF MEMS switches.	32
27	SEM photos of fabricated switch for 50 - 90 GHz applications.	34
28	Close up view of a fabricated switch for 50 - 90 GHz applications.	35
29	Measured results for the switches with a different support design.	35
30	Molecular structure of a typical precursor.	37
31	Photo of a 1 μm wide line of the patterned thin film.	37
32	Traditional deposition approach of dielectric materials.	40
33	Schematic of process using photosensitive metal-organic compounds to produce patterned metal oxides.	40
34	Molecular structures of the titanium(n-butoxide) ₂ (2-ethylhexanoate) ₂ (top) and barium 2-ethylhexanoate used as photosensitive metal-organic compounds in this work to produce patterned mixed oxide structure.	41
35	The cantilever switch fabrication process flow.	41
36	Photo of direct photo-patterned mixed oxide thin film.	42
37	SEM photos of fabricated airbridge type switch with different support spring.	43
38	SEM photo of a fabricated cantilever switch.	44
39	Fabrication process flow for the parallel plate capacitors.	44
40	SEM photos of fabricated parallel plate capacitors with rectangular shape (top) and circular shape(bottom) made using the mixed oxide dielectric produced from a photosensitive metal-organic precursor solution.	45
41	I-V measurement results of parallel plate capacitors made with the mixed metal oxide dielectric which has been processed without an oxygen plasma treatment after exposure and development of the oxide pattern.	46
42	CV measured results for parallel plate capacitors with circular shape (top) and rectangular shape(bottom).	47
43	Comparison for the measured I-V characteristics of the parallel plate capacitors with different precursors and processing.	48
44	I-V measurement results of parallel plate capacitors made with the mixed metal oxide dielectric which has been processed with and without an oxygen plasma treatment after exposure and development of the oxide pattern.	49
45	I-V characteristics of the PPCs with silicon nitride as dielectric layer.	50

46	FTIR spectrum result of the metal oxide after plasma treatment.	50
47	EDS analysis results for the mixed oxide film.	52
48	Measured S-parameter results for switch with metal oxide as dielectrics at the UP state.	52
49	Measured S-parameter results for switch with solid hinge at the DOWN state.	53
50	Measured S-parameter results for switch with S-shape meander hinge at the DOWN state.	54
51	Measurement setup for the reliability test.	55
52	Response of the switch with s-shape meander hinge for the lifetime test. . .	55
53	Response of the switch with solid hinge for the lifetime test.	56
54	Modulus behavior of LCP with temperature.	61
55	Surface roughness of bare LCP substrate.	61
56	Surface roughness of LCP substrate coated with polyimide layer.	62
57	Surface roughness of polished LCP substrate.	63
58	Fabrication process of a switch on LCP substrate.	64
59	Patterned metal on bare LCP substrate.	65
60	Patterned metal on surface roughness improved LCP substrate.	65
61	Photos of fabricated switch on LCP/PI substrate (top) and polished LCP substrate (bottom).	66
62	Measured S-parameters of the fabricated switch as shown in Figure 55 on up state (top) and down state (bottom)	67
63	Reconfigurable antenna in terms of polarization with MEMS switches. . . .	70
64	Close-up view of a single BST MEMS switch.	71
65	RF tunable cantilever switch using BST thin film and separate actuation electrode in both switch up and down states.	72
66	Schematic representation of the CCVD system.	72
67	Fabrication process flow of BST MEMS switches.	74
68	Microscope photo of the patterned Pt layer using lift off process.	75
69	SEM of a fabricated Cantilever type CPW switch on sapphire with 200 nm BST layer and 1.2 μm thick Au membrane.	76
70	SEM Close-up view of membrane and BST area.	76
71	C-V Characteristic of the MEMS switch with BST dielectric layer at the down state.	77

72	Measured S-parameters of the cantilever BST MEMS switch at down-state position.	77
73	Measured S-parameters of the cantilever BST MEMS switch at up-state position.	78
74	S-parameter comparison between BST and SiN switches at down-state.	78
75	Simplified geometry of the switch structure and charging model [72].	83
76	SEM photo of MEMS switch used in this chapter.	86
77	Typical C-V characteristic of a capacitive MEMS switch at room temperature. The probe-station parasitic capacitance was about 2.8 pF [71].	87
78	Typical C-V characteristic of a capacitive MEMS switch at 340 K [71].	88
79	Typical C-V characteristic of a capacitive MEMS switch at 440 K [71].	89
80	Temperature dependence of the offset voltage obtained by ascending and descending the C-V characteristic [71].	90
81	The transient response of a capacitive MEMS switch upon the application of a positive actuation voltage of 20V at room temperature [71].	91
82	The transient response of a capacitive MEMS switch upon the application of a negative actuation voltage of 20V at room temperature [71].	91
83	Arrhenius plot of the time scale of the stretched exponential decay process [71].	94
84	Multilayer antenna architecture [3].	100
85	Dimension and side view of the antenna structure.	100
86	Schematics of the feeding network for both frequencies.	102
87	Pictures of the pattern on different layers before bonding.	103
88	Photo of the fabricated feeding network with MEMS switches.	103
89	Photo of a fabricated SPDT MEMS switch.	104
90	Measured S parameter for 14 GHz antenna array.	104
91	Measured S parameter for 35 GHz antenna array.	105
92	Schematics of the 2 pole (a) and 3 pole (b) filter design.	107
93	Cross section of a BST gap capacitor.	108
94	Fabrication process flow for the tunable filter with BST capacitors and MEMS switches.	109
95	Picture of a fabricated 2 pole filter.	110
96	Picture of a fabricated 3 pole filter.	110
97	Fabrication process flow for the tunable filter with BST capacitors and MEMS switches.	110

98	Measured results for the 2 pole filter(MEMS switch is on the Up position).	111
99	Measured results for the 2 pole filter(MEMS switch is on the Down position).	111
100	Measured results for the 3 pole filter(MEMS switch is on the Up position).	112
101	Measured results for the 3 pole filter(MEMS switch is on the Down position).	112

SUMMARY

This dissertation deals with the development of RF MEMS switches with novel materials and micromachining techniques for the RF and microwave applications. Research on several projects is presented. In the first project, Finite Ground Coplanar (FGC) waveguide transmission line on CMOS grade silicon wafer are studied; the second project and the third project investigated novel dielectric materials for RF MEMS switches. The second project is a low cost Radio Frequency (RF) Micro-electromechanical Systems (MEMS) switch using photo-definable mixed oxide dielectrics, and the third project developed RF MEMS switches on flexible Liquid Crystal Polymer (LCP) substrate to enable the implementation of multi-band and reconfigurable modules. The fourth project is focused on tunable RF MEMS switches using a Barium Strontium Titanate (BST) dielectric layer. In the fifth project, preliminary research on reliability considerations of MEMS switches are discussed and implemented, and the sixth project showed the implementation of several reconfigurable RF circuits with the developed RF MEMS capacitive switches in this dissertation.

In the first project, Finite Ground Coplanar (FGC) waveguide transmission lines on CMOS grade silicon wafer (<0.01 ohm-cm) with a thick embedded silicon oxide layer have been developed using micromachining techniques. Lines with different lengths were designed, fabricated and measured. Measured attenuation and s-parameters are presented in Chapter II. Results show that the attenuation loss of the fabricated FGC lines is as low as 3.2 dB/cm at 40 GHz.

In the second project, a novel approach for fabricating low cost capacitive RF MEMS switches using directly photo-definable high dielectric constant metal oxides has been developed. In this approach, a radiation sensitive metal-organic precursor is deposited via spin coating and converted to a high dielectric constant metal oxide via ultraviolet exposure. The feasibility of this approach is demonstrated by fabricating bridge-type and cantilever-type switches with a photo-definable mixed oxide dielectric film. These switches exhibited

significantly higher isolation and load capacitances as compared to comparable switches fabricated using a simple silicon nitride dielectric. Electrical characterization of the mixed metal oxide and the measurement results of the fabricated switches will be shown in Chapter III.

The third project presents an RF MEMS switch developed on a low cost, flexible liquid crystal polymer (LCP) substrate. Its very low water absorption (0.04%), low dielectric loss and multi-layer circuit capability make it very appealing for RF Systems-On-a-Package (SOP). In chapter IV, a capacitive RF MEMS capacitive switch on an LCP substrate and its characterization and properties up to 40 GHz is presented for the first time.

The fourth project is to develop a tunable RF MEMS switch on a sapphire substrate with BST as dielectric material, which is deposited by a Combustion Chemical Vapor Deposition (CCVD) technology. BST has a very high dielectric constant (>300) making it very appealing for RF MEMS capacitive switches. The tunable dielectric constant of BST provides a possibility of making linearly tunable MEMS capacitor-switches. Here we present for the first time a capacitive tunable RF MEMS switch with a BST dielectric and its characterization and properties up to 40 GHz, and the details will be shown in Chapter V.

Chapter VI shows the basic research for reliability issues of RF MEMS switches like dielectric charging effect on capacitive MEMS switches. In chapter VII, integration of two reconfigurable RF circuits with RF MEMS switches are discussed, the first one is a reconfigurable dual frequency (14GHz and 35 GHz) antenna with double polarization using RF MEMS switches on a multi-layer LCP substrate; and the second one is a tunable Ka band bandpass filter with tunable BST capacitors and RF MEMS switches on sapphire substrate.

CHAPTER I

INTRODUCTION

The development of the wireless communication has led to the huge growth of emerging consumer and military applications of radio frequency (RF), microwave and millimeter wave circuits and systems. Applications include wireless personal (hand-held) communication systems such as mobile phones, wireless local area networks (WLANs), satellite communications and automotive radar. Future hand-held and ground communications systems, as well as communications satellites will require very low weight, volume and power consumption in addition to higher data rates and increased functionality. Improvements in the size and component count have been achieved by increasing the level of integration. Despite many years of research, there is a technological barrier for the IC industry to further increase the integration. Components, such as high-Q inductors, capacitors, varactors and ceramic filters, play a limiting role in further reducing the size. Passive components are indispensable in RF systems and are used for matching networks, LC tank circuits (in VCOs), attenuators, power dividers, filtering, switching, decoupling purposes and as reference resonators. On-chip passive components, fabricated along with the active elements do not result in components with the required high-quality factors offered by the off-chip passives. There is also an urgent need to reduce more and more the supply voltage and the dc power consumption to extend the battery lifetime (and this in particular for hand-held commercial communication systems), while maintaining (or even improving) RF performance. The reduction of dc power has degrading effect on certain RF performance characteristics, and this can be compensated for by utilizing inductors (and other passives) with an even higher Q-factor (easily >40). This poses an very hard task for semiconductor technologists to achieve on-chip [111].

Right now, large percentage of the board area is taken up by the off-chip passives. For instance, 90-95% of components in a cell phone are passive components, taking up 80% of

the total transceiver board area, and accounting for 70% of the cost [11]. To reduce the space taken up by the passives, very small discrete passive components and the integration of the passive components are needed. Multi-chip module, system on a chip (SOC)/system on package (SOP) in which the passives and interconnects are incorporated into the carrier substrate offer an attractive solution to further increase the integration. System on a chip is a fully integrated design with RF passives and digital and/or optical functions on wafer. The possibility of low cost RF and microwave circuits integrated with digital and analog circuits on the same chip is creating a strong interest in silicon as a microwave substrate. Their operation on CMOS grade silicon, however, is degraded by the high loss of transmission lines and antennas. Transmission lines and passive circuit components fabricated directly on standard, low-resistivity silicon wafers, commonly used in commercial foundries, have high loss, or low Q-factors .

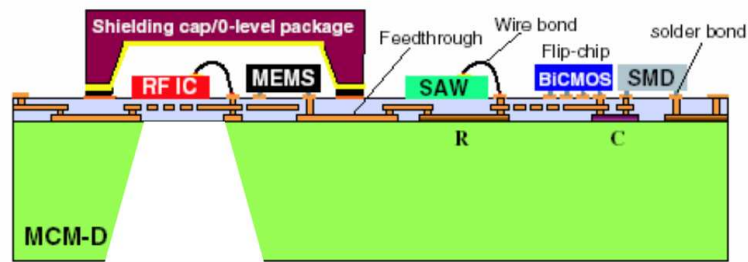


Figure 1: Developmental concept of a RF-MEMS-SOC/SOP based on the hybrid integration of the MEMS.

Micromachining techniques and MEMS (micro-electro-mechanical system or structure) technology [59,60] offer a very attractive solution that enables the integration of several passive components. Figure 1 shows the concept of a SOC/SOP based on the hybrid integration of the MEMS and other components utilizing micromachining techniques. It consists of assembling a few ICs (RFIC, mixed-signal IC, GaAs MMIC) on a single carrier substrate in a MCM fashion (as part of the 1-level packaging). Passive components can be assembled as discrete components (SAW, PIN diode, varactor diode, SMD capacitor) or embedded (Rs, Ls, Cs, LC filters, couplers, etc) within the interconnection substrate. Cost effectiveness asks for as many passives to be embedded into the substrate as possible.

MEMS is clearly an enabling technology to yield integrated wireless systems, but today we are just embarking on this new technology. The development of RF-MEMS components is underway, but integrated MEMS systems are still pretty much in an infant stage. RF-MEMS-SOC/SOP is a possible path for the future evolution of integrating RF-MEMS components together with the other passives and actives as shown in Figure 1 . In this dissertation, to reduce the transmission line loss, and increase the integration of RF circuits on CMOS grade silicon substrate, research on the integration of finite ground lines on complementary metal oxide semiconductor (CMOS) grade silicon has been performed using bulk micromachining technique.

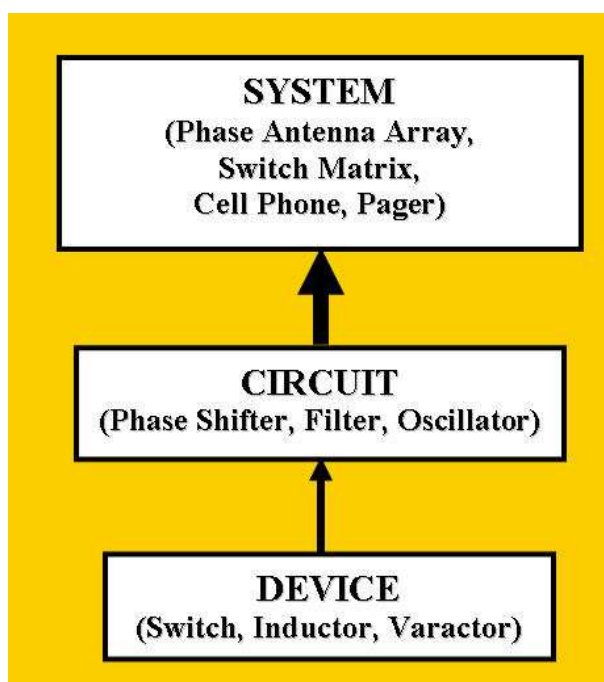


Figure 2: Typical RF MEMS "food chain".

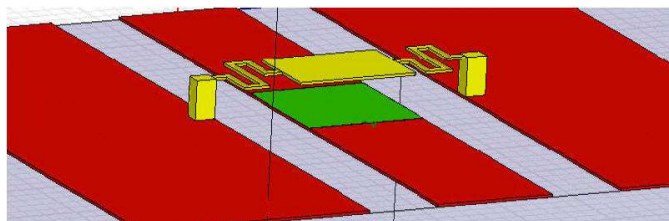


Figure 3: Structure of a typical RF MEMS capacitive shunt switch.

When applying MEMS structures to high-frequency circuits (radio frequency (RF), microwave or millimeter wave), the technology is commonly referred to as RF-MEMS [92]. The interest in MEMS technology for RF and wireless applications stems from the view that, because of its flexibility, it can be exploited to overcome the limitations exhibited by other integrated RF devices and as a result, it enables circuits with new levels of performance not achievable otherwise. Thus, the ultimate goal in applying RF MEMS is to propagate the device level benefits all the way up to the system level to attain unprecedented levels of system performance, as shown in Figure 2. RF MEMS switches are one of the most fundamental structures of the MEMS technology. RF MEMS switch technology has been introduced during the last 10-15 years as a viable alternative with superior RF performance over traditional semiconductor switches. Low-cost MEMS switches are prime candidates to replace the conventional GaAs Field Effect Transistor (FET) and p-i-n diode switches in RF and microwave communication systems, mainly due to their low insertion loss, good isolation, linear characteristic and low power consumption. The basic structure of a typical RF MEMS capacitive switch is shown in Figure 3; it has a fixed bottom electrode, a top movable membrane and a thin dielectric layer between the two metal layers. It is designed for a very low capacitance between the top membrane and the bottom signal line in the up state. Once voltage is applied through the actuation electrode, the top membrane is deflected due to electrostatic forces and as it touches the bottom electrode, a larger metal-insulator-metal capacitor is formed. Various designs of capacitive RF micromechanical switches made out of nickel [70], aluminum [34, 105], gold [96] and copper [7] have been so far reported in literature, with a variety of applications such as phase shifters, reconfigurable filters, tuners and other planar circuits. The structure of these switches consists of a lower electrode, a very thin dielectric layer and the moveable membrane. Several studies have also shown the importance of the dielectric layer in the switch performance (C_{max}/C_{min} ratio, isolation) and reliability [31].

Figure 4 shows the cross section of a DC contact MEMS switch, it has three sections of metals: the first one is the suspension beam (or membrane), the second one is the output transmission line ("RF OUT" in Figure 4), and the last one is the bottom electrode

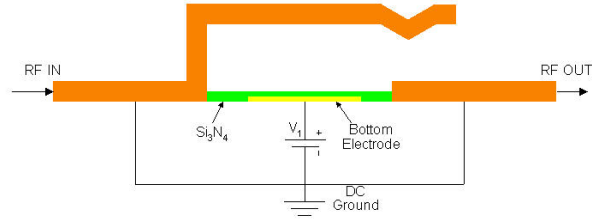


Figure 4: The cross section of cantilever DC contact RF MEMS switches [130].

underneath the thin film dielectric material Si_3N_4 . The operation of this switch is the similar as for the capacitive switch; the difference is that when a voltage is applied between the membrane and the bottom electrode, the membrane will be in DC contact with the output transmission line (“RF OUT” in Figure 4). As a result, it presents a very small resistance, around $0.5 \sim 1 \Omega$ to the RF line.

RF MEMS switches have also paved the way for the development of revolutionary RF circuits that can be potentially used in the next generation of broadband, wireless and intelligent communication and radar systems. Many researchers have been focusing recently on the development of miniaturized, low power and low cost RF/microwave circuits with RF MEMS switches [31,82,87]. For this reason, several different types of capacitive MEMS switches have been developed both at academic institutions and in industry. They can be classified as follows: airbridge [34] or cantilever beam [31,82]. The RF/microwave and the mechanical behavior of these MEMS switches have also been characterized [23,25,97,110].

Figure 5 shows two different types of capacitive switches developed at the University of Michigan. The first one, shown in Figure 5(a), is based on an inline configuration (anchors attached to the center conductor and the electrode attached to ground) [64], and the second capacitive switch is based on a low spring constant membrane (the membrane is connected using a folded spring to the anchors) [70]. The Analog Devices MEMS-series inline ohmic switch is shown in Figure 6(a) [63]. The switch is fabricated using a 7-8 μm thick gold cantilever and is suspended 1 μm above the substrate. The switch is very compact and is around 75 μm long and 30 μm wide. The pull-down electrode is defined near the end of the cantilever and is $20 \times 35 \mu m$. There are two contact points, each with dimensions around

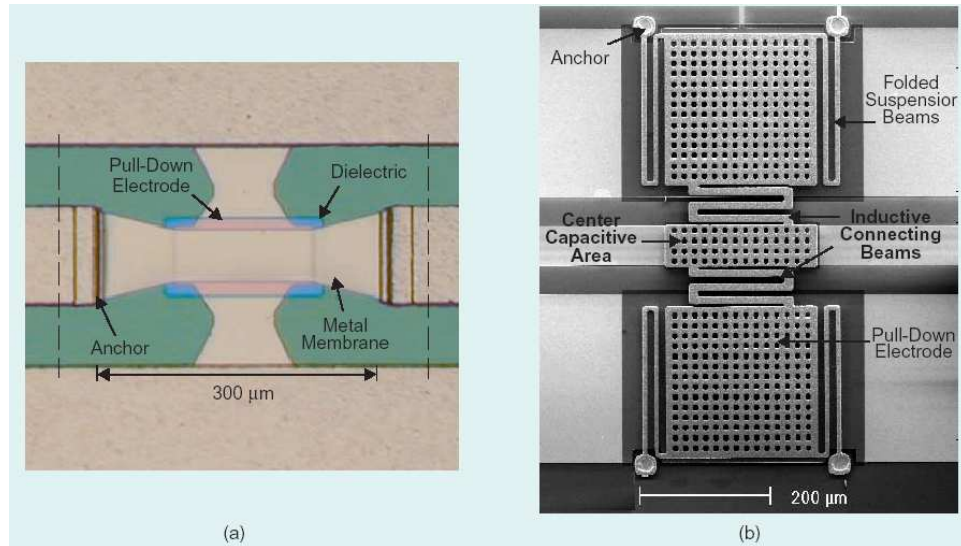


Figure 5: (a) University of Michigan low-height high-spring-constant gold MEMS switch and (b) low spring-constant MEMS switch [64, 70].

2- μm square. The spring constant is 60-100 N/m, which results in a pull-down voltage of 60-80 V and a switching time of 2-3 μs . The mechanical Q is close to 1, therefore, the switch settles quickly upon actuation. The contact force is 100-150 μN , and the switch resistance is 0.5-1.0 Ω . The up-state capacitance is 4-5 fF, and the measured isolation is -40 dB at 4 GHz and -26 dB at 20 GHz. The measured insertion loss is -0.15 dB up to 20 GHz. The University of Michigan developed an all-metal broadside-series switch (Figure 6(b)) [64]. In this case, the pull-down electrodes are moved away from the center of the switch, and the switch is anchored on both sides of the transmission line. The switch is fabricated using a 0.8 μm thick gold layer and is suspended 1.7 μm above the transmission line. The spring constant is given by the anchor design and the residual stress in the membrane and is 25-40 N/m for the switch of Figure 6(b). The resulting pull-down voltage is 35-50 V. As usual, 5 μm -square gold contact points are used, and the contact resistance is 1-2 Ω . The up-state capacitance is 6-8 fF, which results in an isolation of -35 dB at 4 GHz. The University of Michigan switch is completely compatible with the shunt-capacitive switch fabrication technique, therefore, it can be used in series/shunt designs.

Due to their superior RF performance (low loss, low power and low intermodulation

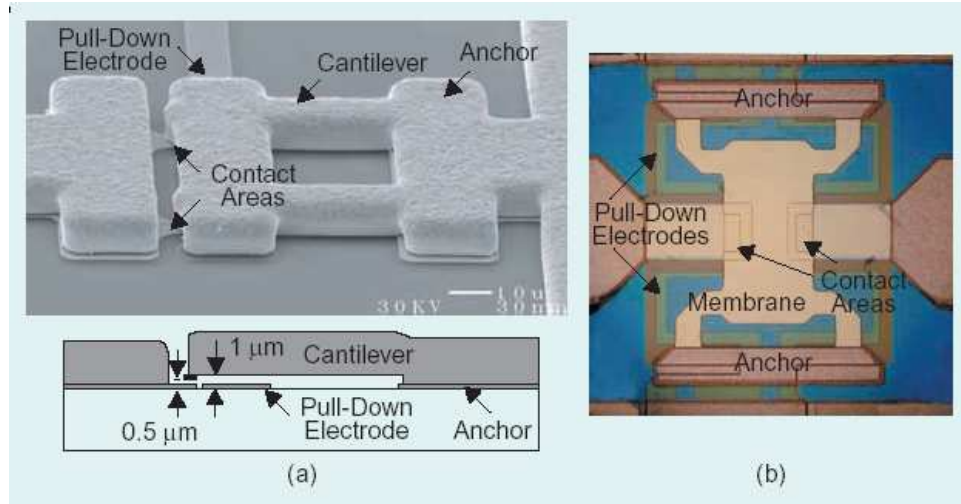


Figure 6: a) Analog Devices MEMS-series switch (Courtesy Analog Devices) [63] and (b) the University of Michigan MEMS series switch [64].

distortion), RF MEMS switches have been used in variety of RF circuit applications: tunable microwave filters [2, 8, 11, 33, 106], tunable phase shifters [4], tunable antennas [17] and tunable matching networks [73]. In most MEMS capacitive switches reported so far, the dielectric layer is typically silicon nitride or silicon dioxide deposited with Plasma Enhanced Chemical Vapor Deposition (PECVD) or High Density Inductively Coupled Plasma (HDICP) CVD techniques [15]. A switch that uses Barium Strontium Titanate (BST) as the dielectric layer has also been reported [55]. Taking into account the higher cost associated with using CVD and sputtering techniques for the fabrication of the dielectrics layer, there is a need for lower fabrication cost switches based on cheaper dielectric layer fabrication techniques, while maintaining flexibility in the choice of the dielectric parameters (dielectric constant and loss). This dissertation presents a capacitive RF MEMS switch made with a very low cost mixed oxide dielectric layer, whose parameters can be easily controlled during fabrication to achieve the desired values. In the fabrication process, a photosensitive metal-organic precursor solution is cast onto the substrate (typically by spin coating) to form a thin, solid, amorphous precursor film. Upon Ultra-Violet (UV) exposure, the organic ligands of the precursor molecules are cleaved, resulting in the formation of an amorphous metal oxide. The remaining unexposed precursor material may be subsequently washed away by rinsing with a developer solvent [5]. The photosensitivity of these materials allows

one to selectively deposit metal oxide structures at low temperatures (1) without requiring the deposition of blanket oxides via sputtering, CVD, or other means and (2) without requiring subsequent separate lithographic and etching (typically dry etching with Reactive Ion Etching (RIE)) steps that are needed to pattern blanket films.

Most RF MEMS switches reported so far, are fabricated on hard and fragile semiconductor substrates like silicon [34, 70, 105]. Miniaturization, portability, cost and performance have been the driving force for the evolution of packaging and system-on-package (SOP) approach in RF, microwave and millimeter wave applications. Liquid Crystal Polymer (LCP) provides the all-in-one solution for such a integration approach in terms of a high quality dielectric for high performance multi-band passive designs, excellent substrate for heterogeneous SOP integration as well as for MEMS structures. Furthermore, low loss and low power MEMS switches fabricated on LCP enable the implementation of multi-band and reconfigurable modules. This dissertation presents capacitive RF MEMS switches with silicon nitride as dielectric layer on flexible LCP substrate.

Microwave and millimeter-wave technology that offers wide tunability is essential for today's cost-driven commercial and military industries. In order to meet the above requirements, recently, micromachined tunable capacitors have been shown to have an adequate Q-factor when they are fabricated in either an aluminum [126,127] or a polysilicon [123] with surface micromachining technology. Also, a three-plate structure with a wide tuning range was reported [20]. Tunable capacitors are enabling components for millimeter-wave systems. There are two approaches to make such components as shown in Figure 7. One is a chemical approach that improves properties of the materials, and the other is a physical approach that controls the gap or area of the dielectric layer for variable capacitance. MEMS switches with precise, micrometer-level movements are ideal drives for the physical approach. A MEMS-based switching diaphragm could be used as a variable capacitor [32]. The tunability of this component was very impressive because a lossless, 2 μm airgap was used for the dielectric layer. However, the range of this variable capacitance was limited when the top membrane collapsed onto the bottom plate. There is need for new MEMS design providing capacitors with superior tunability. Emerging Barium Strontium Titanate (BST) thin film technology

has been investigated for enhancing RF MEMS capacitive switches due to its high dielectric constant ($\epsilon_r > 200$) in [55]. In this dissertation, a new capacitive RF tunable MEMS switch with an extra pull down electrode using BST as the dielectric layer is developed for the first time. It provides continuous (analog) tunability of the capacitor after the MEMS switch has been pulled down, due to voltage controlled properties of the BST dielectric material. The switch can be used to develop very compact and high-Q digital capacitor banks with enhanced analog tuning for a variety of reconfigurable networks (e.g. filters, tuners).

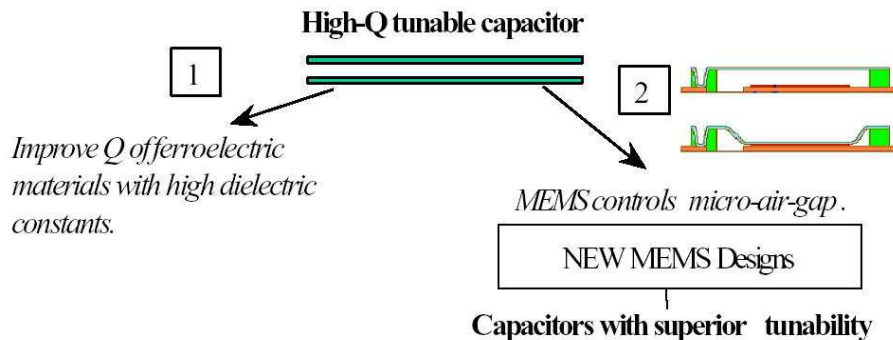


Figure 7: Approaches for the implementation of tunable capacitors.

MEMS technology enables batch fabrication of miniature mechanical transducers integrated with complementary metal oxide semiconductor (CMOS) circuits. The increasing demand for more flexible and functional, yet lightweight and low-power-consumption wireless systems, has generated the need for a technology that can dramatically reduce manufacturing cost, size, and weight, and improve performance and reliability. RF MEMS provide an opportunity to meet these requirements. Unfortunately, it has been widely observed that the performance of the switches can vary over time. Reliability of MEMS components is of major concern for long term and broad based applications, and it is currently an area of intense research [86]. For capacitive MEMS switches, the major reliability problem is stiction between the metal layer (top electrode) and the dielectric layer covering the bottom electrode in the absence of other environmental conditions. The failure is believed to be result of charge build-up in the dielectric material. This charge build-up is strictly related to the actuation voltage [30]. It is believed that these behaviors are due to charges being

injected into and trapped in the dielectric layer covering the electrode. This problem is compounded by the fact that over time and cycling, the charge in the dielectric can build up, eventually causing the switch to permanently stay closed. The lifetime of capacitive RF MEMS switches can theoretically be much higher than the lifetime of metal to metal contact switches, because no metal to metal contact degradation takes place, which limits the lifetime of, e.g., macroscopic relays. However, it was experimentally found that high- ϵ_r materials (required for the high on/off capacitance ratio needed for RF applications) are prone to charging when an actuation voltage is applied. This parasitic charge in the dielectric causes a drift in device behavior, and, ultimately, failure. What exactly causes the failure was however not very well understood, it is very meaningful to investigate the charging effect in RF MEMS capacitive switches in order to obtain a better insight on the dielectric charging mechanisms. In this dissertation, the dielectric charging effects theoretically and experimentally for capacitive RF MEMS switches with silicon nitride as dielectric layer are investigated. Dielectric charging caused by charge injection under voltage stress was observed. The amphoteric nature of traps and its effect on the switch operation were confirmed under both positive and negative control voltages. It has been confirmed that the charging is a complicated process, which can be better described through the stretched exponential relaxation. This mechanism is thermally activated with an activation energy being calculated from the temperature dependence of the capacitance transient response. The charging mechanism, which is responsible for the pull-out voltage and the device failure, is also responsible for the temperature induced shift of the capacitance minimum bias.

Future personal and ground communications systems require very low weight, small volume and very low power. In addition to decrease size, the functionality of the platforms is increased necessitating the use of highly integrated RF front ends. Furthermore, in order to transmit/receive the maximum amount of data, communications systems are moving up in frequency to X, K and Ka bands. Electronic packaging can account up to 30% of the overall system mass, thus making advanced high frequency microelectronics, high density integration and packaging a key to reducing mass while improving performance. The performance of the MEMS device depends on the package used. Therefore, the packaging

requirements of MEMS devices are very important. Micromachining techniques can also create new capabilities for packaging technologies. For example, a plastic substrate fabricated with very precise three-dimensional (3-D) structures including conductors. Several issues related to wafer-level or zerolevel packaging of RF MEMS devices are important. The main technological drivers in wireless applications are small size, low cost and modularity of the packaged components. In particular, modularity will be emphasized in the future because one key issue is how to increase integration to have system-on-package solutions that contain MEMS and integrated circuits (ICs). Packaging has always been a very important issue for IC industry, especially for fragile MEMS components. The package is an integral part of the microelectronic system. The challenge for the package is to provide all crucial functions required by the component without limiting the performance of the part. Although fabrication techniques can be carried over from IC to MEMS, the requirements of MEMS packaging are different from those of IC packaging since it is application specific and different designs are needed for different circuits. This lack of standardization leads to excessive cost for the final product [83]. Figure 8 demonstrates the MEMS package with a top covered layer. Millimeter wave systems for commercial, scientific or military applications are rapidly emerging requiring development of high frequency packaging technologies. For high-density, high frequency (5-100 GHz) packages, the performance requirements are very stringent, since poor design and fabrication can lead to increased cavity resonances and cross-talk between neighboring circuits [62]. Many materials can be utilized for packaging including plastic and alumina which offer low cost. Both, however, suffer from poor electrical performance at frequencies beyond 10 GHz. Silicon on the other hand has been extensively used and studied in the electronics industry [35]. Its electrical properties have enabled the semiconductor industry to use it as the primary dielectric material in developing ICs while the mechanical properties of silicon have been utilized to develop high performance MEMS structures. These two properties in addition to the thermal characteristics of silicon make it an appealing candidate for packaging high frequency circuits.

MEMS switches have a lot of applications and the primary advantages of MEMS devices arise from their size. Furthermore, when mass-produced, MEMS devices offer a significant

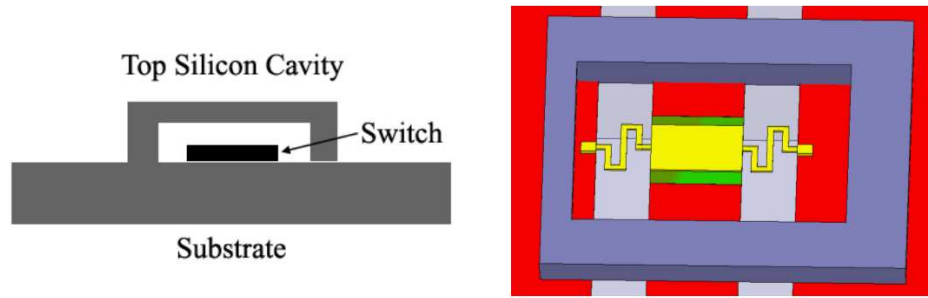


Figure 8: Demonstration of MEMS package with top covered layer

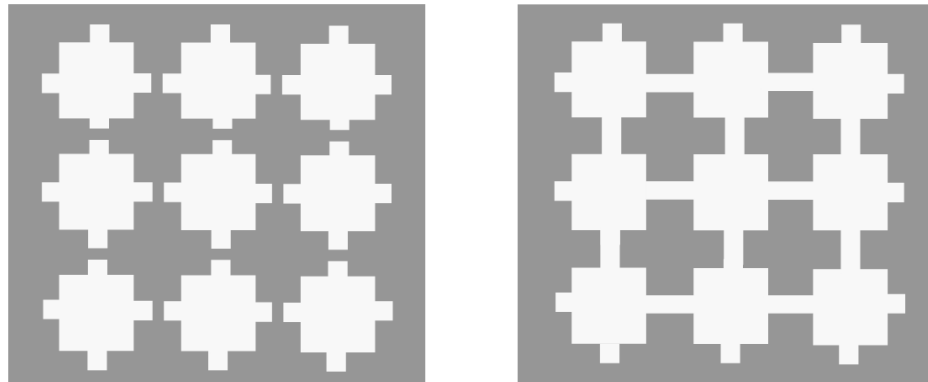


Figure 9: Configurations of a reconfigurable antenna: Open Configuration (left) and Close configuration (right).

cost advantage over conventional technologies. It has also provided the way for the development of novel revolutionary RF circuits like low cost reconfigurable and smart antenna systems-on-chip that can be used in the next generation of broadband, wireless, and intelligent communication and radar systems. RF MEMS switches have many advantages by replacing the electrical circuit elements with electromechanical signal processing. Compared with the electrical switches, the RF MEMS switches have a low insertion loss, good isolation, low power consumption and linearity. It also reduces the intermodulation distortion to minimize crosstalk effects. Single Pole Double Through (SPDT) switching circuits have been intensively used in microwave and millimeter wave communication systems for signal routing in transmit and receive applications, switched line phase shifters in phased array antennas, and wide-band tuning networks. A MEMS switched reconfigurable antenna, as shown in Figure 9, is one that can be dynamically reconfigured within a few microseconds to

choose different polarizations. Polarization diversity is gaining importance in modern wireless communication systems. In wireless local area networks, polarization diversity is used to avoid the detrimental fading loss, caused by multipath effects. In microwave tagging systems it is used as a modulation scheme such as the circular polarization modulation. In this dissertation, implementation of reconfigurable dual frequency antenna arrays for weather applications with double polarization utilizing RF MEMS switches on multilayer LCP substrate and agile Ka band bandstop filter with tunable BST capacitors and RF MEMS switches are presented.

CHAPTER II

FINITE GROUND COPLANAR LINES ON CMOS GRADE SILICON WITH A THICK EMBEDDED SILICON DIOXIDE LAYER USING MICROMACHINING TECHNIQUES

Development of Finite Ground Coplanar (FGC) waveguide transmission lines on CMOS grade silicon wafer ($\rho < 0.01$ ohm-cm) with a thick embedded silicon oxide layer using micromachining techniques is presented in this chapter. Lines with different lengths were designed, fabricated and measured. Measured attenuation and s-parameters are presented in this chapter. Results show that the attenuation loss of the fabricated FGC lines is as low as 3.2 dB/cm at 40 GHz.

2.1 Background

Radio Frequency and Microwave Monolithic Integrated Circuits (RFICs and MMICs) fabricated on silicon substrates have obtained widespread use in personal communication, GPS, and other systems that are highly dependent on cost. The possibility of integrating low cost RF and microwave circuits with digital and analog circuits on the same chip has created a strong interest in silicon as a microwave substrate. While the development of SiGe heterojunction bipolar transistors (HBTs) with a maximum frequency of oscillation, f_{max} , of 350 GHz [91,94] has enabled Si-based circuits to be used in the millimeter-wave spectrum, it is the transmission lines and passive circuit elements that have limited the wider application of Si RFICs. Conventional RF transmission lines such as microstrip and coplanar waveguides (CPWs) placed on standard CMOS grade Si wafers with a resistivity of 1-20 Ω -cm have an unacceptably high attenuation. The performance of the RF and microwave

circuits on CMOS grade silicon is degraded by the high loss of transmission lines and antennas. Transmission lines and passive circuit components fabricated directly on standard, low-resistivity silicon wafers, commonly used in commercial foundries, have high loss, or low Q-factors [75]. To overcome this problem researchers have used two different approaches. In the first approach, high resistivity silicon (HRS) wafers are used ($\rho > 2500 \text{ } \Omega\text{-cm}$) [58], [90] and traditional microwave components have a performance similar to those on dielectric substrates, such as GaAs. In the second approach, polyimide or Benzocyclobutene-based polymers (BCB) layers are used on top of the CMOS silicon substrate to create an interface layer that can host low loss microwave components. Both microstrip and coplanar waveguide transmission lines fabricated in this way have exhibited low attenuation for an optimum polyimide thickness [76], [77]. In the case of finite coplanar lines with an interface layer, the structure may be thought of as a Metal-Insulator-Semiconductor (MIS) that may support three modes of propagation (skin effect mode, a dielectric quasi-TEM mode, and a slow-wave mode). Previous work on MIS coplanar waveguides has explored this with the goal of developing slow wave structures for circuit size reduction [77], [78], [100]. However, the slow-wave structures were built on thin insulators deposited over a thin, highly doped semiconductor layer that is grown on an insulating material [100], [27]. Because the insulating layer is thin (less than $1 \text{ } \mu\text{m}$), the fields interact strongly with the semiconductor layer and the attenuation is reported to be greater than 10 dB/cm [27], [98]. Thus, while interesting and useful for some purposes, the attenuation is too high for most silicon radio frequency integrated circuits (RFICs). References [76], [77] demonstrated the viability of using thick polyimide interface layers to reduce the dielectric loss of finite ground coplanar (FGC) lines and coplanar waveguides (CPW) on low resistivity silicon wafers (Figure 10). An attenuation as low as 5 dB/cm with $20 \text{ } \mu\text{m}$ thick polyimide interface layers has been achieved. Since polyimide interface layer is being laminated or spin coated on silicon followed by a high temperature cure, there is a need for an alternative way with simple, CMOS compatible fabrication process to get comparable or even smaller attenuation of transmission lines on CMOS grade silicon. In this chapter, we present for the first time measured characteristics of FGC lines built on a CMOS grade silicon substrate ($\rho < 0.01 \text{ } \Omega\text{-cm}$) with

an embedded thick silicon dioxide layer using micromachining techniques. A schematic of the proposed structure can be seen in Figure 11. The oxide layer has a thickness of 50 microns and minimizes substantially the electromagnetic field interaction with the lossy silicon substrate. The fabrication technique is simple, low cost, CMOS compatible and does not require the deposition and post-processing of several layers as in the case of using BCB or polyimide as the interface layer.

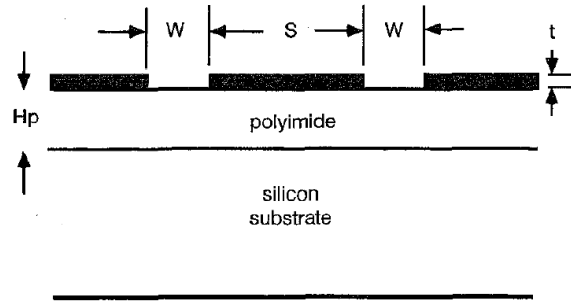


Figure 10: Coplanar waveguide on low resistivity Si with polyimide interface layer [77].

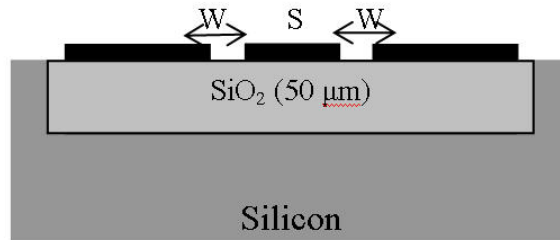


Figure 11: Cross-sectional view of the Finite Ground Coplanar (FGC) waveguide fabricated on thick oxide islands inside the silicon substrate.

2.2 Fabrication and Measurements

The resistivity of silicon substrates was first measured with a four-point probe and determined to be $0.0057 \Omega\text{-cm}$. The fabrication process flow is shown in Figure 12. The fifty microns thick silicon dioxide islands were embedded in the silicon substrate by etching deep trenches in selected areas of the silicon substrate (using the Bosch process) and subsequently oxidizing the silicon left in between the trenches [114]. This process was then augmented by a Low Pressure Chemical Vapor Deposition (LPCVD) oxide deposition in order to fill

any empty space between the oxidized slabs and create a solid piece of thick SiO₂ island. Figure 13 is an SEM picture of the cross section of such an oxide island ($\sim 50\mu\text{m}$ thick), showing the excellent quality of the oxide and very small surface roughness ($< 0.5 \mu\text{m}$).

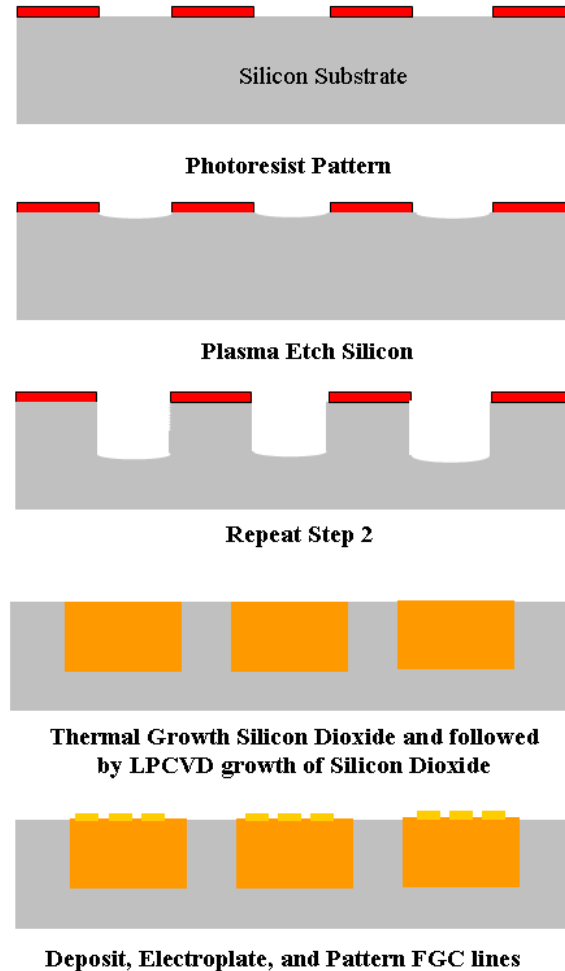


Figure 12: Fabrication process flow of the FGC lines with embedded thick silicon dioxide islands.

Once the oxide islands were created the coplanar waveguide transmission lines were patterned and gold electroplated to a thickness of $3 \mu\text{m}$ (Figures 14 and 15). Measurements were taken using an Agilent 8510 network analyzer and a Cascade probe station. The GGB Short Open Load Through (SOLT) calibration was implemented. To improve the accuracy, each circuit was measured several times. The dimensions of the different fabricated lines are summarized in Table 1. Full wave simulations were also performed using Momentum for the fabricated transmission lines and results yielded a characteristic impedance of 85Ω

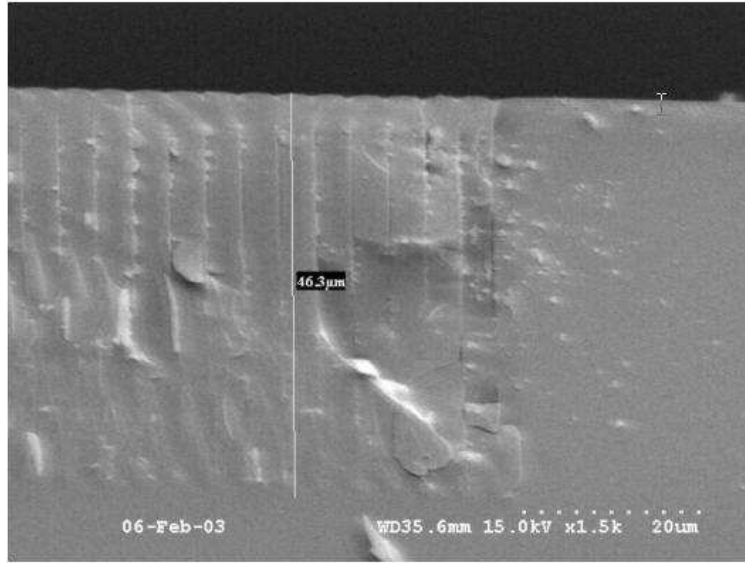


Figure 13: Cross section of 50 μm thick silicon dioxide embedded in low resistivity silicon substrate.

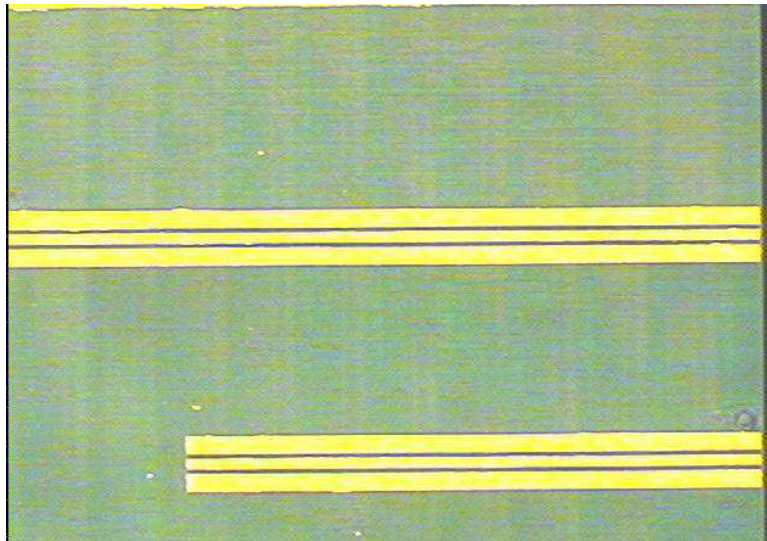


Figure 14: Photo of the fabricated FGC lines.

and an effective dielectric constant of 2.35 at 20 GHz. The latter value indicates that most of the electromagnetic field is contained within the thick oxide layer.

2.3 Results and Discussion

The measured s-parameters of the three FGC lines with different lengths fabricated on CMOS grade silicon with embedded silicon oxide layer are shown in Figure 16. It is seen

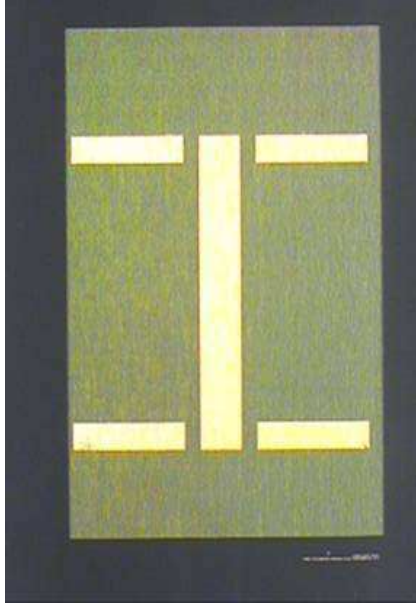


Figure 15: Photo of the fabricated transmission line.

Table 1: Dimensions of fabricated FGC lines

S (μm)	W (μm)	Length of the line(μm)
42	24	5000
42	24	4000
42	24	2500

that the maximum return loss for all lines is around 6 dB. The maximum insertion loss comes from the longest line as expected, and it is around 2.75 dB at 27.5 GHz. Figure 17 shows the s-parameter comparison between the simulation and the measurement for the 4000 μm long FGC line. The simulation results match with the measurements very well. Based on the s-parameter measurements of all three lines, the attenuation for the transmission line with $s=42 \mu\text{m}$ and $w=24 \mu\text{m}$ was extracted.

The measured attenuation for the FGC lines is shown in Figure 18. The average value of the three lines is plotted. As it is shown, the attenuation is only 3.2 dB/cm at 40 GHz and 1.5 dB/cm at 20 GHz.

Table 2 shows the measured attenuation comparison for lines fabricated on CMOS grade silicon with different interface layers. The results show that the transmission line on embedded silicon dioxide layer has less attenuation than that with polyimide interface layer

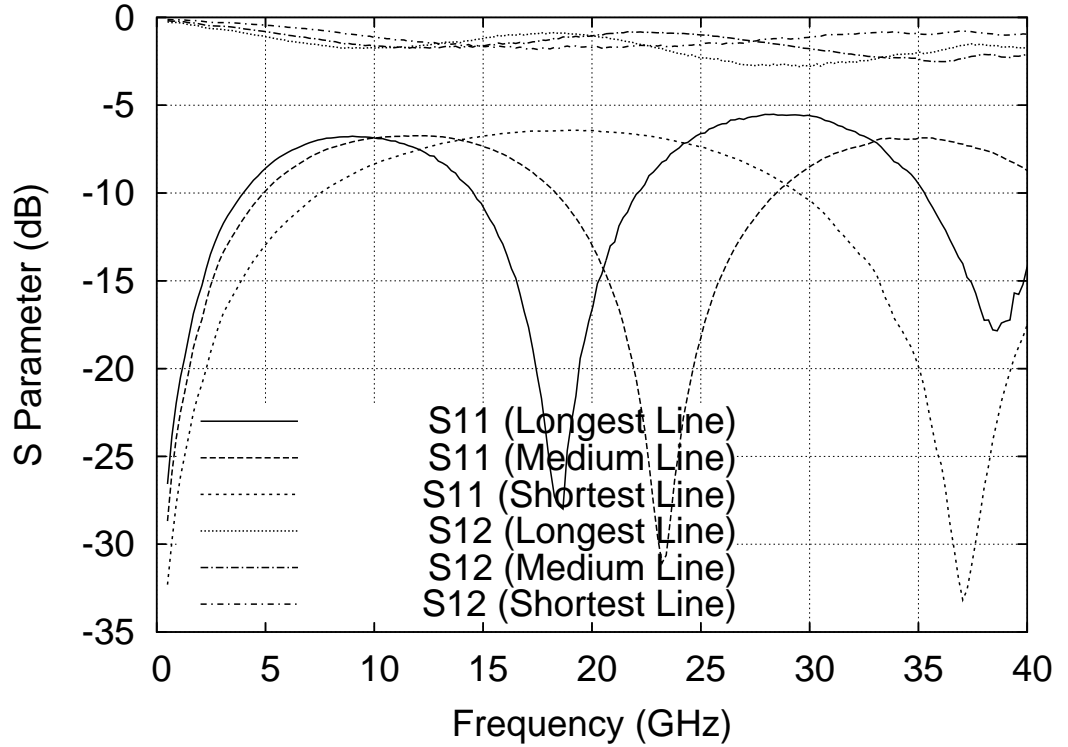


Figure 16: Measured S-parameters of FGC lines on silicon oxide islands with silicon substrates.

as thick as $20.15 \mu\text{m}$ [77].

2.4 Conclusions

FGC lines on CMOS grade silicon with embedded thick silicon dioxide layer have been developed and measured for the first time. There is a rapidly expanding market for silicon Microwave/Millimeter wave Integrated Circuits (MMICs) fabricated in standard CMOS foundries to replace GaAs MMICs in wireless communication systems, phased array radar,

Table 2: Attenuation comparison between FGC lines on embedded silicon dioxide island and FGC lines on CMOS grade silicon substrate with polyimide interface layer [77]

Substrate	Attenuation (dB/cm)
8.83 μm polyimide interface layer	7.5
14.59 μm polyimide	6
20.15 μm polyimide	5
50 μm silicon dioxide layer	3.2

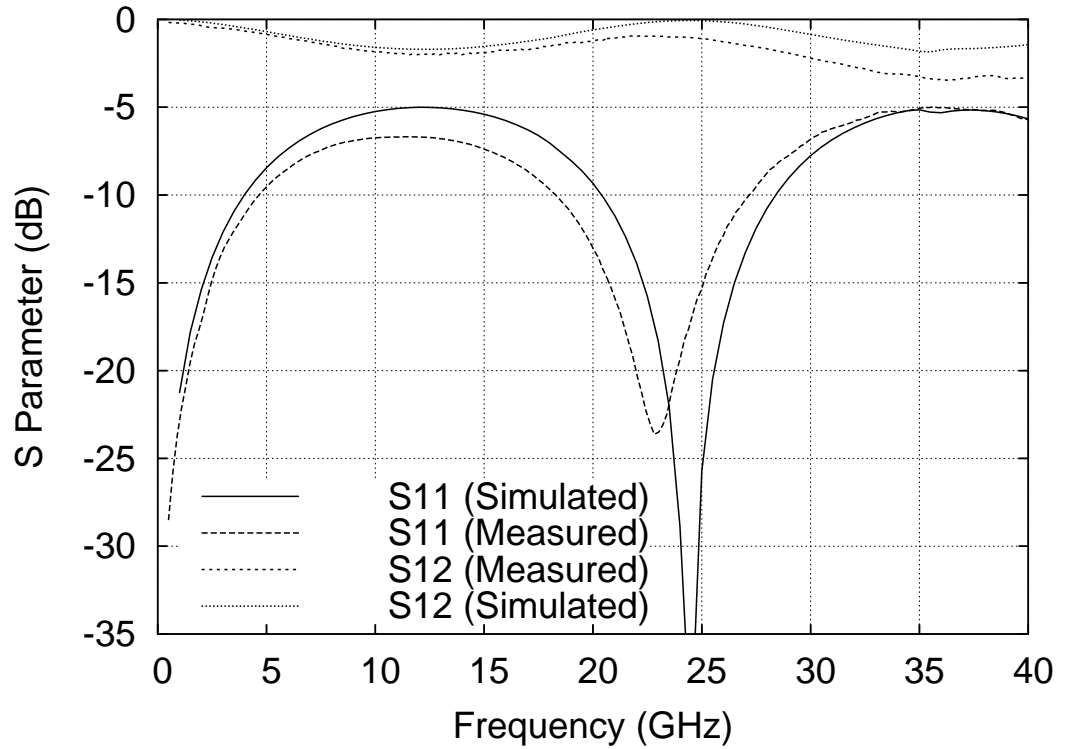


Figure 17: Comparison of the measured and simulated S-parameters of FGC line with the length of $4000 \mu\text{m}$ on silicon oxide islands with silicon substrates.

and other applications where the circuit cost is a major factor in determining the system cost. However, as mentioned previously, microwave passive elements and transmission lines placed directly on standard CMOS grade silicon have high attenuation. FGC lines fabricated on CMOS grade silicon with embedded silicon dioxide layer solves the problem of high attenuation, and it provides the possibility for integration of low cost RF and microwave circuits with digital and analog circuits on the same chip. The fabrication process is also simple and CMOS compatible and it can be used to integrate RF components like antennas as shown in Figure 19 with other semiconductor circuits.

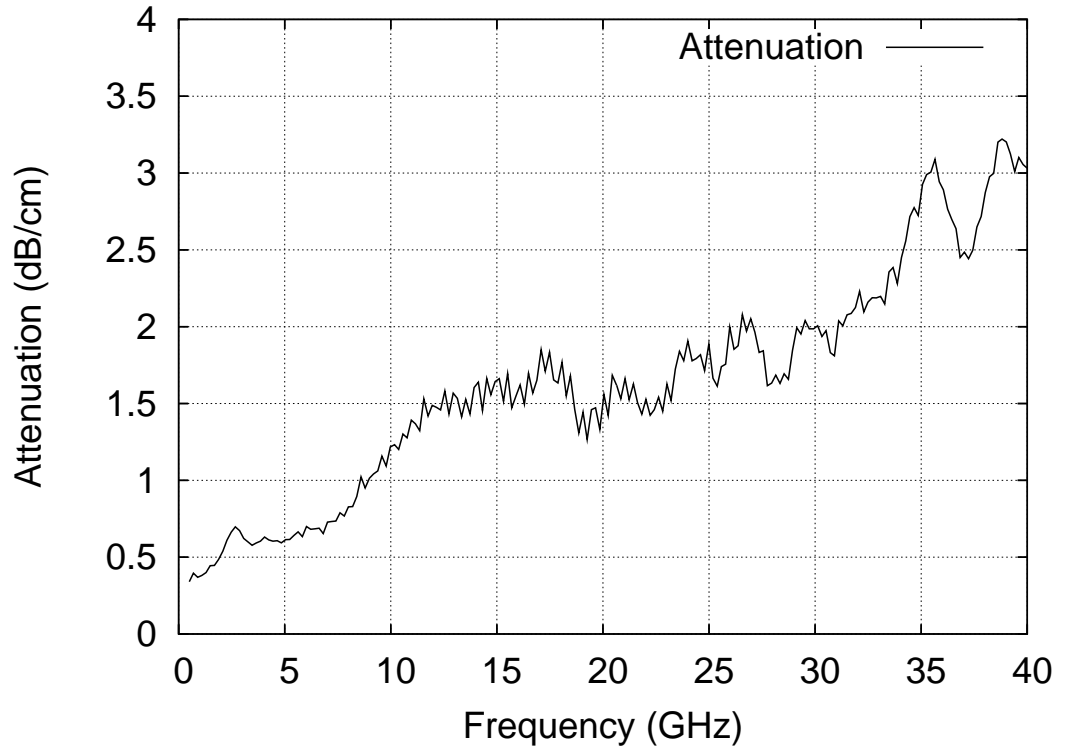


Figure 18: Measured attenuation of FGC lines on CMOS grade Si ($\rho=0.0057 \Omega\text{-cm}$) with embedded thick SiO₂ island.

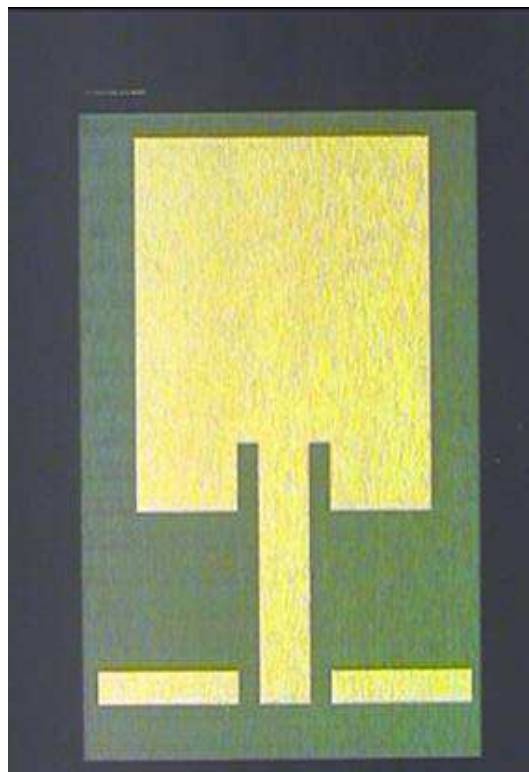


Figure 19: Fabricated patch antenna on embedded silicon dioxide.

CHAPTER III

RF MEMS SWITCHES WITH PHOTODEFINABLE MIXED METAL OXIDE DIELECTRICS

Radio-frequency microelectromechanical system (RF MEMS) is now an emerging technology with great promise for reducing cost and improving performance in certain microwave applications. In this chapter, the basic design requirements for the RF MEMS capacitive switch are discussed first. A novel approach for fabricating low cost capacitive RF MEMS switches using directly photodefinable high dielectric constant metal oxides has been developed. In this approach, a radiation sensitive metal-organic precursor is deposited via spin coating and converted patternwise to a high dielectric constant metal oxide via ultraviolet exposure. The feasibility of this approach is demonstrated by fabricating switches with the mixed oxide dielectric film. These switches exhibited higher isolation and load capacitances as compared to comparable switches fabricated using a simple silicon nitride dielectric.

3.1 Introduction to RF MEMS Switch

RF MEMS switches are devices that use mechanical movement to achieve a short circuit or an open circuit in the RF transmission line. RF MEMS switches are the specific micromechanical switches that are designed to operate at RF-to-millimeter-wave frequencies (0.1 to 100 GHz). The forces required for the mechanical movement can be obtained using electrostatic, magnetostatic, piezoelectric, or thermal designs. To date, only electrostatic-type switches have been demonstrated at 0.1-100 GHz with high reliability (100 million to 100 billion cycles) and wafer-scale manufacturing techniques [30].

The physical structure of the electrostatic-type MEMS switching device is shown in Figure 20. In this case the switch alternates between a high and a low capacitance. Here a thin metal membrane of thickness t is suspended a short distance g above a conductor. When a DC potential is applied between the two conductors, charges are induced on the

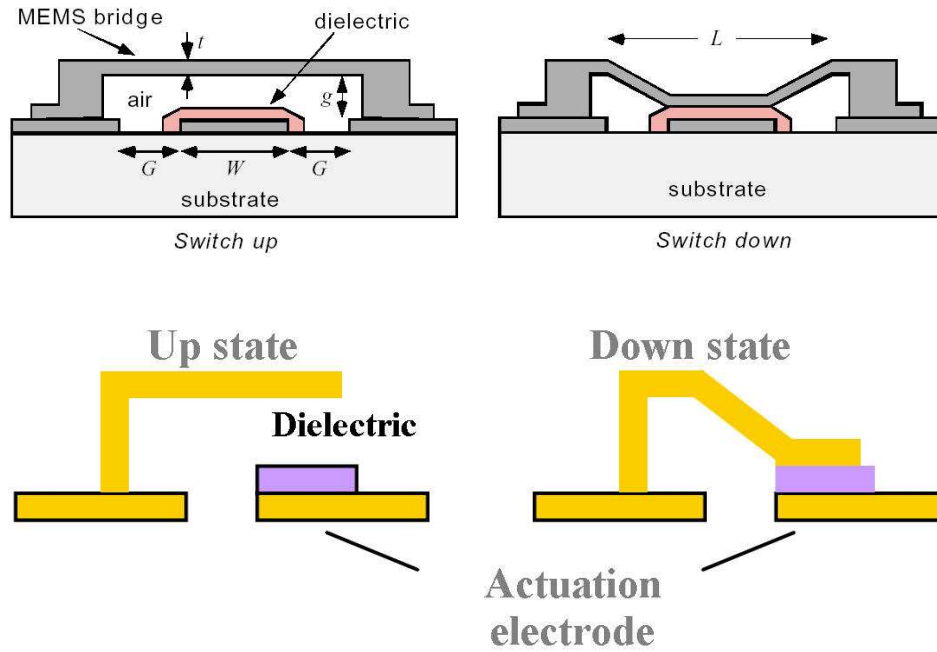


Figure 20: Physical structure and operation of electrostatic type RF MEMS airbridge switch (top) and cantilever switch (bottom).

metal which tend to attract the two electrodes. Above a certain threshold voltage, the force of attraction is sufficient to overcome mechanical stresses in the material, and the membrane snaps down to the closed position shown on the right of Figure 20. Figure 21 shows the equivalent circuit model for both airbridge and cantilever type RF MEMS capacitive switches. Both switches can be fitted with a simple parallel or series RLC electrical circuit.

The prevailing MEMS capacitive switching technology employs a thin dielectric coating over the center conductor, as shown in Figure 20, so that the device essentially switches between two capacitance states. Typically an $h=2000$ to 3000 Å thick silicon nitride (Si_3N_4) film is used with $\epsilon_r=7.5$. The capacitance in the two states can be accurately computed using parallel plate formulas, requiring only knowledge of the electrode geometries and the dielectric material. A perspective view of a MEMS switch in a coplanar waveguide configuration is shown in Figure 22 [128]. The membrane in this case is an air-bridge between the ground electrodes, which is a natural component of any coplanar waveguide circuit and therefore no unusual processing is required. The switch is designed so that the off

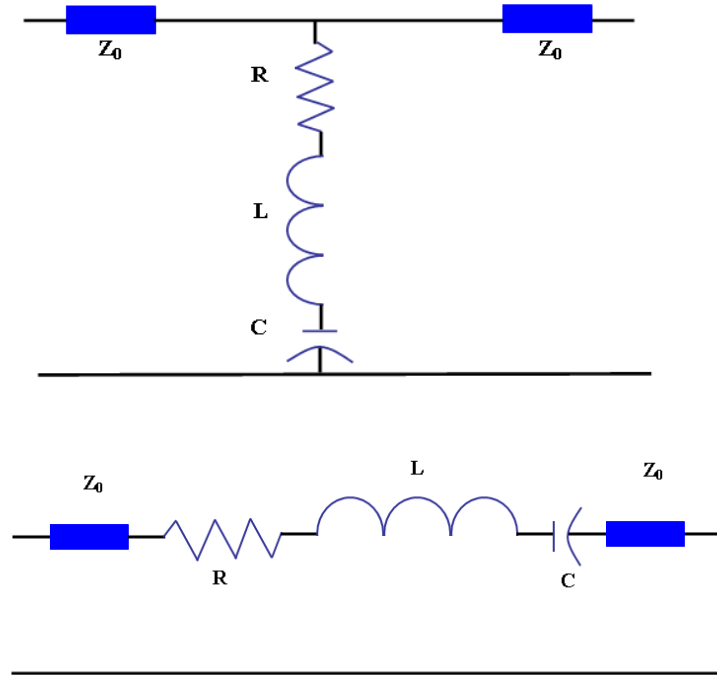


Figure 21: Equivalent circuit model for airbridge switch (top) and cantilever switch (bottom).

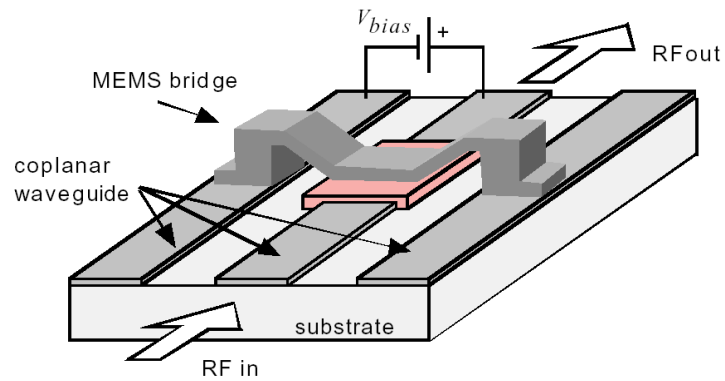


Figure 22: A coplanar waveguide implementation of RF MEMS capacitive switch [128].

capacitance is small compared to the line capacitance. When a bias above the threshold is applied between the center conductor and ground, the switch is closed, throwing a shunt capacitor across the line. The on capacitance is designed to be an effective short circuit at RF frequencies. RF MEMS switches offer a substantially higher performance than p-i-n diode or FET switches. The significant performance improvements possible with these RF

MEMS devices compared to typical FET and p-i-n diode switches has important implications in system designs for both military and commercial telecommunications at microwave and millimeter wave frequencies. The advantages of RF MEMS capacitive switches over p-i-n and FET switches are summarized below [128], [88]:

- Near-Zero Power Consumption: Electrostatic actuation requires 20-80 V but does not consume any current, leading to a very low power dissipation (10-100 nJ per switching cycle).
- Very Low Insertion Loss: RF MEMS series and shunt switches have an insertion loss of 0.1 dB up to 40 GHz.
- Very High Isolation: RF MEMS series switches have very low off-state capacitances (due to the airgap) resulting in excellent isolation up to 80 GHz.
- Intermodulation: MEMS switches are very linear devices and, therefore, result in very low intermodulation products. Their performance is around 30 dB better than p-i-n or FET switches.
- Very Low Cost: RF MEMS switches are fabricated using surface micromachining techniques and can be built on quartz, Pyrex, low-temperature cofired ceramic (LTCC), mechanical-grade high-resistivity silicon, or GaAs substrates and even a flexible polymer substrate [118].

However, there are also some problems of RF MEMS switches [128], [88]:

- Relatively Low Speed: The switching speed of most MEMS switches is around 2-40 μ s due to the mechanical movement. Certain communication and radar systems require much faster switches.
- Power Handling: Most MEMS switches can handle only 20-500 mW.
- High-Voltage Drive: Most electrostatic MEMS switches require 20-80 V for reliable operation, and this necessitates a voltage up-converter chip when used in portable telecommunication systems.

- Reliability: The reliability of mature MEMS switches is 0.1-100 billion cycles. However, many systems require switches with more cycles. Also, the long-term reliability issue like dielectric charging has not yet been addressed.
- Packaging: MEMS switches need to be packaged in inert atmospheres (nitrogen, argon, etc.) and in very low humidity, resulting in hermetic or near-hermetic seals. Packaging costs are currently high, and the packaging technique itself (high temperature bonding etc.) may adversely affect the reliability of the MEMS switch.
- Cost: Although the manufacturing cost is low, but the cost of packaging is high and the high-voltage drive chip is needed. It is, therefore, hard to beat a \$0.30-0.60 singlepole double-throw 3-V p-i-n or FET switch, tested, packaged, and delivered.

The main application areas of MEMS switches are [128], [88]:

- Radar Systems for Defense Applications (5-94 GHz): Phase shifters for satellite-based radars (20 billion cycles), missile systems (0.1-1 billion cycles), long range radars (20-200 billion cycles).
- Automotive Radars: 24, 60, and 77 GHz (1-4 billion cycles and 10 years).
- Satellite Communication Systems (12-35 GHz): Switching networks with 4×4 and 8×8 configurations and reconfigurable-Butler matrices for antenna applications (0.1 million cycles). Switched filter banks (0.1-100 million cycles, depending on the application). Also, phase shifters for multibeam satellite communication systems (1-20 billion cycles).
- Wireless Communication Systems (0.8-6 GHz): Switched filter banks for portable units (0.1-1 million cycles), switched filter banks for base stations (0.1-10 billion cycles), general SP2T to SP4T switches (0.1-10 billion cycles), transmit/ receive switches (2-4 billion cycles and 5-20 μ s switching time), and antenna diversity SP2T switches (10-100 million cycles).

- Instrumentation Systems (0.01-50 GHz): These require high-performance switches, programmable attenuators, SPNT networks, and phase shifters capable of at least 20-40 billion cycles and 10 years of operation, especially in industrial test benches.

3.2 RF MEMS Design

3.2.1 Mechanical Design of RF MEMS Switch

Figure 23 shows the operation principle of RF MEMS capacitive switches; the left one shows an airbridge RF capacitive switch on the "up" state while the right figure shows the "down" state .

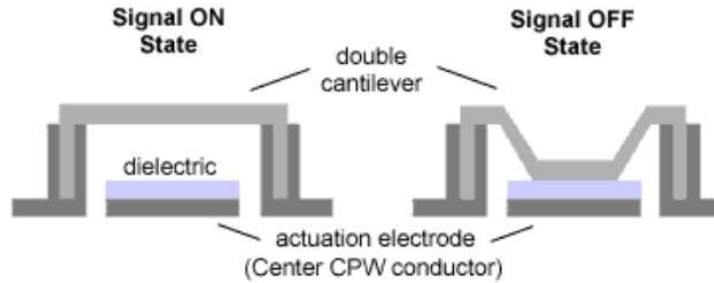


Figure 23: Operation of a RF MEMS switch.

Equations for predicting the bending of cantilever and doubly-supported beams have been around for decades [79]. Unfortunately, applying simplistic equations to complex MEMS devices can be cumbersome. The two most important mechanical features of a MEMS switch are the pull-down voltage and the deflection. Both of these quantities can be calculated by treating the MEMS switch as a mechanical spring. In order to calculate the pull-down voltage, one must equate the force pulling down on the beam by the electrostatic force between the metal layers

$$F_{down} = \frac{\epsilon_0 AV^2}{2g^2} \quad (1)$$

Where ϵ_0 is the permittivity of the air, A is the area of the actuation electrode, V is the applied voltage and the g is displacement of the top moveble metal layer.

The force pushing up from the spring using the Hooke's Law is

$$F_{up} = -k(g_0 - g) \quad (2)$$

Here g_0 is the original air gap between the two metal layers. For parallel plate electrostatic actuation, when the gap reduces to 2/3 of the original gap, the beam becomes unstable and experiences a "pull-in" effect [95]. Equating the equations above where the gap is 2/3 of the original gap and solving for the pull down voltage gives:

$$V_{pull-down} = \sqrt{\frac{8kg_0^3}{27\epsilon_0 A}} \quad (3)$$

The maximum deflection can also be calculated from the spring constant by the equation [79]:

$$\delta = -\frac{F}{k} \quad (4)$$

Where δ is the deflection, F is the force pushing down the spring and k is the spring constant. The values for the permittivity, area, and gap can be designed for and implemented in fabrication. The only two unknowns for a given MEMS switch are the spring constant and the downward force. The effective spring constant can be derived for a meandered line by the equation [86]:

$$k_m = \frac{Ew\left(\frac{t}{L_c}\right)^3}{1 + \frac{L_s}{L_c}\left(\left(\frac{L_s}{L_c}\right)^2 + 12\frac{1+\nu}{1+\left(\frac{w}{t}\right)^2}\right)} \quad (5)$$

where E is the Young's Modulus of the membrane material, ν is the poisson's ratio of the membrane, w is the width of the meander, L_s is the overall width of the spring, and L_c is the distance from the end of the spring to the start of the meander. These dimensions are illustrated in Figure 24.

For a non-meandered spring, the spring constant is given by [29]

$$k_{non-m} = \frac{32EWH^3}{L^3} \quad (6)$$

Here where E is the Young's Modulus, W is the width, H is the thickness, and L is the length of the actuation electrode.

When designing switches with low actuation voltage, the choice of the membrane material and of the support design is critical. In order to lower the pull-in voltage of the structure, three different ways can be used [70]:

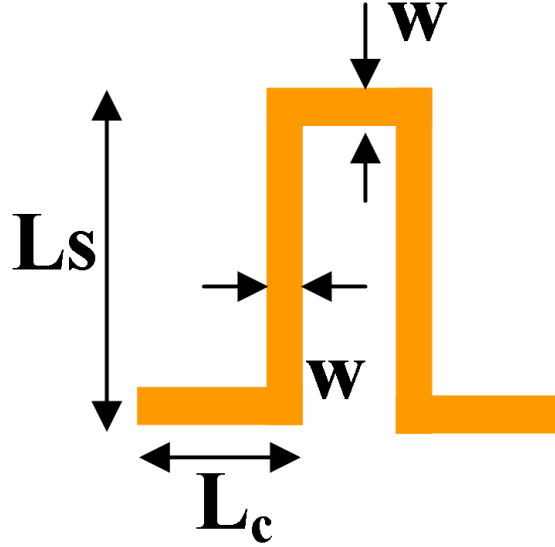


Figure 24: Illustration of dimensions.

- increasing the area of the membrane
- diminishing the gap between the switch and bottom electrode
- designing a structure with low spring constant

In the first case, the area can only be increased by so much before the device size becomes a prevailing issue. In the second case, the isolation associated with the RF signal restricts the value of the gap. The third case is the one with the most flexibility, since the design of the springs does not considerably impact the size, weight, and/or RF performance of the circuit. For a given material, the spring constant of the membrane is reduced by using meander shaped supports for air-bridge structures.

The effective spring constant, k_{eff} , for the entire MEMS switch can be determined by combining the simple spring equations in a fashion similar to capacitors. That is, springs in parallel add directly and springs in series add as the inverse of the sum of the reciprocals [48]. The spring constant of N such structures in series and parallel are respectively k_{eff}/N and Nk_{eff} . For switches that use gold for the cantilever material the expected pull-in voltages are in the range of 10-40 V.

Switches with four different support beam have been fabricated in this dissertation as

shown in Figure 25 labeled from 1 to 4.

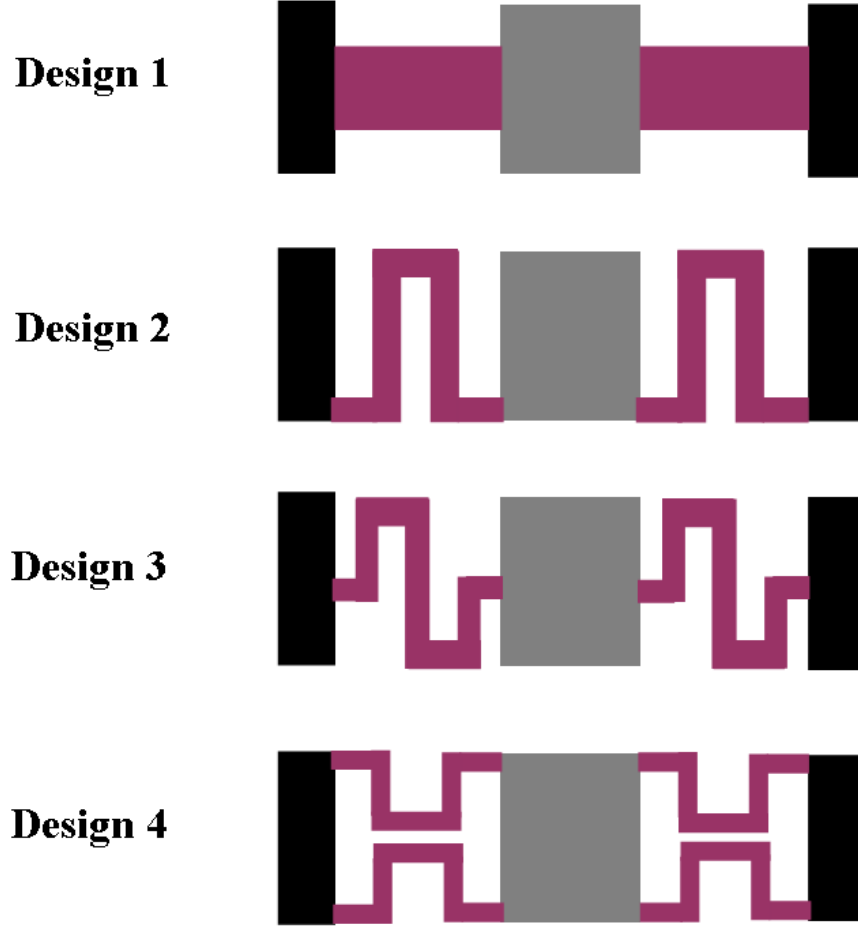


Figure 25: Switch designs with different support structure.

The effective spring constants for the four switch designs are [48]:

For Design 1:

$$k_{eff} = \frac{32EWH^3}{L} \quad (7)$$

Design 2 has two meander springs in series with a non-meander spring. The effective constant is

$$k_{eff} = \frac{k_m k_{n-m}}{k_m + 2k_{n-m}} \quad (8)$$

Design 3 has 4 meander springs in series with a non-meander spring. The effective constant is

$$k_{eff} = \frac{k_m k_{n-m}}{k_m + 4k_{n-m}} \quad (9)$$

Design 4 has two meander springs in parallel and in series with another two parallel meander springs and a non-meander spring, the effective constant is

$$k_{eff} = \frac{k_m k_{n-m}}{k_m + k_{n-m}} \quad (10)$$

Substituting k_{eff} into Equation 3 will get the theoretical pull down voltages. Another way to get pull down voltage is using FEMLAB simulation tools. Figure 26 shows the simulated deflection profile of the four switch designs.

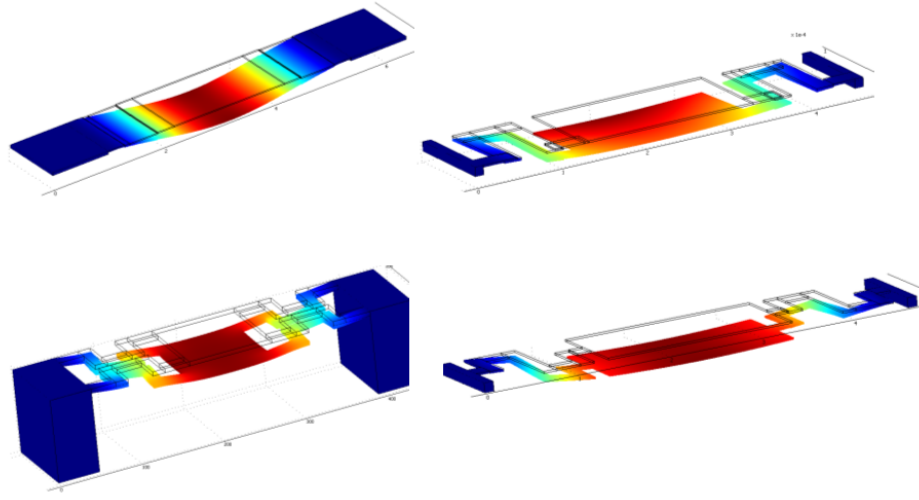


Figure 26: 3D simulated deflection profile of RF MEMS switches.

The FEMLAB 3.0 static structural mechanics module from Comsol was used for the mechanical simulations. FEMLAB is a multiphysics simulation tool. Using FEMLAB, it is easy to determine the force necessary to deflect the MEMS switch a desired distance. Ideally, it is necessary to deflect the MEMS switch the same distance as the gap between the beam and the metal layer below it. The equation that relates force to pull-down voltage in terms of the gap is given by [79]

$$V_{pull-down} = \sqrt{\frac{2g^2 F}{\epsilon_0}} \quad (11)$$

3.2.2 Electrical Design of RF MEMS Switch

As shown in Figure 21, the capacitive switch behaves like a series (cantilever switch) or parallel (shunt or airbridge type) RLC circuit, since the springs exhibit an inductance, the

actuation region exhibits a capacitance, and the metal beam exhibits a resistance. It is important to evaluate the RF characteristics and the value of R, L and C since the resonant frequency of the switch is given by Equation 12:

$$f = \frac{1}{2\pi\sqrt{LC}} \quad (12)$$

The R, L, and C value can be calculated within an order of magnitude by using fundamental equations. The resistance can be calculated using [80].

$$R = \frac{\rho L}{HW} \quad (13)$$

where ρ is the resistivity of the metal beam, L is the length of the beam, H is the thickness of the beam and W is the width of the beam. The capacitance can be calculated by:

$$C = \frac{\epsilon A}{g} \quad (14)$$

where A is the effective contact area of the electrode, g is the thickness of the dielectric layer, and ϵ is the permittivity of the dielectric material.

There are several ways to get the value of the inductance. The first way is to calculate the inductance using Equation 12. The second solution is to fit the measured data to get the parameters (R, L, and C) using Agilent ADS simulation tools with a simple RLC circuit as shown in Figure 21. In addition, a simulation tool RAPHEL can also be used to decide the value of the inductance for a given structure.

In order to design RF MEMS capacitive switches for high frequency (> 50 GHz) applications, it is very important to design the switch with a very high resonant frequency. Capacitive membrane switches generally have meandered line springs, which reduces the force required to reach pull down but limits the maximum usable frequency. To achieve higher bands of operation, the meandered region is replaced with a wide metal band (Figure 27 shows the SEM photos of the fabricated MEMS switch for frequency up to 90 GHz and Figure 28 shows the close up view of a fabricated 50-90 GHz RF MEMS switch.). Holes in the membrane can also be added to reduce the capacitance for the switch at down position. Research has been done showing that the holes has no effect on the pull down voltage [86]. These changes reduce the effective capacitance and inductance which raises the resonant

frequency, but also increases the actuation voltage due to the higher spring constant. To reduce the pull down voltage, one possible way is to increase the length of the beam.

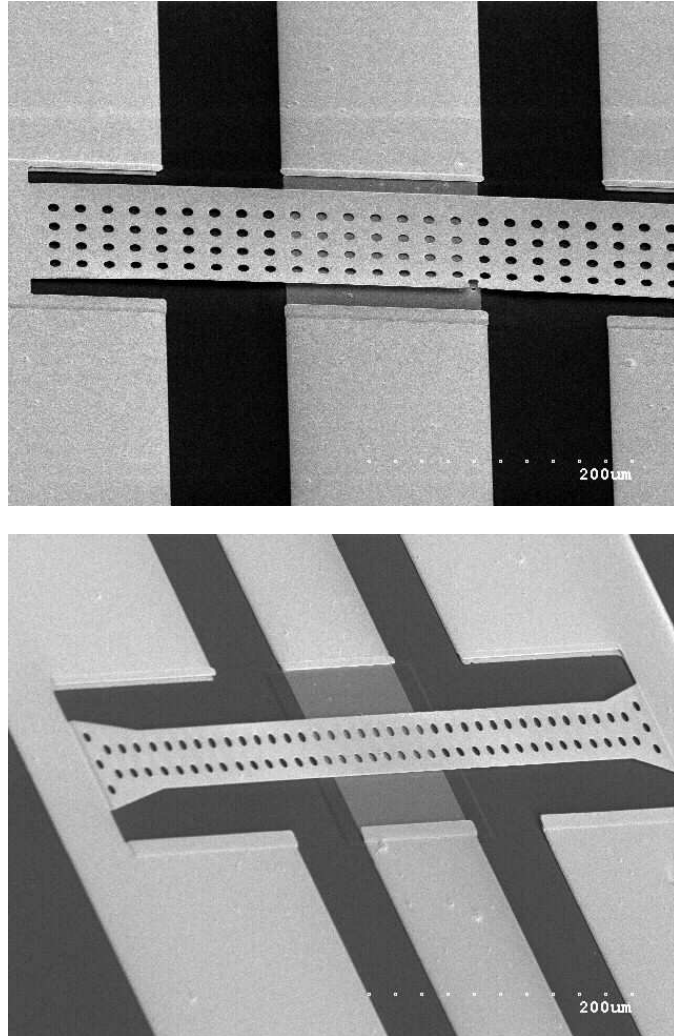


Figure 27: SEM photos of fabricated switch for 50 - 90 GHz applications.

Switches with the four different support designs were developed to determine the resonance frequency. The measured results are shown in Figure 29. In addition, the comparison between the theoretical, simulated and measured pull down voltage is summarized in Table 3 and the fitted RLC data is summarized in Table 4.

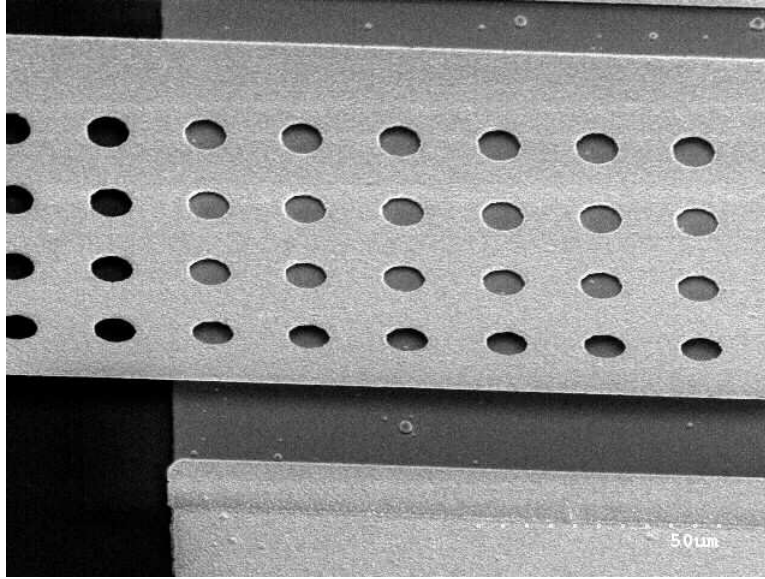


Figure 28: Close up view of a fabricated switch for 50 - 90 GHz applications.

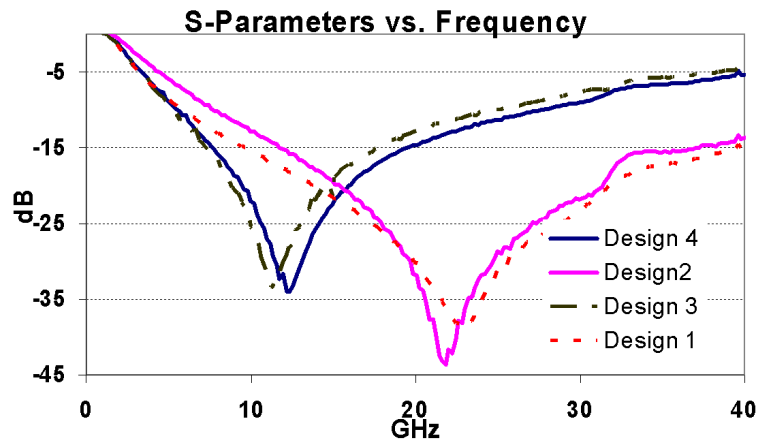


Figure 29: Measured results for the switches with a different support design.

3.3 *RF MEMS Switch with Photodefinable Mixed Oxide Dielectrics*

3.3.1 Motivation and Introduction

RF MEMS switches are prime candidates to replace the conventional GaAs FET and p-i-n diode switches in RF and microwave communication systems, mainly due to their negligible power (\sim a few nW) consumption, low insertion loss, small size and light weight. Applications for such devices include next-generation reconfigurable communication systems. RF MEMS switches are in essence mechanical switches, allowing either capacitive

Table 3: Comparison of theoretical, simulated, and measured pulldown voltage

Design	Theoretical (V)	Simulated (V)	Measured (V)
1	117	127	100
2	69	73	72
3	32	28	30
4	40	38	35

Table 4: Capacitance, Inductance and Resistance of the RF MEMS switches with different support design

Design	Resonant Frequency (GHz)	C	L	R
1	23.2	2.2pF	22pH	0.4 Ω
2	21.6	2.0pF	28pH	0.5 Ω
3	11.4	2.9pF	66pH	0.5 Ω
4	12.4	2.8pF	60pH	0.5 Ω

contact (AC) switching or ohmic contact (DC) switching. Various designs of capacitive RF micromechanical switches made out of different metals have been reported in literature. High quality dielectric material is the key factor for good RF performance in terms of isolation (C_{max}/C_{min} ratio) and reliability of RF MEMS capacitive switches. For most MEMS switches reported so far, the dielectric layer is typically silicon nitride or silicon dioxide deposited with Plasma Enhanced Chemical Vapor Deposition (PECVD) or High Density Inductive Coupled Plasma (HDICP) CVD techniques [15]. A switch that uses BST as the dielectric layer has also been reported [55]. There is a need for lower cost switches based on inexpensive dielectric layer fabrication techniques, while maintaining flexibility in the choice of the dielectric parameters (dielectric constant and loss). To reduce the high cost associated with using CVD and sputtering techniques for fabrication of RF MEMS switches, preliminary research on capacitive RF MEMS switches made with a very low fabrication cost photo-definable metal oxide dielectric has been reported previously [115]. However, the switches reported previously which used these low cost dielectric fabrication methods [115] suffered from reduced reliability due to a stiction issue that occurred when the switch was activated caused by the relatively high actuation voltage combined with the low break-down voltage of the metal oxide used. In other words, occasionally the dielectric

would break-down when the switch was actuated and the switch membrane then appeared to be welded to the dielectric surface.

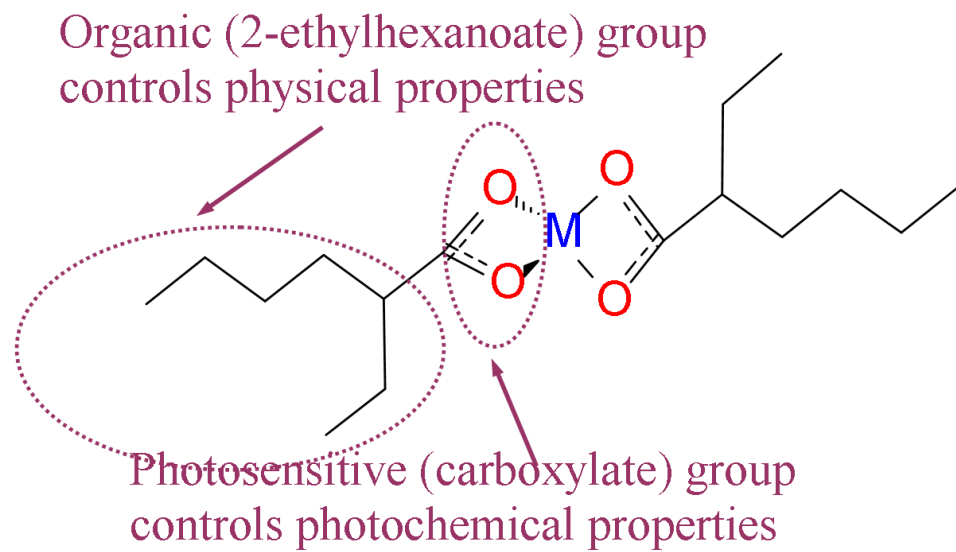


Figure 30: Molecular structure of a typical precursor.

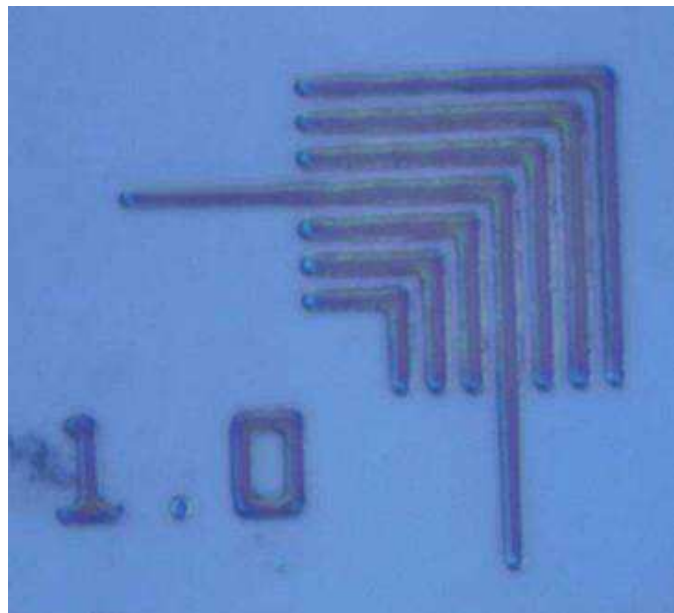


Figure 31: Photo of a 1 μm wide line of the patterned thin film.

Regardless of the processing temperature, the creation of embedded passive devices will inevitably require the ability to carry out fine patterning of the deposited thin film. Conventional dielectrics deposition techniques (e.g. CVD, PVD, sputtering, etc.) require

numerous process steps. Such methods also often require both vacuum and high temperature processing, resulting in material compatibility issues and increased cost. The plasma based subtractive etch that is often used to pattern blanket film deposited materials can be problematic due to substrate damage and difficulties associated with etching certain metals and metal oxides such as platinum and BST, respectively. Solution based approaches such as Chemical Solution Deposition (CSD), Metal Organic Deposition (MOD) and the sol-gel method allow for relatively easy compositional control and for relatively low cost deposition of blanket high-k films. However, these methods still require an etching step to create a patterned oxide, and in every case involve high temperature processing. Both of these characteristics make them ill-suited for embedded passive applications where low processing temperatures and low cost processing are required. In response to these issues, another process based on photosensitive metal-organic precursors has been investigated [6]. This process appears to be a viable low cost dielectric deposition method for embedded capacitor applications and other applications where low cost and low temperature processing are important. This research is concerned with the evaluation and processing of a new set of materials that can be deposited at room temperature using UV radiation and/or low temperature thermal treatment. This low temperature process satisfies the temperature requirements for packaging applications, and eliminates the need for costly vacuum processing. The specific class of metal-organic compounds selected for study, possess several unique properties that make them attractive candidates for this novel materials deposition process. Each of the precursor compounds as shown in Figure 30 consists of a metal atom that is linked to an organic group or "ligand" via a group that is photosensitive. The organic group is chosen in order to satisfy the desired physical properties of the precursor material. Due to the "greasy" nature of these organic ligands, strong interactions between individual molecules are absent. This characteristic prevents the formation of long-range order, and in most cases, allows these precursor films to be deposited as high-optical-quality, amorphous films suitable for use in optical patterning methods. If such a material also possesses moderate to high photosensitivity, it may fall into a unique category of materials that may be suitable for direct patterning of metals and metal oxides by lithographic

methods. The unique nature of this class of compounds makes them well suited to a variety of applications in the areas of Micro-Electro-Mechanical Systems (MEMS). This novel oxide deposition technique allows amorphous metal oxide films to be deposited at ambient temperatures and pressures. Metal-organic precursors containing carboxylate group can be used to form thin metal-organic precursor films that can be directly photo-converted to metal oxides using radiation exposure. The photosensitivity of these materials allows one to selectively deposit metal oxide structures using lithographic methods without requiring the use of the subtractive etch that is needed to pattern blanket films deposited by traditional means (i.e. PVD, CVD, sol-gel, etc.). Figure 31 shows 1 μm wide line of the direct photo patterned film. Results show that patterned lines have been fabricated using this method and a very good pattern with high contrast has been achieved.

3.3.2 Characterization of Metal Oxide Dielectrics

3.3.2.1 Fabrication of Metal Insulator Metal Capacitors (MIM) and MEMS Switches

The traditional approach of Nitride/Oxide deposition is shown in Figure 32. Photosensitive metal-organic precursors that can be coated from solution provide a unique method (as shown in Figure 33) for directly patterning high dielectric constant metal oxide structures. This directly patterned deposition method eliminates the numerous lithographic and etching steps required for patterning blanket dielectrics deposited via traditional methods such as Chemical Vapor Deposition (CVD), sputtering, sol-gel, and laser ablation processes that all deposit blanket films as discussed in the previous sections. Thus, the processing complexity and cost of depositing a patterned dielectric can be drastically reduced with this photosensitive metal-organic approach by eliminating expensive vacuum processing equipment and reducing the number of fabrication steps required to fabricate the final device. Furthermore, the dielectric constant and loss of the thin film can be controlled through chemical processes like changing the composition of mixed oxide.

In this work, precursor films consisting of titanium(n-butoxide)₂ (2-ethylhexanoate)₂ and barium 2-ethylhexanoate were spin coated from methyl isobutyl ketone (MIBK) solutions and used to directly deposit patterned mixed metal oxide dielectric pads using standard

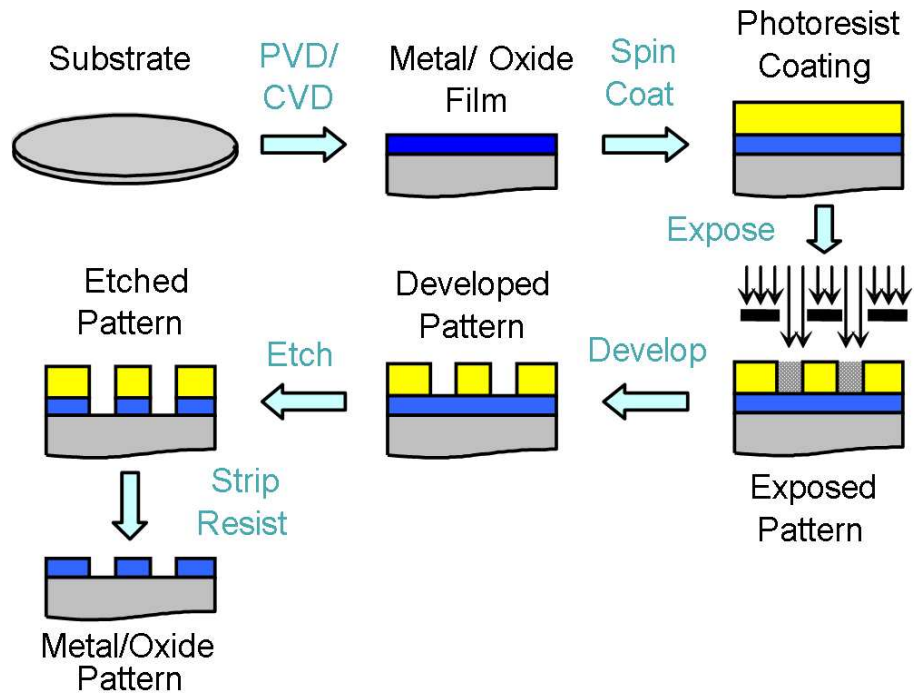


Figure 32: Traditional deposition approach of dielectric materials.

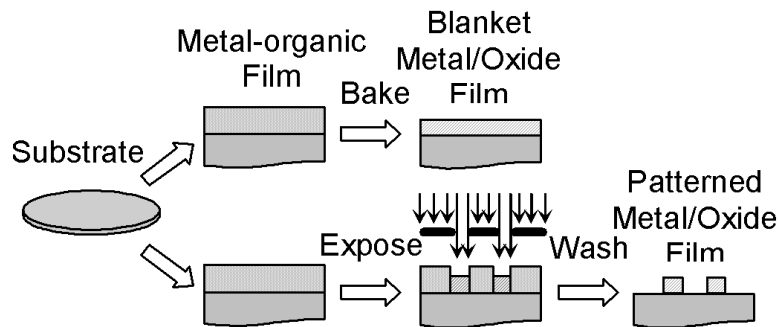


Figure 33: Schematic of process using photosensitive metal-organic compounds to produce patterned metal oxides.

lithographic exposure tools and methods. Figure 34 shows the molecular structure of the precursor. Deep ultraviolet exposure (248 nm) of these precursors results in cleavage of one of the organic ligands, producing an unstable molecule which further decomposes to form a metal oxide.

The fabrication process flow for the Coplanar Waveguide (CPW) cantilever switches is shown in Figure 35. The switches are fabricated on top of high resistivity silicon substrate

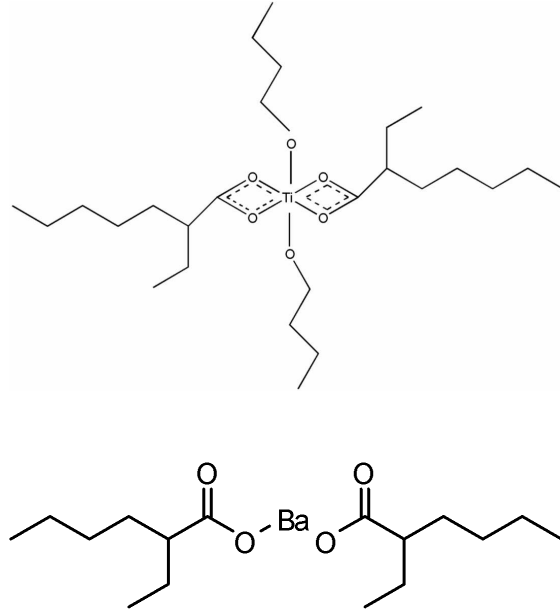


Figure 34: Molecular structures of the titanium(n-butoxide)₂(2-ethylhexanoate)₂ (top) and barium 2-ethylhexanoate used as photosensitive metal-organic compounds in this work to produce patterned mixed oxide structure.

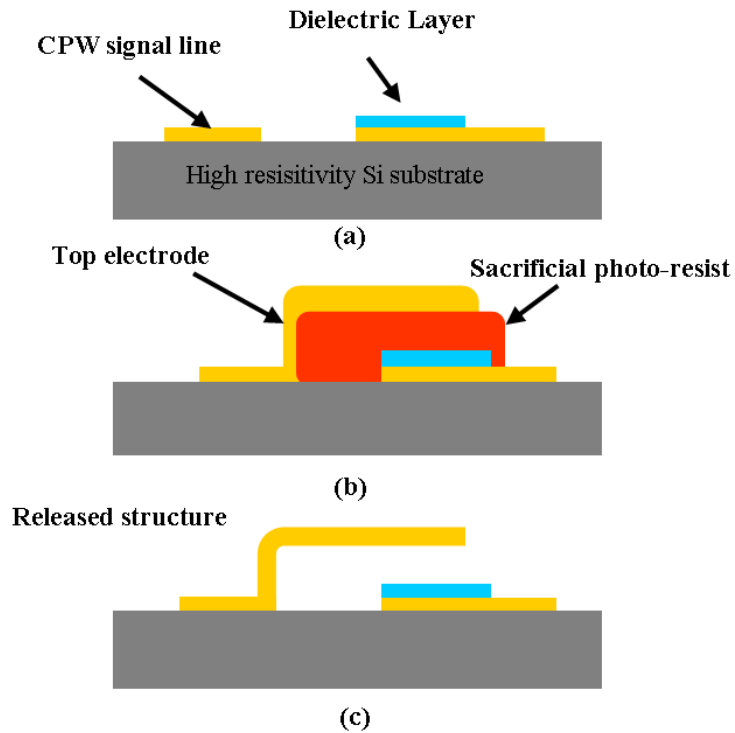


Figure 35: The cantilever switch fabrication process flow.

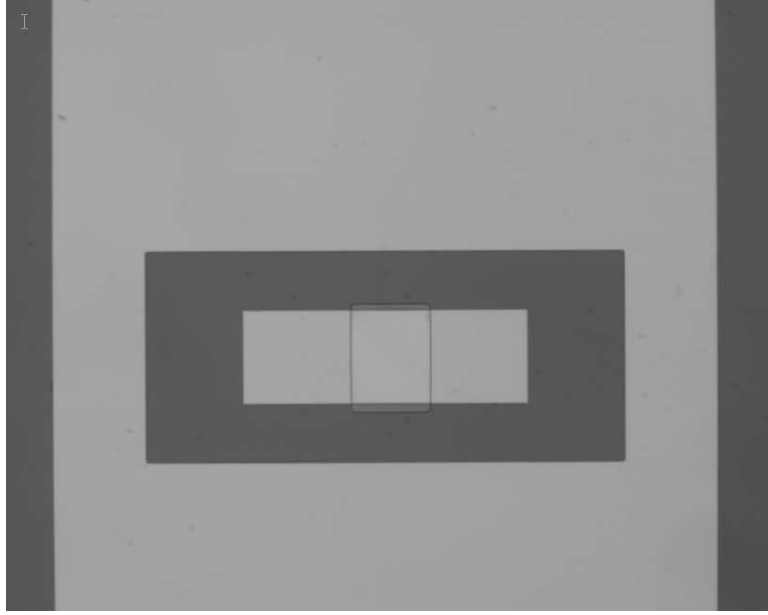


Figure 36: Photo of direct photo-patterned mixed oxide thin film.

(3000-5000 ohm-cm) with a $1\ \mu\text{m}$ thick isolation oxide layer. The CPW signal lines were fabricated by evaporating Ti/Au/Ti ($400\ \text{\AA}/5000\ \text{\AA}/400\ \text{\AA}$). A photosensitive precursor solution composed of a mixture of the metal-organic precursors for barium and titanium, was deposited by spin coating and patterned with standard DUV photolithography to form the mixed-oxide dielectric layer between the membrane and the signal line. The unexposed precursor was then washed away by rinsing with developer solvent. The dielectric was then hard baked to a thickness of $1400\ \text{\AA}$. Figure 36 shows the direct photo-patterned mixed oxide thin film on CPW bottom electrode. A $2\ \mu\text{m}$ thick photoresist (1813) was spin coated and patterned to create the airgap. A Ti/Au/Ti ($400\ \text{\AA}/3000\ \text{\AA}/300\ \text{\AA}$) seed layer was then evaporated, patterned and electroplated. Finally, after removing the sacrificial photoresist layer with a resist stripper, a critical point drying process was used to release the switches.

SEM pictures of the fabricated switches with various support design and membrane thicknesses are shown in Figures 37-38 . Figure 37 shows an airbridge type CPW switch with different meander-shaped supports and a membrane size of $120 \times 200\ \mu\text{m}$. Figure 38 shows a solid cantilever switch structure with a $1.2\ \mu\text{m}$ thick gold membrane, a $1.8\ \mu\text{m}$ air-gap and a membrane size of $90 \times 100\ \mu\text{m}$.

In order to test the electrical performance of the dielectric thin films, Parallel Plate

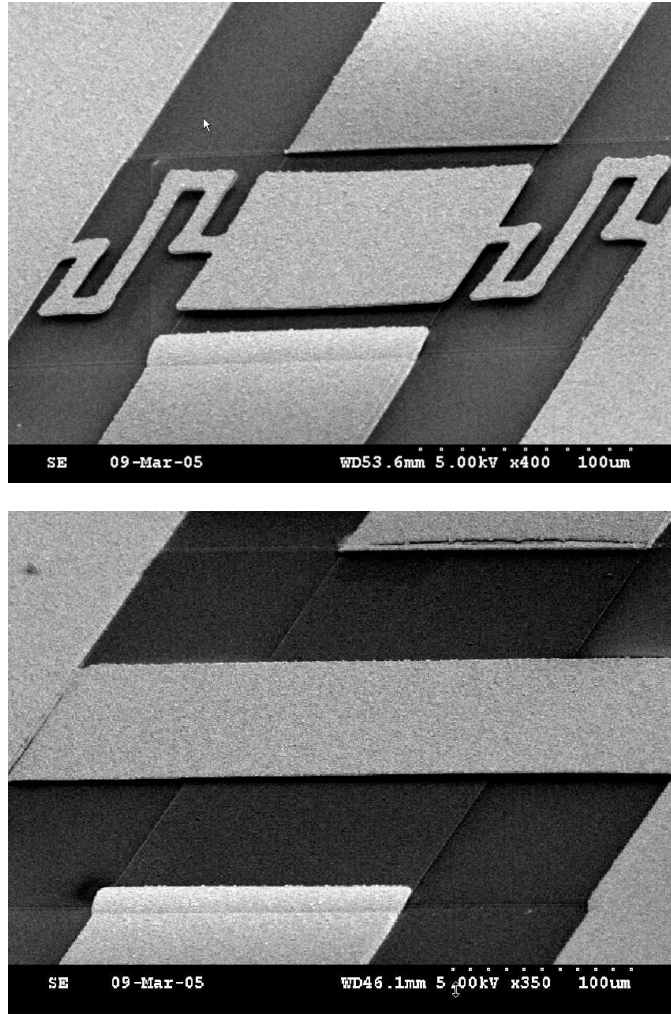


Figure 37: SEM photos of fabricated airbridge type switch with different support spring.

Capacitors (PPC) with different dimensions have been fabricated. Figure 39 shows the fabrication process flow of the PPC. Figure 40 shows the SEM photo of the fabricated parallel plate capacitors.

3.3.2.2 Characterization of the Photo-Definable Metal Oxide Dielectrics Film

Table 5 shows the dimensions for the fabricated parallel plate capacitors. I-V measurements were done using the HP 4156A semiconductor parameter analyzer. C-V measurements of the parallel plate capacitors were done using the Keithley 590 CV station at 100 KHz. Figure 41 shows the measured electrical performance of the parallel plate capacitors with the titanium dioxide as the dielectric layer. The dielectric layer has a thickness of 180 nm

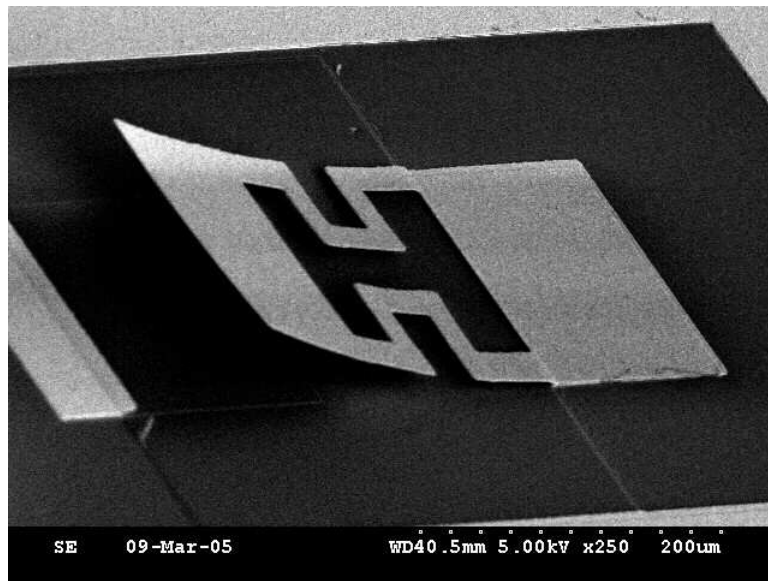


Figure 38: SEM photo of a fabricated cantilever switch.

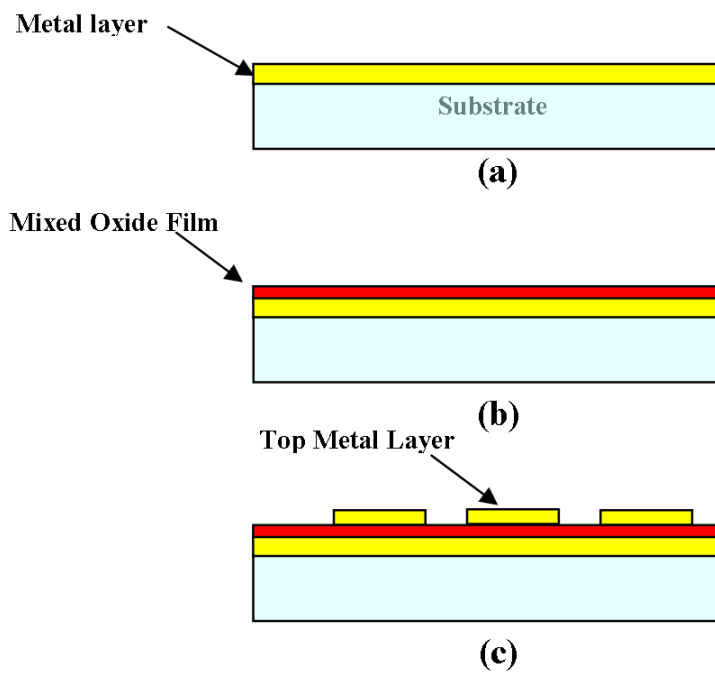


Figure 39: Fabrication process flow for the parallel plate capacitors.

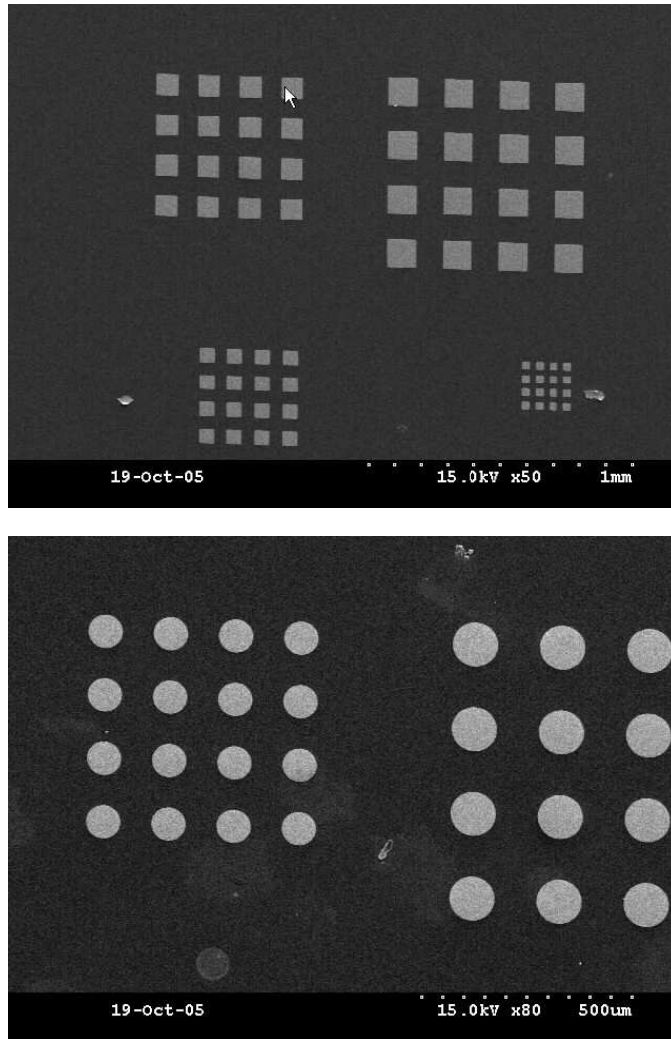
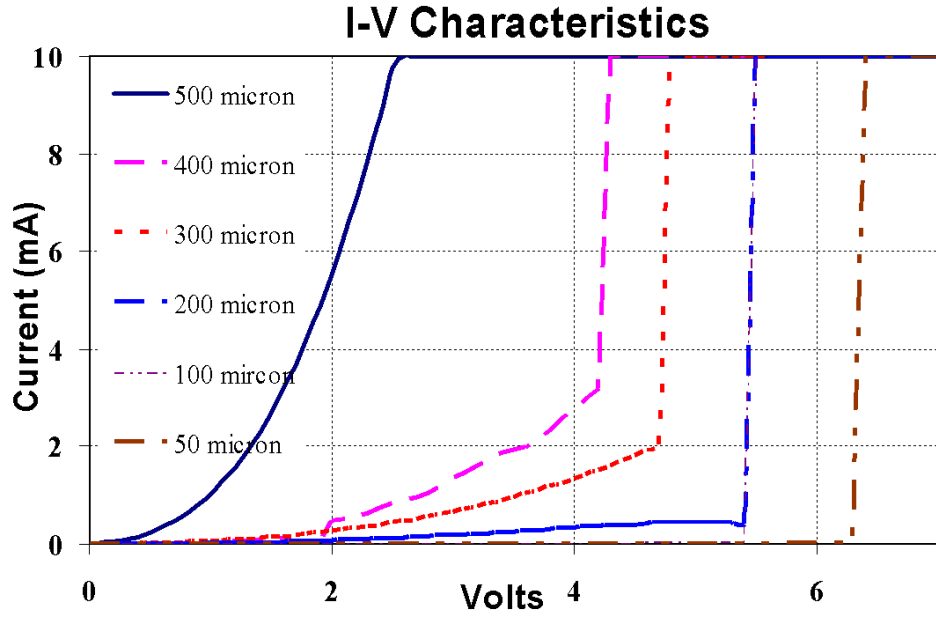


Figure 40: SEM photos of fabricated parallel plate capacitors with rectangular shape (top) and circular shape(bottom) made using the mixed oxide dielectric produced from a photosensitive metal-organic precursor solution.

and was formed with flood DUV exposure. Results show that the breakdown voltage for the dielectric thin film is only 6 volts. This is much smaller than the actuation voltage of the MEMS switch (around 20 to 25 volts). To increase the breakdown voltage of the dielectrics, A variety of different routes have been investigated for improving the breakdown voltage of the metal oxide dielectric thin films used in this work as compared to the titanium dioxide thin films reported previously [115]. Table 6 shows the comparison among different samples with different thermal hydrated treatment; in the Table "P" means only UV exposure for the formation of the dielectric thin film, and "T" means UV exposure and 200 degree C

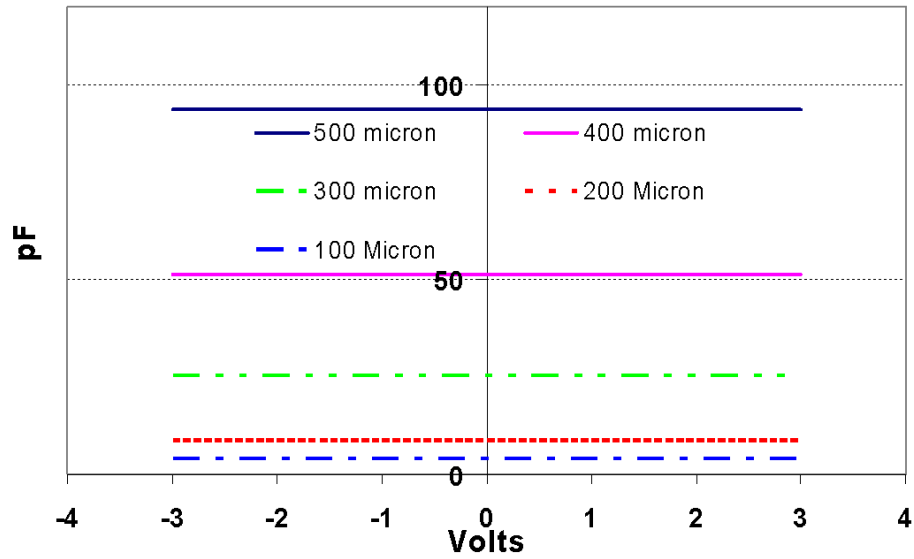
Table 5: Dimensions of fabricated parallel plate capacitors

Dimension	Circular Shape	Rectangular Shape
Diameter or Side Length(μm)	500	500
Diameter or Side Length(μm)	400	400
Diameter or Side Length(μm)	200	200
Diameter or Side Length(μm)	100	100
Diameter or Side Length(μm)	50	50

**Figure 41:** I-V measurement results of parallel plate capacitors made with the mixed metal oxide dielectric which has been processed without an oxygen plasma treatment after exposure and development of the oxide pattern.**Table 6:** Measured capacitance for different capacitors with mixed oxide dielectrics

Sample	Precursor Material	Humidity	Area (cm^2)	Thickness (\AA)	C (nF)	ϵ_r
1P	Acetylacetenate	80%	0.0314	766.4	2.4	13.4
1T	Acetylacetenate	80%	0.0314	602.6	2.7	11.7
2P	Ethylhexanoate	80%	0.0314	831.5	2.4	14.5
2T	Ethylhexanoate	80%	0.0314	643.5	2.6	12.2
3P	Acetylacetenate	15%	0.0314	805.6	1.9	10.8
3T	Acetylacetenate	15%	0.0314	716.1	2.1	10.7
4P	Ethylhexanoate	15%	0.0314	826.7	2.3	13.8
4T	Ethylhexanoate	15%	0.0314	665.5	2.6	12.4

Capacitors with Mixed Oxide Dielectrics CV Characteristics



Capacitors with Mixed Oxide Dielectrics C-V Characteristics

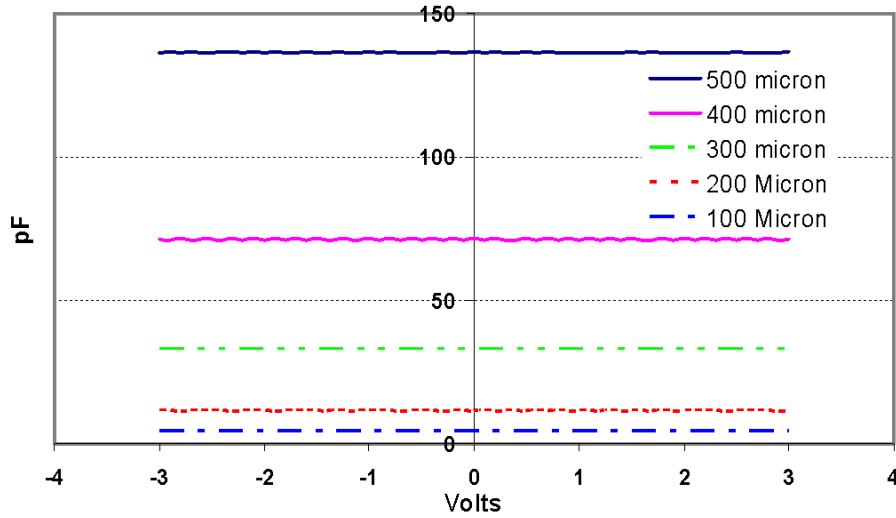


Figure 42: CV measured results for parallel plate capacitors with circular shape (top) and rectangular shape(bottom).

thermal bake. All the measurement were done at 1 MHz. Figure 42 shows the measured CV results for the parallel plate capacitors with different dimensions and shapes.

Figure 43 shows the measured I-V characteristics of the samples described in Table 6. The results show no big improvement of the breakdown voltage. One of the more

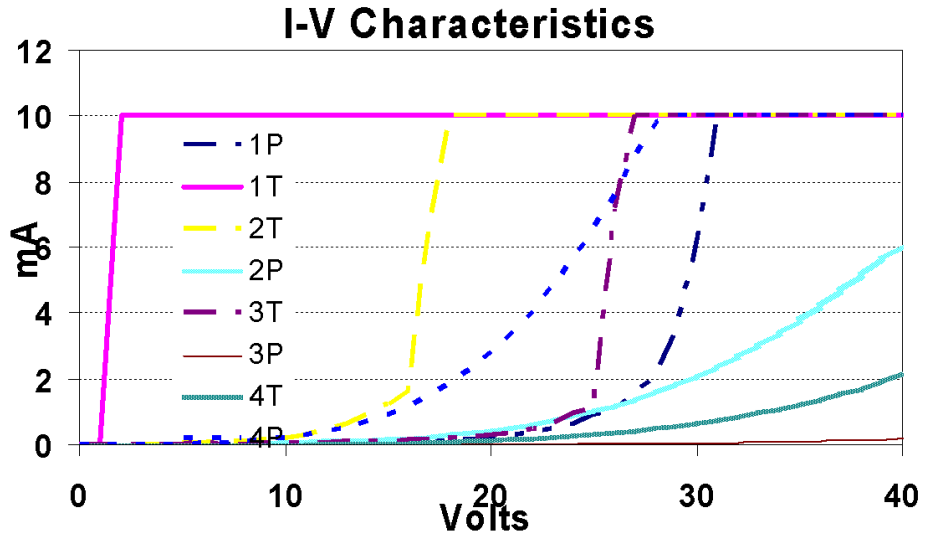


Figure 43: Comparison for the measured I-V characteristics of the parallel plate capacitors with different precursors and processing.

effective routes for improving the break-down strength of the oxide films was found to be treatment in reactive oxygen environments. In this work, the patterned metal oxide films have been treated using oxygen plasma. The equipment was set for treatment at 30 °C, 200 mTorr, 400 W and 50 sccm O₂ for 25 minutes. I-V measurements of the mixed metal oxide films clearly show that oxygen plasma treatment of the patterned oxide films improves their breakdown strength significantly as shown in Figure 44. This is mainly because that oxygen plasma reduces the number of the dangling Ti-O bond on the surface of the film and also densifies the photo-converted film. For the same size 100 micron square oxide feature, it requires approximately 25 times more applied voltage for the oxygen plasma treated sample as compared to sample without plasma treatment to achieve the same leakage current of 10 microamperes through the capacitor. I-V measurement results also show that parallel plate capacitors with larger areas made using the photosensitive metal oxide deposition process have smaller breakdown voltages (see Figure 44). This is believed to simply be due to a higher probability and number of defects from the the spin coating process in the larger metal oxide features which reduce the film electrical quality including the break-down voltage. This problem can most likely be addressed by more careful filtration and preparation of the precursor solutions and the use of more advanced coating methods and

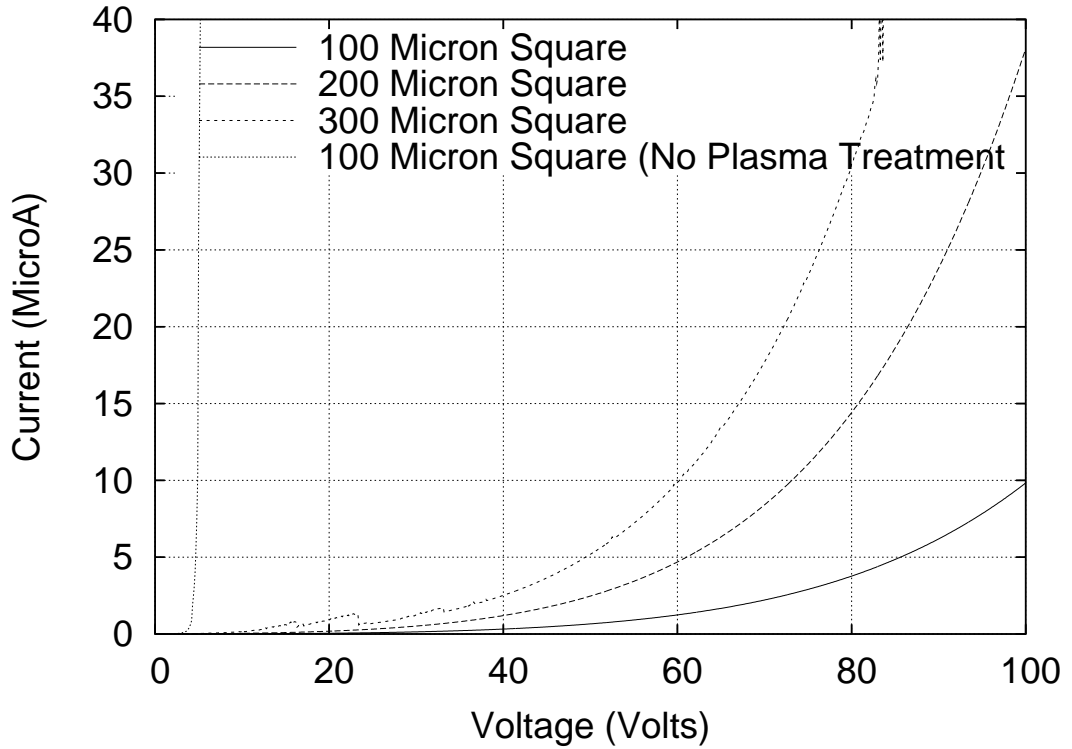


Figure 44: I-V measurement results of parallel plate capacitors made with the mixed metal oxide dielectric which has been processed with and without an oxygen plasma treatment after exposure and development of the oxide pattern.

Table 7: Measured capacitance for parallel plate capacitors with silicon nitride as dielectric layer

Material	Area (cm ²)	Thickness (Å)	Capacitance (nF)	ϵ_r
Silicon Nitride	0.0314	1900	0.6	7.9

equipment.

To make comparison, parallel plate capacitors with silicon nitride as dielectric layer are also fabricated and measured. Table 7 shows the measured capacitance and calculated dielectric constant. Figure 45 shows the measured I-V characteristics of the capacitors. Table 8 summarize the breakdown voltage for the Oxygen plasma treated mixed oxide and silicon nitride when both dielectrics have the same thickness (200nm).

The mixed metal oxide dielectric thin films have also been analyzed using both XPS and FTIR to verify full conversion of the precursors into the desired metal oxide form and

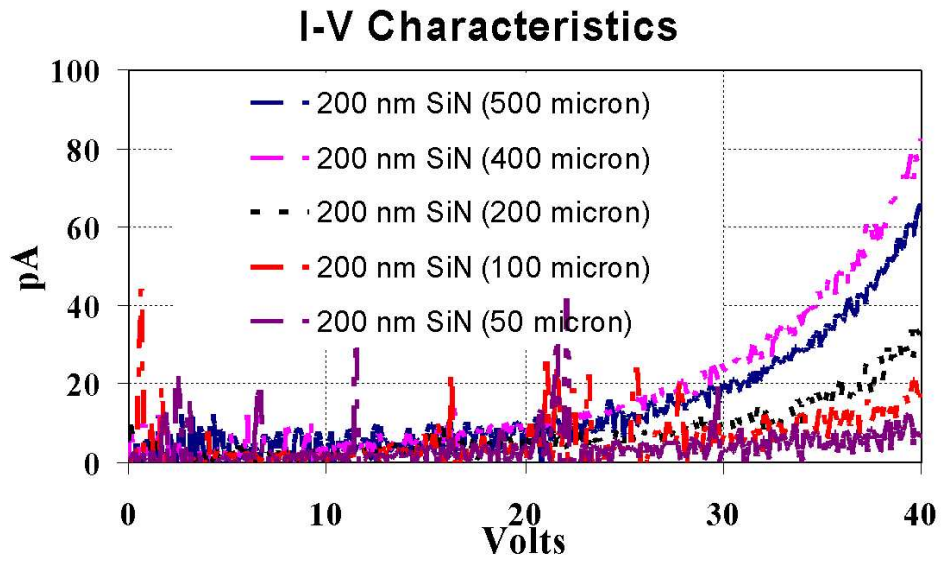


Figure 45: I-V characteristics of the PPCs with silicon nitride as dielectric layer.

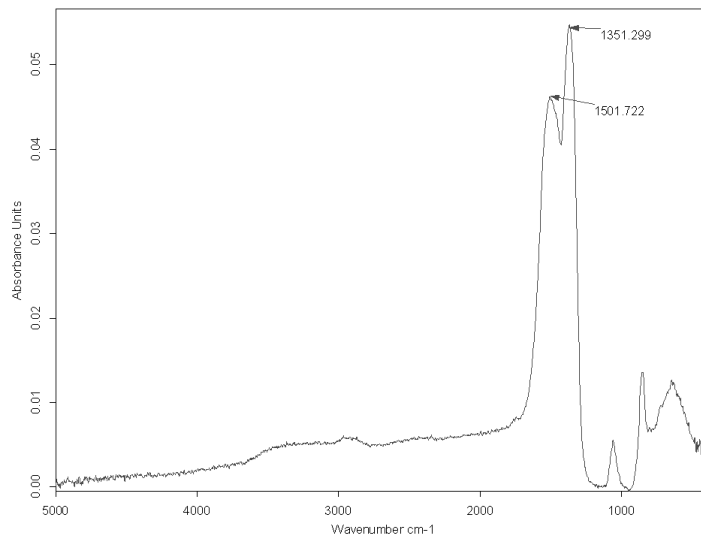


Figure 46: FTIR spectrum result of the metal oxide after plasma treatment.

Table 8: Summary of the measured breakdown voltage for mixed oxide dielectrics and silicon nitride

Sample	Breakdown Voltage (V)
100 Micron Square Mixed Oxide	9
100 Micron Square Plasma Treated Mixed Oxide	42
200 Micron Square Plasma Treated Mixed Oxide	30
300 Micron Square Plasma Treated Mixed Oxide	20
100 Micron Square Silicon Nitride	> 40
200 Micron Square Silicon Nitride	> 40

Table 9: XPS atomic composition of the mixed metal oxide film after plasma treatment

Detector Angle (Degree)	C1s (%)	O1s (%)	F1s (%)	Ti2p (%)	Ba3d5 (%)
45	15.62	26.63	41.60	4.45	11.71
70	11.37	29.50	40.31	5.91	12.91

to check the stoichiometry of the film produced and determine residual carbon contamination levels. FTIR measurements (as shown in Figure 46) of the mixed metal oxide films showed that the peaks associated with CH₂ and CH₃ stretching (2850 -2950 cm⁻¹) which are not observed in the precursor films due to the presence of the organic ligands, are not observed. Table 9 shows the XPS atomic composition of the mixed metal oxide film after plasma treatment. F has been found in the XPS results, this is because the surface absorption/contamination due to the F residue inside the RIE chamber, since deeper analysis of the thin mixed oxide film using EDS (as shown in Figure 47) showing that there is no existence of F in the bulk of the film. XPS results also indicate that the Ba to Ti ratio in the final oxide are essentially equivalent to their original molecular weight ratio of 6:5.

3.3.2.3 Measured Results of MEMS Switches

Measurements of the airbridge type switch were taken using an Agilent 8510 network analyzer. A Thru, Reflection and Line (TRL) calibration was performed to deembed the coplanar line and transition losses. Several membrane geometry designs were realized and measured (as shown in Figure 37). Switches with silicon nitride as dielectrics were also fabricated and measured for comparison purpose. Figure 48 shows the measured result for

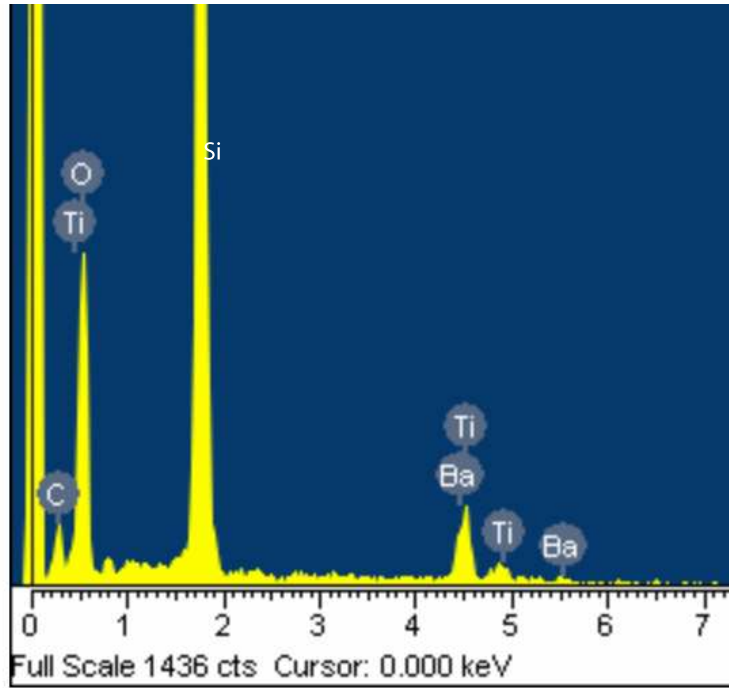


Figure 47: EDS analysis results for the mixed oxide film.

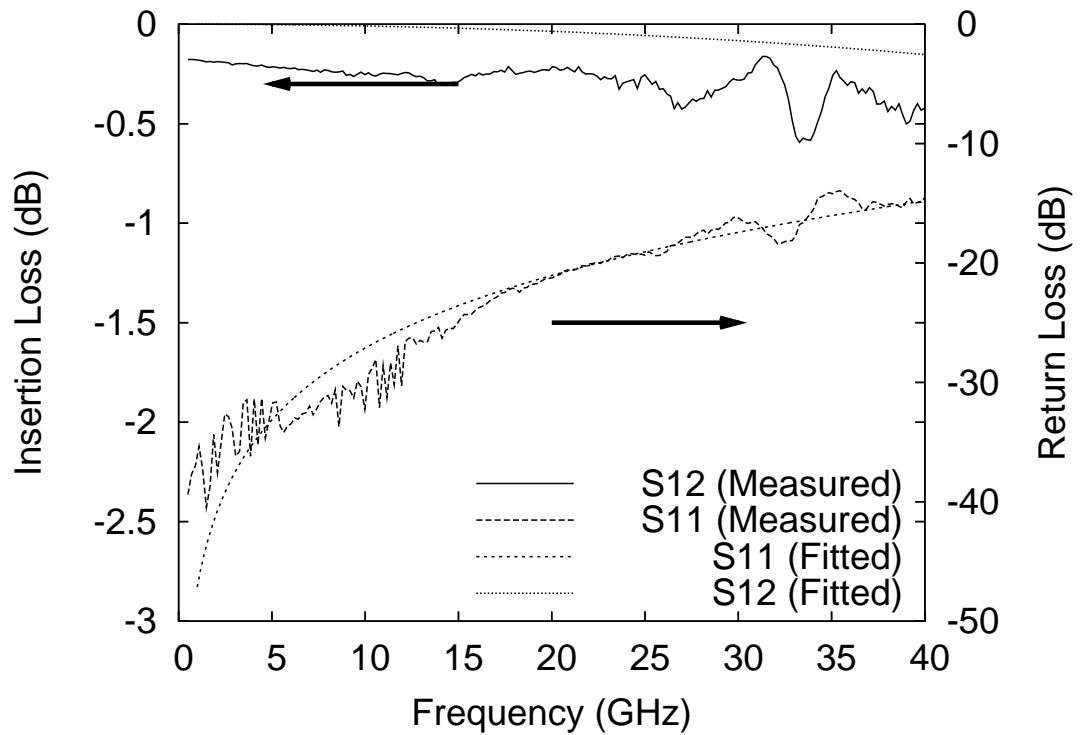


Figure 48: Measured S-parameter results for switch with metal oxide as dielectrics at the UP state.

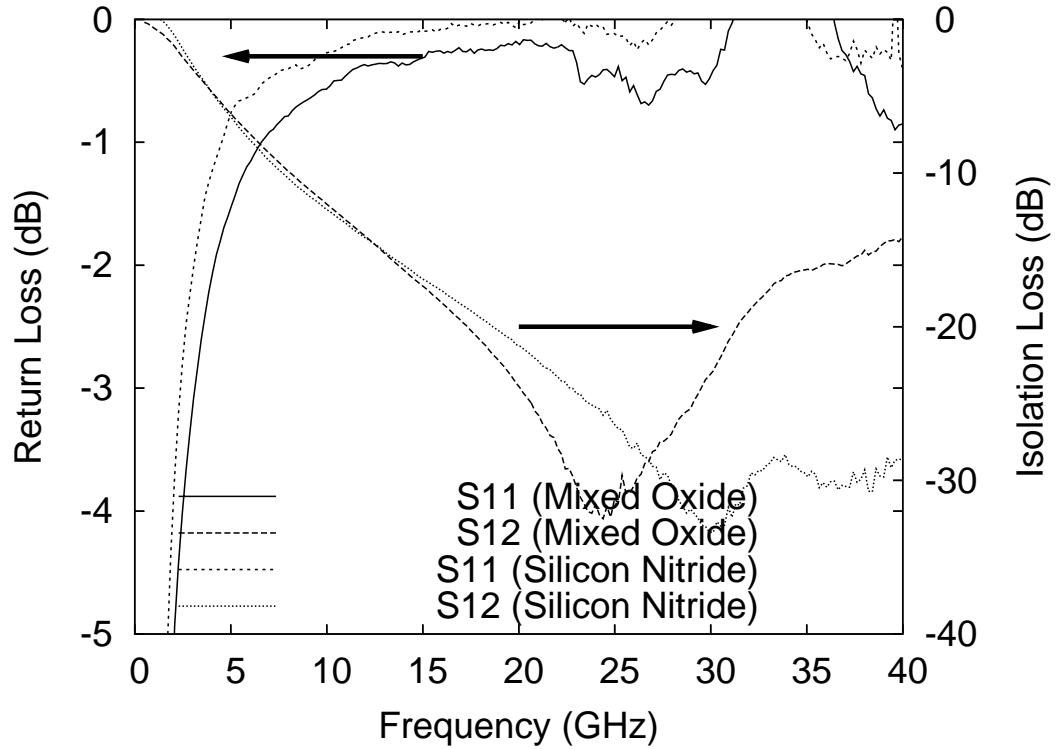


Figure 49: Measured S-parameter results for switch with solid hinge at the DOWN state.

the switch with metal oxide as dielectric on the "Up" state. The measured switches results for the "Down" state are shown in Figure 49 and Figure 50.

The measured results were also curve-fitted using Agilent-ADS with a simple RLC electrical model in order to extract the switch parameters. The model is a series combination of a capacitor, a resistor, and an inductor. Fitted results for the switch with mixed oxide as the dielectric at the down states are summarized in Table 10. The fitted results for the switch with silicon nitride as the dielectric at the down state are summarized in the Table

Table 10: Summary of the measured results for switches with mixed oxide dielectrics on the down state

	Solid Hinge	S-shape Meander Hinge
Resistance (Ω)	0.6	0.5
Capacitance (pF)	3.2	4
Inductance (pH)	13	66
Isolation Loss at 20 GHz(dB)	24	11
Return Loss at 20 GHz(dB)	0.2	1.1

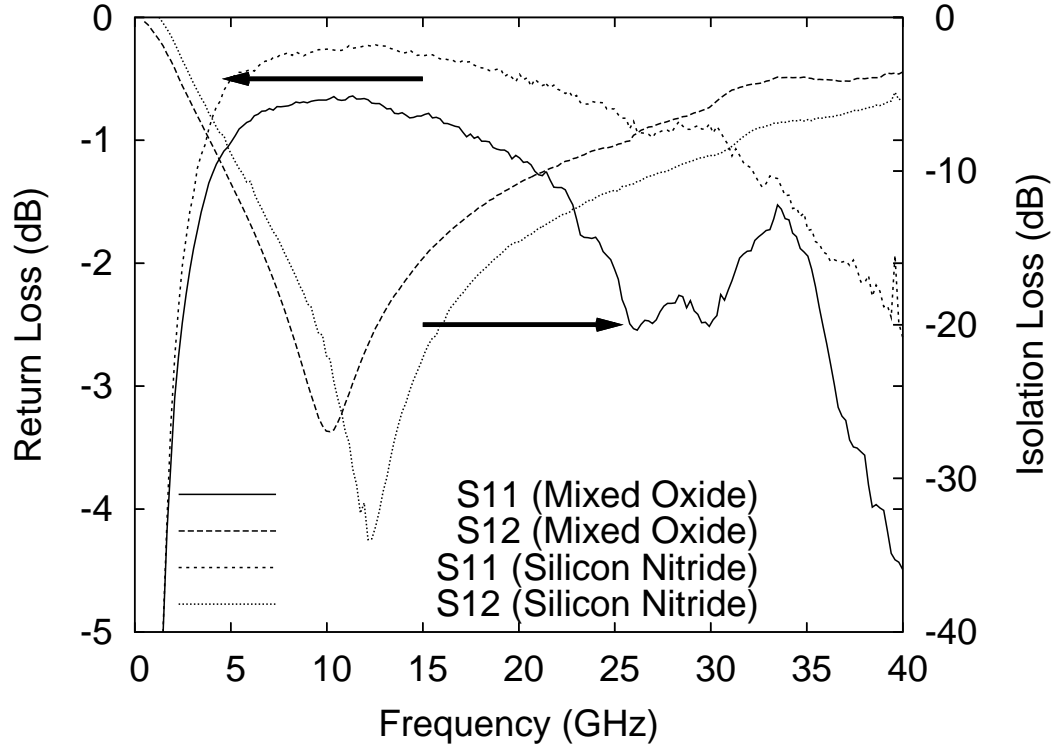


Figure 50: Measured S-parameter results for switch with S-shape meander hinge at the DOWN state.

11. The pull-down voltage was measured to be around 25 V.

From these results, it is observed that the switches with the mixed metal oxide have higher down state capacitance as compared with those of the nitride switches. This is due to the fact that the dielectric constant of the titanium-barium oxide dielectric produced from the photochemical conversion of the metal-organic precursor film is higher than that of the silicon nitride, which results in a larger C_{ON} than that of the plain silicon nitride switch.

Table 11: Summary of the measured results for switches with silicon nitride dielectrics on the down state

	Solid Hinge	S-shape Meander Hinge
Resistance (Ω)	0.5	0.5
Capacitance (pF)	2.1	2.8
Inductance (pH)	13	60
Isolation at 20 GHz(dB)	21	14
Return Loss at 20 GHz(dB)	0.4	0.5

All the switches with metal oxide dielectrics show some isolation improvement compared with the nitride switches at lower frequencies.

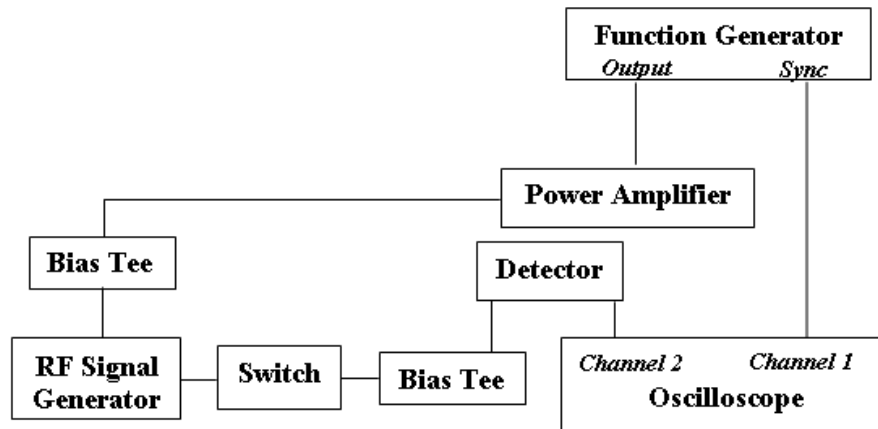


Figure 51: Measurement setup for the reliability test.

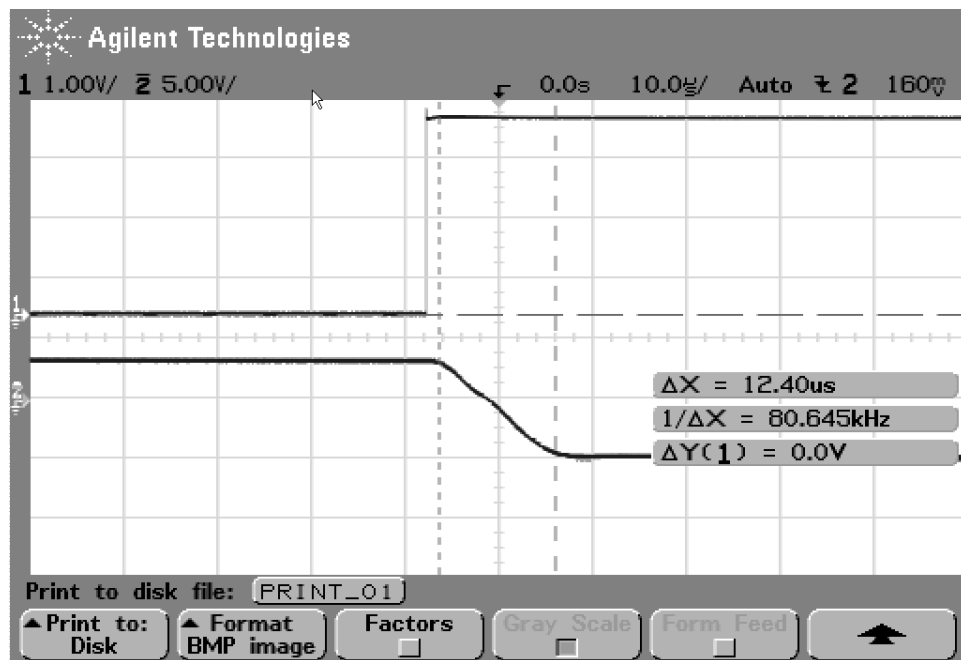


Figure 52: Response of the switch with s-shape meander hinge for the lifetime test.

To further investigate the reliability of the fabricated switch, a lifetime test was performed. The measurement setup is shown in Figure 51, response for the measured switch with s-shape meander hinge is shown in Figure 52 and Figure 53 shows the response for

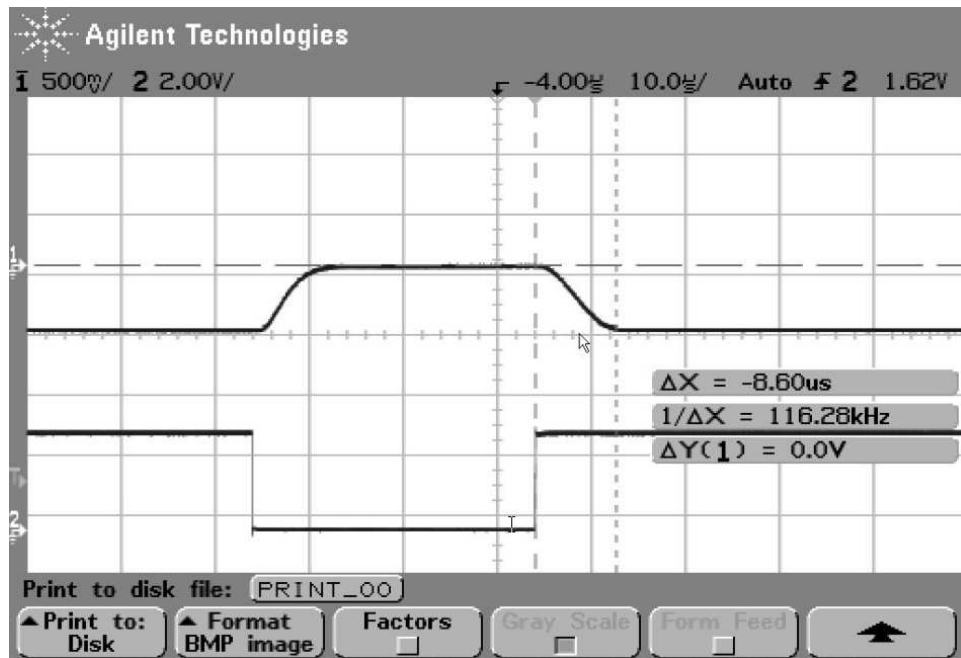


Figure 53: Response of the switch with solid hinge for the lifetime test.

the measured switch with solid hinge. The measurement method for monitoring the switch actuation is to apply a Continuous Wave (CW) signal to the switch and measure the modulated RF envelope resulting from the switch actuation [31]. For the measurement, an Agilent 33220A 20 MHz function/arbitrary waveform generator was used to generate a DC square wave signal, and a Trek power amplifier (model 603) was used to amplify the DC signal. The DC bias was applied to the switch through a bias tee. The switches were probed with a Cascade probe station. The output RF probe was connected to a bias tee and an Agilent 8473C crystal detector. The crystal detector provided a DC voltage proportional to the modulated RF envelope and representative of the switching behavior of the device under test. The detected signal is applied to an Agilent 54622A Oscilloscope. During measurement, the RF signal was 15 GHz with about 10 dBm of RF power and the generated square wave frequency was 1 KHz. The measured switch speed was around 8.6 to 12.4 μ S as shown in Figures 52-53. The switches were cycled for 2 days in the lab with no performance deterioration. This means that a minimum of 340 million cycles in an open air environment (switch is not packaged) was achieved.

3.3.3 Conclusions

In this chapter, a new approach for fabricating low cost RF MEMS switches has been developed using photodefinable metal-oxide dielectric layers. It provides a new method for the deposition and patterning of high quality dielectric thin films of MEMS capacitive switches without the using of PECVD and RIE equipments. Good metal oxide dielectric thin films with higher dielectric constants than conventional silicon nitride films and high breakdown voltage have been achieved. The switches discussed in this work were fabricated and measured demonstrating the feasibility of using this metal-organic precursor processing approach. Better isolation at low frequencies and higher down state capacitances were achieved using the photo-patterned oxide dielectrics as compared to conventional switches using a silicon nitride dielectric. A lifetime greater than 340M cycles with no package was observed, demonstrating the robustness of the mixed metal oxide dielectric materials made using this new processing methodology.

CHAPTER IV

RF MEMS SWITCH WITH LCP SUBSTRATE

In this chapter, an RF MEMS switch developed on a low cost, flexible liquid crystal polymer (LCP) substrate is presented. LCPs very low water absorption (0.04%), low dielectric loss and multi-layer circuit capability make it very appealing for RF system-on-a-package (SOP) applications. Here, the fabrication of capacitive MEMS switch on an LCP substrate and its characterization and properties up to 40 GHz are presented.

4.1 Introduction

As discussed in the previous chapters, low cost MEMS switches are prime candidates to replace the conventional GaAs FET and p-i-n diode switches in RF and microwave communication systems, mainly due to their low insertion loss, good isolation, linear characteristic and low power consumption. In most MEMS switches reported so far, all switches are fabricated on semiconductor substrates like Silicon [34, 70, 105]. Miniaturization, portability, cost and performance have been the driving force for the evolution of packaging and System-On-a-Package (SOP) approach in RF, microwave and millimeter wave applications. Liquid crystal polymer (LCP) provides the all-in-one solution for such integration approach in terms of high quality dielectric for high performance multiband passive design, excellent substrate for heterogeneous SOP integration as well as for MEMS structures. Furthermore, low loss and low power MEMS switches fabricated on LCP enable the implementation of multi-band and reconfigurable modules.

In this chapter, a capacitive RF MEMS switch with silicon nitride as dielectric layer on LCP substrate is presented for the first time. It is well known that organic substrates are typically not as smooth as semiconductor ones, and therefore special consideration must be given when developing MEMS devices. Clamped-clamped (air-bridge-type) coplanar waveguide (CPW) switches with a membrane size of $100\mu\text{m}\times 200\mu\text{m}$ and various hinge geometries

(solid and meander shaped) were fabricated on LCP substrates using a simple four mask low-temperature process that minimizes the surface roughness and assures good switch performance. The measured DC and microwave performance of the airbridge switches for a given hinge geometry has been reported at this stage.

4.2 Properties of LCP

Digital and RF analog circuits require increasing operating frequencies, increased levels of integration density and maintaining low power consumption and low cost. One material that may offer a solution is Liquid Crystal Polymer (LCP). LCP is a material whose mechanical strength, adhesion to copper, and via drilling/metallization have all recently been optimized to enable its use in microwave circuit construction [102]. LCP's combination of being a low cost material with the best packaging characteristics of any polymer has generated great interest in using it as a dielectric substrate and packaging material for mm-wave applications. Previous literature has described the numerous benefits of LCP [37, 44, 119]:

- Excellent high-frequency electrical properties (stable ϵ_r and low loss [$\tan \delta=0.002-0.004$] for $f < 35$ GHz) [46, 132, 133],
- Quasi-hermetic (water absorption $< 0.04\%$) [24],
- Low cost ($\sim \$5/\text{ft}^2$ for 2-mil single-clad low-melt LCP) [66],
- Low xy coefficient of thermal expansion (CTE), which may be engineered to match metals or semiconductors,
- Naturally non-flammable (no need to add halogens \Rightarrow environmentally friendly),
- Recyclable,
- Flexible for conformal and/or flex circuit applications,
- Multilayer all-LCP lamination capabilities to create multilayer LCP RF modules,
- Relatively low lamination processing temperature (~ 285 °C),
- Low dielectric constant ($\epsilon_r = 3.16$) for use as an efficient antenna substrate [109].

The use of LCP as a microwave circuit substrate is not a new idea. It has been around in thin film form since the early 1990s when it was first recognized as a candidate for microwave applications [19, 45, 46]. However, early LCP films would easily tear and were difficult to process. Film uniformity was not acceptable and poor LCP-to-metal adhesion and failure to produce reliable plated through holes (PTHs) in LCP limited the capabilities for manufacturing circuits on it. Devising and optimizing LCP surface treatments and via drilling and de-smearing techniques were also necessary to bring the material to a state where circuits on it could be manufactured with confidence. Much work has focused on methods to improve these fabrication difficulties [12, 16, 47, 50, 102–104, 124].

A unique extrusion process, surface treatments, and experiments with laser, chemical, and Reactive Ion Etch (RIE) gases have been used to overcome its previous process limitations [66, 104, 124]. LCP is nearly hermetic, has very good electrical properties ($\epsilon_r = 2.9\text{-}3.0$, $\tan\delta = 0.002\text{-}0.003$), is recyclable, has a wide range of CTE (0-30 ppm/C), has excellent chemical resistance, is flexible, and it is capable of multilayer lamination. For multilayer LCP circuits, a 1 mil low melting temperature (290°C) LCP layer can be used to bond high melting temperature (315°C) LCP core layers which typically come in 2 - 4 mil thicknesses (Modulus behavior of LCP with temperature is shown in Figure 54). Electrical properties of the two types are the same. Thus, compact, vertically integrated architectures performing as the substrate and package may be realized in LCP material. And the cost of LCP (5/ft²) [132], though not yet competitive with FR-4, is already reasonable and should continue to drop as production levels grow. Several single measurements have been reported showing that LCP has low loss [108, 121, 132]. The loss characterization of LCP transmission lines up to W band provides an excellent insight of its potential for mm-wave applications. Conductor backed CPW (CB-CPW) transmission lines have been fabricated on 2 mil LCP substrates with measured insertion loss of 2.35 dB/cm at 110 GHz [108].

4.3 RF MEMS Switches using LCP Substrate

High C_{ON}/C_{OFF} ratio is very critical for RF MEMS capacitive switches. In order to get high capacitance when the switch is at the down state, good contact between the switch

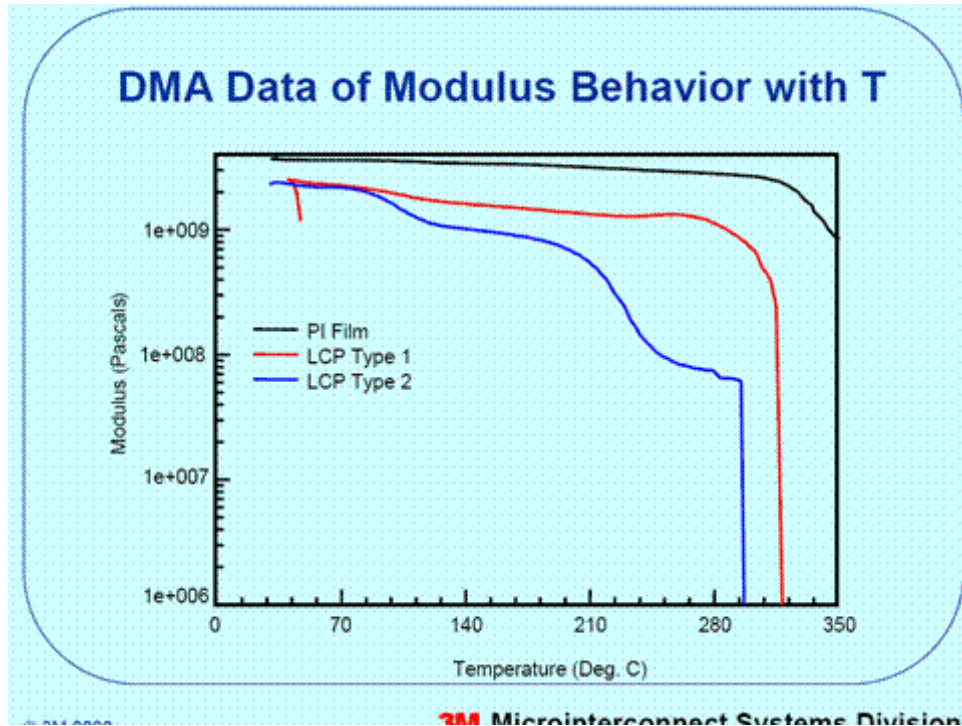


Figure 54: Modulus behavior of LCP with temperature.

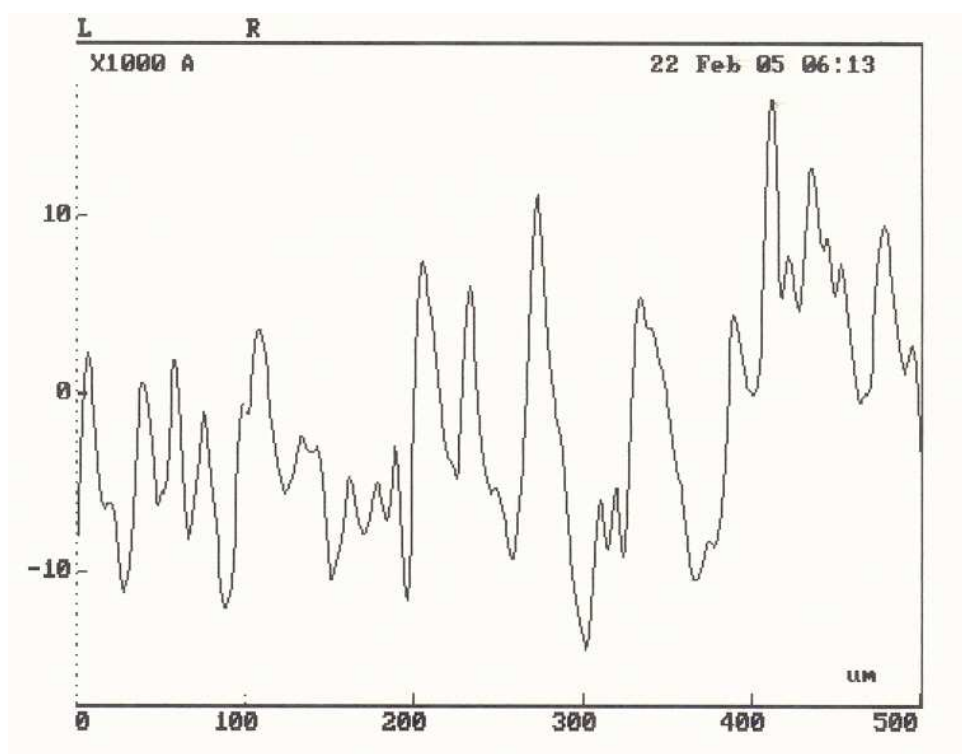


Figure 55: Surface roughness of bare LCP substrate.

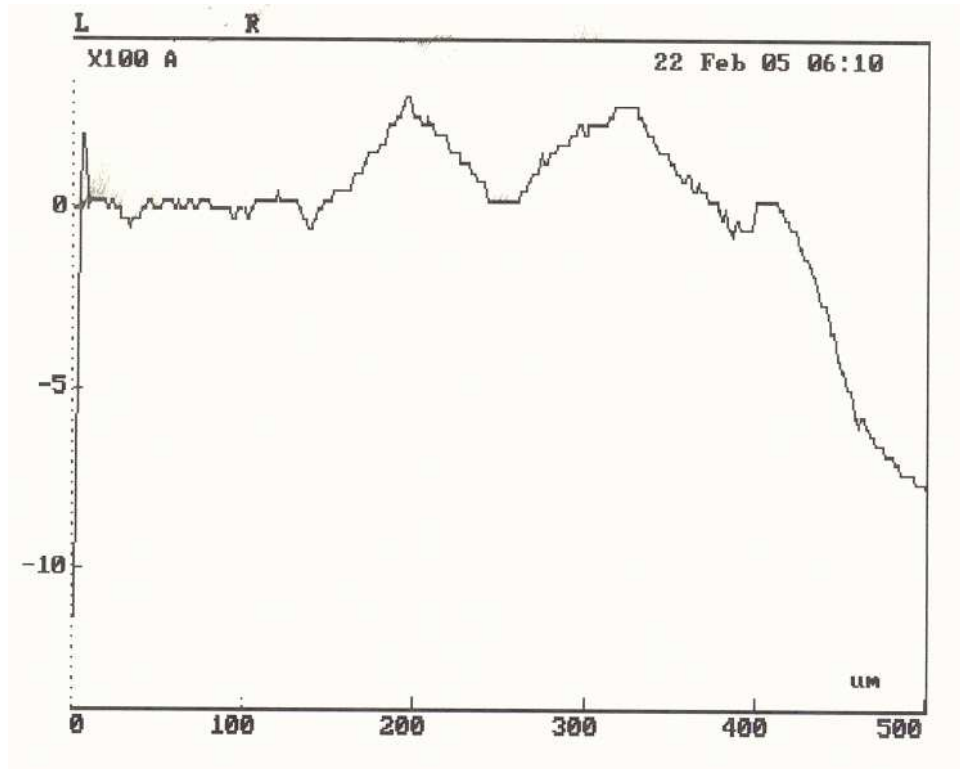


Figure 56: Surface roughness of LCP substrate coated with polyimide layer.

membrane and bottom signal line is needed. However, the surface roughness of bare LCP normally is around 0.6 to 1 μm as shown in Figure 55, and thus, decrease the performance of the switch at ON state (the membrane is on the Down position). Two different methods have been used to smooth the surface roughness of LCP [93,118]. In the first method, a 3 μm PI2610 polyimide is first spun on LCP to planarize the surface to minimize the roughness and get surface roughness was measured around 500 \AA as shown in Figure 56. In the second method, LCP was polished using lap master polisher with 0.06 μm slurry for 2 hours and the surface roughness is measured around 600 \AA as shown in Figure 57. To fabricate MEMS switches on LCP substrate, a simple four mask process is used as shown in Figure 58. The CPW signal lines were fabricated by evaporating Ti/Au/Ti (300 \AA /5000 \AA /300 \AA), here, a little bit thicker bottom metal layer was patterned to improve the surface roughness of the substrate. Figure 59 shows the patterned electrode on bare LCP, where the surface roughness of the substrate is clearly seen. Figure 60 shows the patterned metal on surface roughness improved LCP layer. 3000 \AA PECVD Si_3N_4 layer was patterned between the

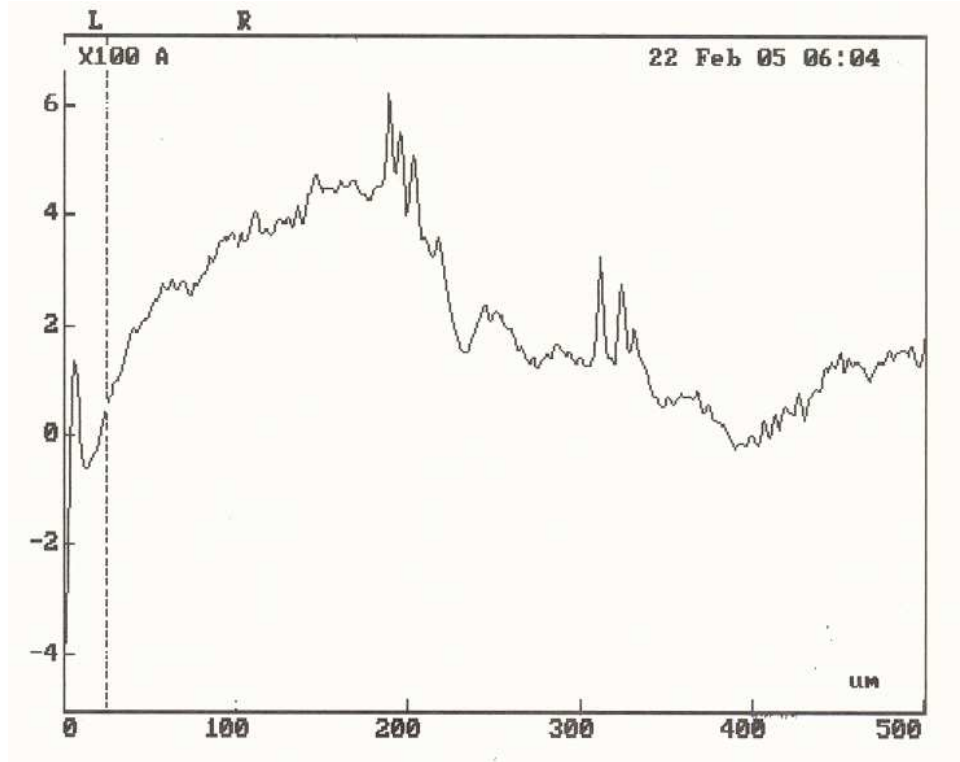


Figure 57: Surface roughness of polished LCP substrate.

Table 12: Measured s-parameter summary for the switch on different substrates

Substrate	Insertion Loss (dB)	Return Loss (dB)	Isolation Loss (dB)	Return Loss (dB)
LCP/PI	0.08	18	17.7	0.1
LCP	0.05	20.6	20.8	0.05

membrane and the signal line. A $1.8 \mu\text{m}$ thick photoresist (Shipley 1813) was spin coated and patterned to create the air-gap. Ti/Au/Ti ($300\text{\AA}/3000\text{\AA}/300\text{\AA}$) seed layer was then evaporated, patterned and electroplated. Finally, after removing the sacrificial photoresist layer with a resist stripper, a critical point drying process was used to release the switches.

Scanning Electron Microscope (SEM) picture of the fabricated air-bridge type CPW switch structure with a $1.2 \mu\text{m}$ thick gold membrane, a $1.8 \mu\text{m}$ air-gap and a membrane size of $100 \times 200 \mu\text{m}^2$, is shown in Figure 61.

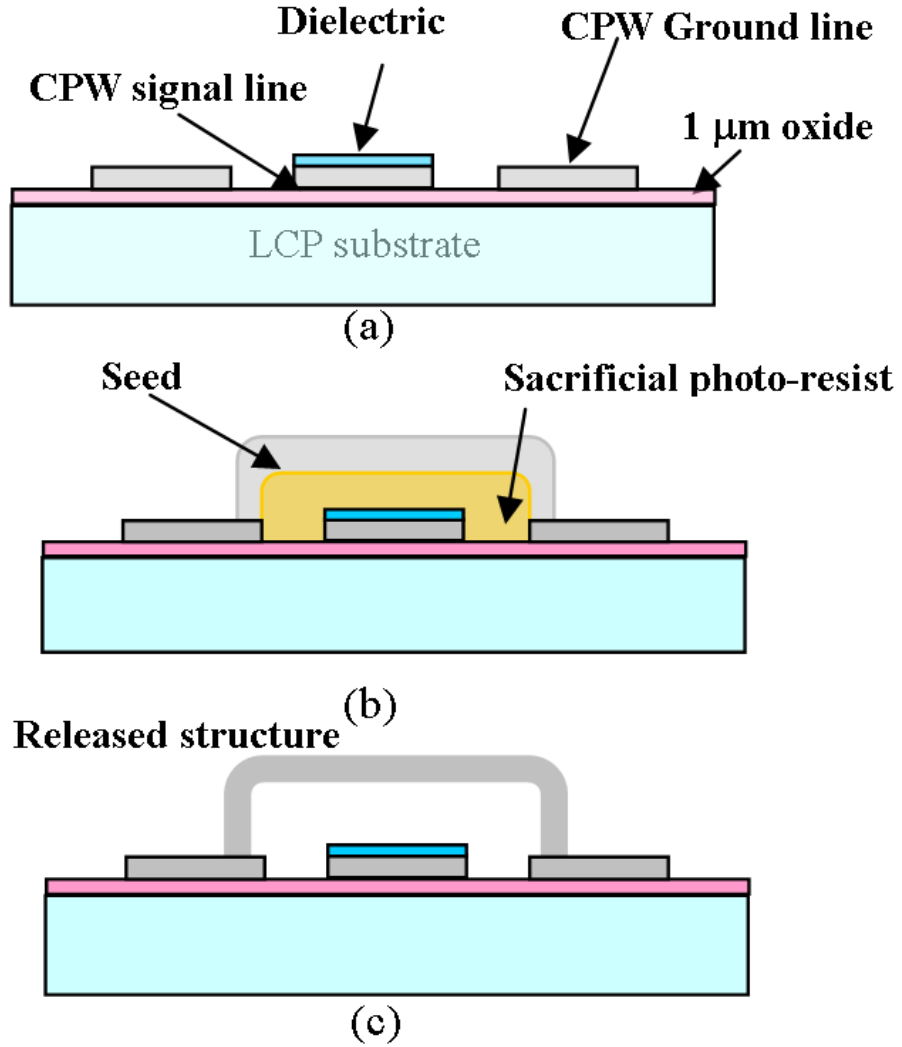


Figure 58: Fabrication process of a switch on LCP substrate.

4.4 Measured Results

Measurements of the air-bridge type switch were taken using an Agilent 8510 network analyzer. A TRL calibration was also performed to deembed the coplanar line and transition losses. Measured results for the nitride switches with LCP coated with polyimide substrate and polished LCP are shown in Figure 62. The pull-down voltage was measured to be between 25 and 35 volts. For the LCP switch with the 3 μm polyimide intermediate layer, when the switch is activated, the isolation is around 18 dB at 20 GHz and $C_{ON}=3.5$ pF, while the return loss is around 0.1 dB at 20 GHz. When the switch is in the UP position, the insertion loss is around 0.08 dB at 20 GHz and the return loss is 18 dB at 20 GHz

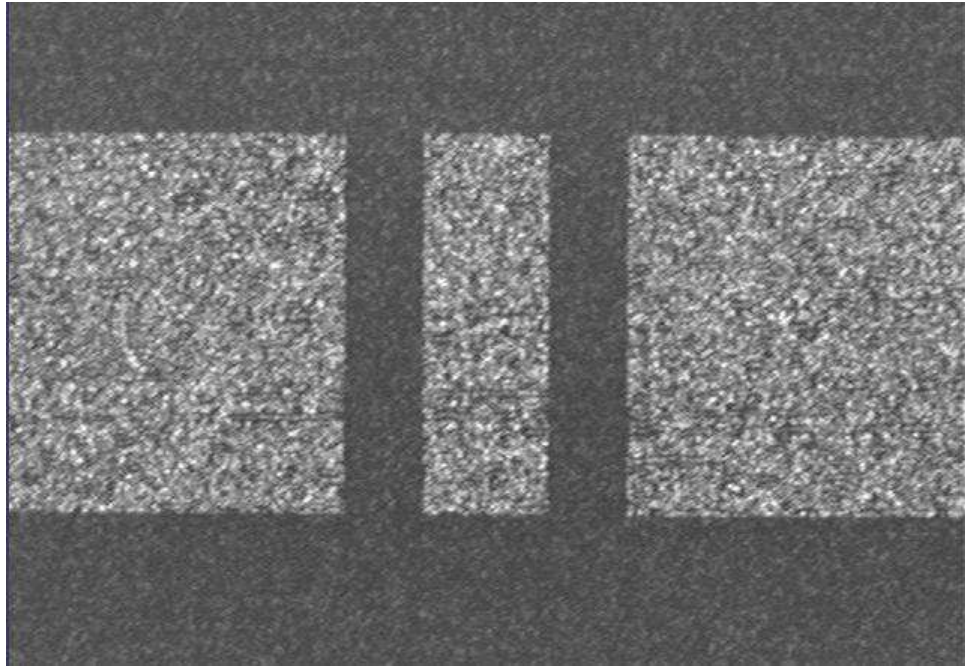


Figure 59: Patterned metal on bare LCP substrate.

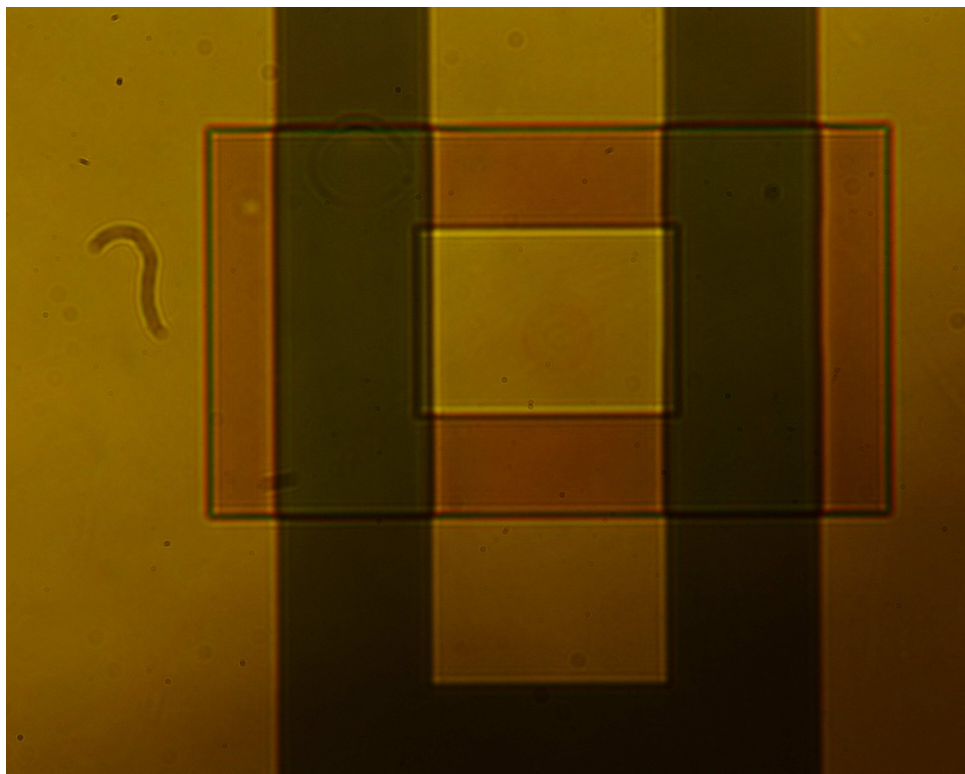


Figure 60: Patterned metal on surface roughness improved LCP substrate.

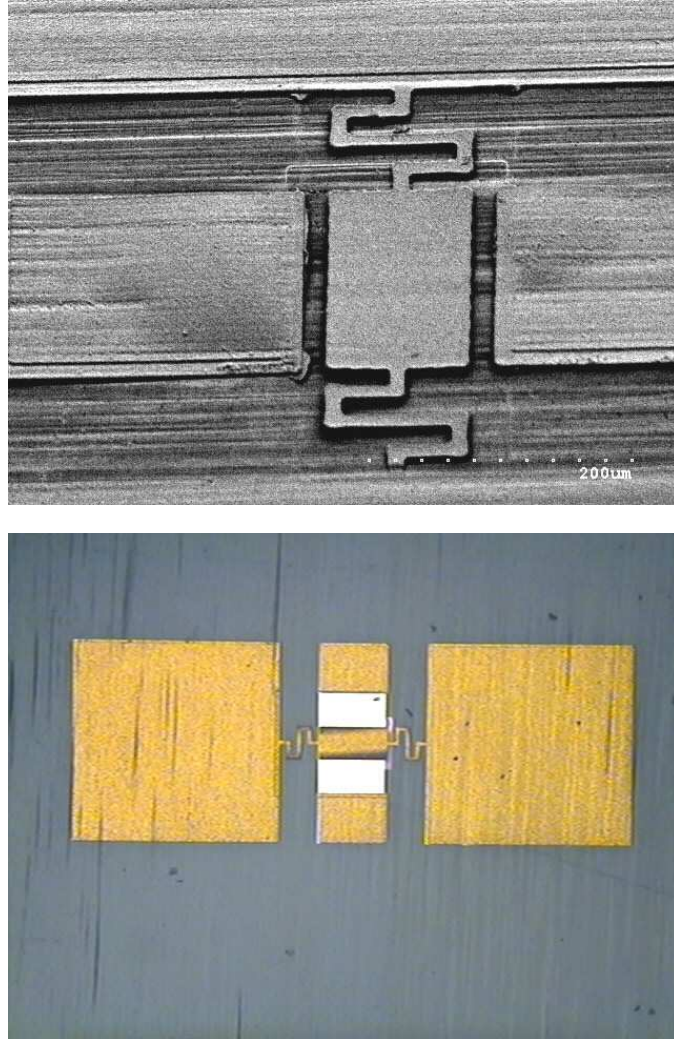


Figure 61: Photos of fabricated switch on LCP/PI substrate (top) and polished LCP substrate (bottom).

corresponding to a $C_{OFF}=35$ fF. For the switch on the bare polished LCP, when the switch is activated, the isolation is around 20.8 dB at 20 GHz and $C_{ON}= 3$ pF while the return loss is around 0.05 dB at 20 GHz. When the switch is in the UP position, the insertion loss is around 0.1 dB at 20 GHz and $C_{OFF}=30$ fF while the return loss is 20.6 dB at 20 GHz. All the measured results and fitted data are summarized in Table 12 and 13. The fitted data shows that $L=35$ pH and $R=0.3 \Omega$. For both switches, a silicon nitride layer was deposited by PECVD for 30 minutes. The different C_{ON} was achieved between the switches with different substrates is due to the small difference in the thickness of silicon nitride (2600 Å vs. 3000 Å), which is caused by the slightly different deposition rate of

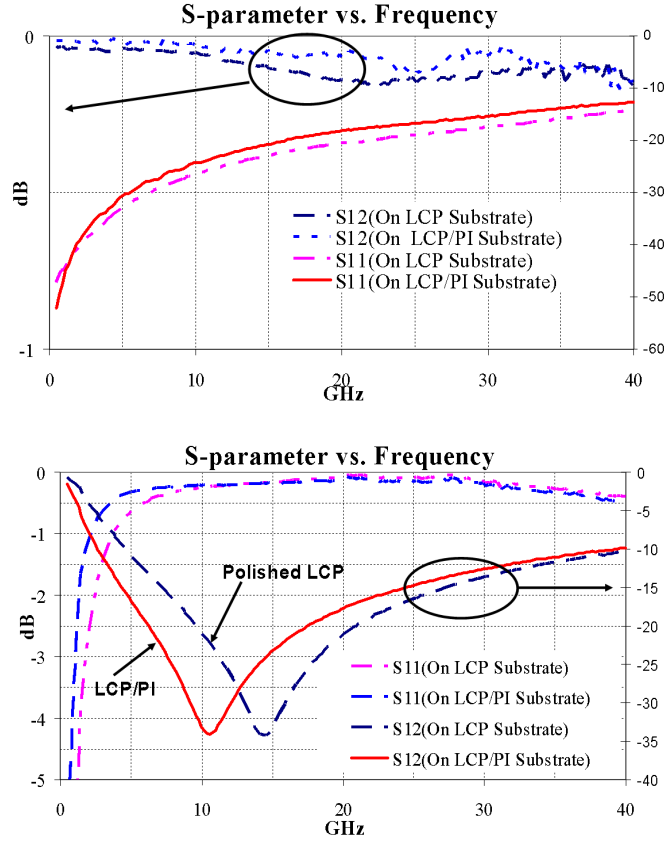


Figure 62: Measured S-parameters of the fabricated switch as shown in Figure 55 on up state (top) and down state (bottom) .

silicon nitride for different substrates. All airbridge switches with LCP substrate have very low insertion loss, this is probably partly due to the low dielectric loss tangent of the LCP substrate. Also, to get stable and accurate measurement results, it is very important to get good measurement contacts since the LCP substrate is flexible.

Table 13: Fitted capacitances for the measured results of the switches.

Substrate	Up state	Down state
LCP/PI	C=35 fF	C=3.5 pF
LCP	C=30 fF	C=3 pF

4.5 Conclusions

In this chapter, RF MEMS capacitive switches on flexible LCP substrate have been developed. From the results, the switch on LCP substrate has extremely low loss. It is flexible and can be compatible with an appropriate wafer level package. It enables the integration of reconfigurable architectures on LCP for 3D RF front ends such as reconfigurable antenna arrays with tunable frequency bands and polarizations. It also shows that the switch on LCP substrate can be a low cost/enhanced performance alternative to the RF MEMS capacitive switches on hard fragile substrates like silicon.

CHAPTER V

TUNABLE MEMS SWITCHES WITH BARIUM STRONTIUM TITANTATE (BST) DIELECTRICS

In this chapter, a tunable RF MEMS switch used for the development of reconfigurable antennas that is fabricated on sapphire substrate with a BST dielectric is presented. BST dielectric is deposited by a combustion chemical vapour deposition (CCVD) technology. BST has a very high dielectric constant (>300) making it very appealing for high performance RF MEMS capacitive switches. The tunable dielectric constant of BST provides a possibility of making linearly tunable MEMS capacitor-switches. Here for the first time a capacitive tunable RF MEMS switch with a BST dielectric and its characterization and properties up to 40 GHz are presented.

5.1 Introduction

RF MEMS switch technology has been introduced during the last 10-15 years as a prime candidate to replace the conventional GaAs FET and p-i-n diode switches in RF and microwave communication systems. It has also provided the way for the development of novel revolutionary RF circuits like low cost reconfigurable and smart antenna systems on-chip that can be used in the next generation of broadband, wireless, and intelligent communication and radar systems. A MEMS-switched reconfigurable antenna is one that can be dynamically reconfigured within a few microseconds to choose different polarizations (as shown in Figure 63) or to serve different applications at drastically different frequency bands, such as communications at L-band (1-2 GHz) and synthetic aperture radar (SAR) at X-band (8-12 GHz). Recently, many researchers have been focusing on the development of miniaturized, low power and low cost, RF/Microwave circuits with RF MEMS switches [70, 105, 113].

MEMS switches have been used in different RF circuit applications: tunable antennas,

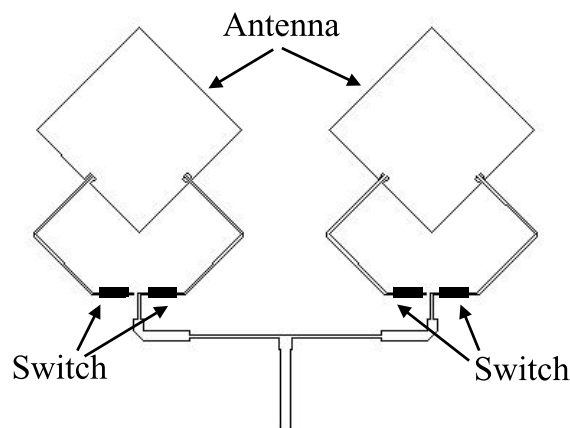


Figure 63: Reconfigurable antenna in terms of polarization with MEMS switches.

tunable microwave filters, tunable phase shifters, and tunable matching networks. Microwave and millimeter-wave technology that offers wide tunability is essential for today's cost-driven commercial and military industries. In order to meet the above requirements, recently, micromachined tunable capacitors have been shown to have an adequate Q-factor when they are fabricated in either an aluminum [126, 127] or a polysilicon [123] surface micromachining technology as discussed in chapter I. In addition, a three-plate structure with a wide tuning range was reported [20] in 1998. Since tunable capacitors are enabling components for high frequency systems, two approaches have been studied to make such components. One is a chemical approach that improves properties of the materials, and the other is a physical approach that controls the gap or area of the dielectric layer for variable capacitance. MEMS switch precise, micrometer-level movements make them ideal drives for the physical approach.

A MEMS-based switching diaphragm has been used as a variable capacitor [32]. Although, the tunability of this component was very impressive because a lossless, $2 \mu\text{m}$ airgap was used above the dielectric layer, the range of this variable capacitance was limited when the top membrane collapsed onto the dielectric layer.

One key factor of MEMS switches is input-output signal isolation in the down state. Traditional MEMS switches use Si_3N_4 as dielectric material; its lower dielectric constant

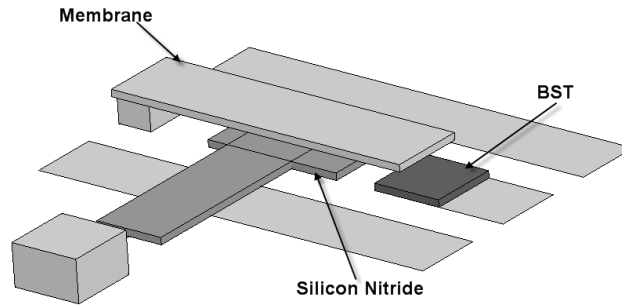


Figure 64: Close-up view of a single BST MEMS switch.

(~ 7) limits its application at very lower frequencies. In order to further improve the performance of MEMS switches, higher C_{ON}/C_{OFF} ratio and thus larger down state capacitances are required. Emerging BST thin film technology has been investigated for enhancing RF-MEMS capacitive switches due to its high dielectric constant (>200) in [55]. The switch provides better isolation than the nitride switch of the same type, but the isolation value drops considerably (< 15 dB) below 5 GHz. This is because only the partially contact between the top membrane and BST layer is achieved to avoid the breakdown of the BST using a low actuation voltage. In addition, no analog tuning capability was reported in [55].

In this chapter, a highly compact low-loss up to 40 GHz and linearly tuned capacitive cantilever MEMS switch (as shown in Figure 64) using high quality BST as the dielectric layer is reported for the first time. It provides continuous (analog) tunability of the capacitor after the MEMS switch has been pulled down, due to the voltage controlled dielectric constant properties of the BST material. The developed switch can be used to build very compact digital capacitor banks with enhanced analog tuning for a variety of reconfigurable antenna systems and other networks. A special MEMS design with a separate actuation electrode is considered to provide tunability of the switch and to prevent the breakdown problem of the BST. Clamped-free (cantilever-type) coplanar waveguide (CPW) switches with a contact area of $100 \mu\text{m} \times 200 \mu\text{m}$ and various hinge geometries (solid and meander shaped) were fabricated on sapphire substrates using a five mask process [115]. The measured DC and microwave performance of the cantilever switches for a given hinge geometry has been reported at this stage. The BST composition used did not exhibit hysteresis

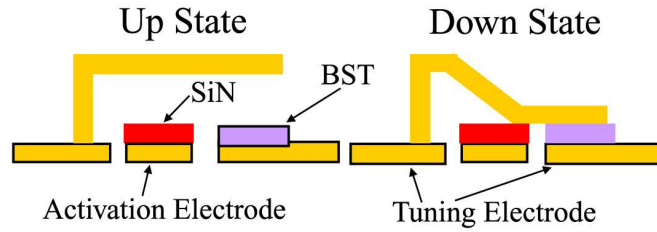


Figure 65: RF tunable cantilever switch using BST thin film and separate actuation electrode in both switch up and down states.

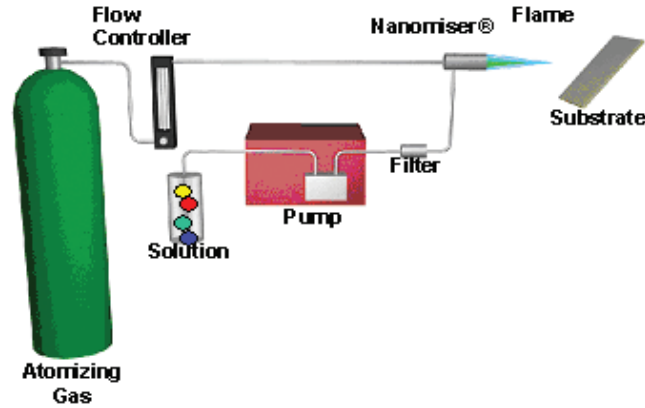


Figure 66: Schematic representation of the CCVD system.

(charging) from other applications.

5.2 Design and Fabrication

Figure 65 shows the designed CPW cantilever capacitive switch in both up and down switch states. The switch is designed for a very low capacitance between the top membrane and the bottom signal line in the up state. Once voltage is applied through the actuation electrode, the top membrane is deflected due to electrostatic forces and as it touches the bottom electrode, a larger metal-insulator-metal capacitor is formed. The down-state capacitance of the design is highly enhanced by the use of high dielectric constant BST material.

5.2.1 Deposition and Properties of BST Thin Film

Ferroelectric material is a category of material with reorientable spontaneous polarization, a sub-category of pyroelectric materials. Because of their high dielectric constant, the electric field dependence and the temperature dependence of their dielectric constant (the variation

in capacitance over the range of $-20\text{ }^{\circ}\text{C}$ to $+100\text{ }^{\circ}\text{C}$ can be as high as 35% or even lower than 5% depending on the composition), and high breakdown voltage, ferroelectric materials have a wide range of applications such as IR detection, high-density capacitors, DRAMs, non-volatile ferroelectric memory, and high frequency microwave devices. $\text{Ba}_x\text{Sr}_{1-x}\text{TiO}_3$ (BST) has been the subject of extensive investigation for these applications. The $\text{Ba}_{0.45}\text{Sr}_{0.55}\text{TiO}_3$ films were prepared by using nGimat's proprietary combustion chemical vapor deposition (CCVD) process as shown in Figure 66 [38–42]. In the CCVD process, precursors, which are the metal-bearing chemicals used to coat an object, are dissolved in a solution, which typically is a combustible fuel. This solution is atomized to form microscopic droplets by means of the proprietary Nanomiser® Device. These droplets are then carried by an oxygen stream to the flame where they are combusted. A substrate is coated by simply drawing it in front of the flame. The heat from the flame provides the energy required to vaporize the droplets and for the precursors to react and deposit (condense) on the substrates. One of the strengths of the CCVD process is the variety of complex materials and substrates that can be utilized, The CCVD process offers significant advantages over traditional CVD/PVD techniques [1], including:

- The quality production of highly-tailored and complex material solutions that cannot be commercially achieved with CVD/PVD processes,
- The elimination of energy intensive, highly specialized and expensive equipment (e.g., vacuum chambers, reaction furnaces and chemical scrubbers),
- Continuous manufacturing capability currently unavailable under competing CVD/PVD batch technologies,
- The use of low cost and environmentally friendly precursors and other process chemicals.

5.2.2 Fabrication of the Switches

Figure 67 shows the fabrication flow of the BST switch. Due to the high growth temperature of BST and the wafer temperature ($900\text{ }^{\circ}\text{C}$), a platinum electrode is used as the bottom

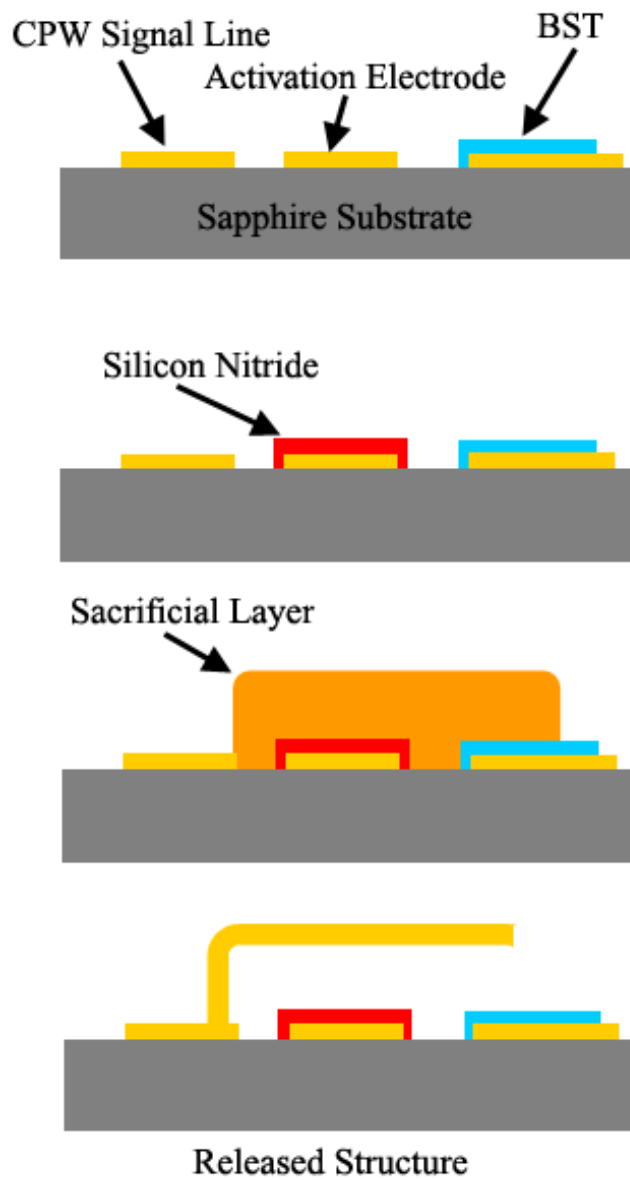


Figure 67: Fabrication process flow of BST MEMS switches.

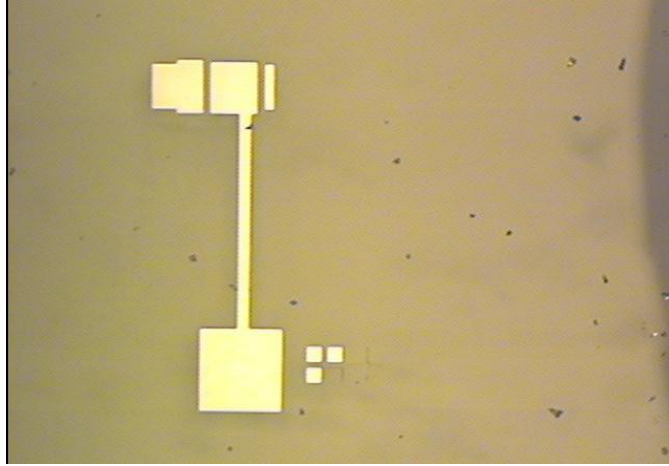


Figure 68: Microscope photo of the patterned Pt layer using lift off process.

electrode in the BST thin film deposition. Since Pt is very hard to pattern using wet etching, a lift off process is first used to pattern Ti/Pt ($200 \text{ \AA}/1000 \text{ \AA}$) before the BST deposition. Figure 68 shows the Pt pattern after using the lift off process. The BST layer was then patterned and etched in a diluted HF solution with an etching rate of 500 \AA per minute. A 2000 \AA Silicon Nitride layer was then deposited by plasma enhanced chemical vapor deposition (PECVD) and patterned using reactive ion etcher (RIE) for the actuation electrode. Since the silicon nitride layer can not survive the high deposition temperature of the BST layer, the silicon nitride layer was patterned after the deposition of BST layer. A 2 \mu m thick photoresist (1813) was then spin coated and patterned to create the air-gap. A Ti/Au/Ti ($200 \text{ \AA}/3000 \text{ \AA}/200 \text{ \AA}$) seed layer was then evaporated, patterned and electroplated. Finally, after removing the sacrificial photoresist layer with resist stripper, a critical point drying process was used to release the switches.

A Scanning Electron Microscope (SEM) picture of the fabricated cantilever type CPW switch structure with a 1.2 \mu m thick gold membrane, a 2 \mu m air-gap and a contact area of $100 \times 200 \text{ \mu m}^2$, is shown in Figure 69. Figure 70 shows the close-up view of the membrane and BST area of the switch.

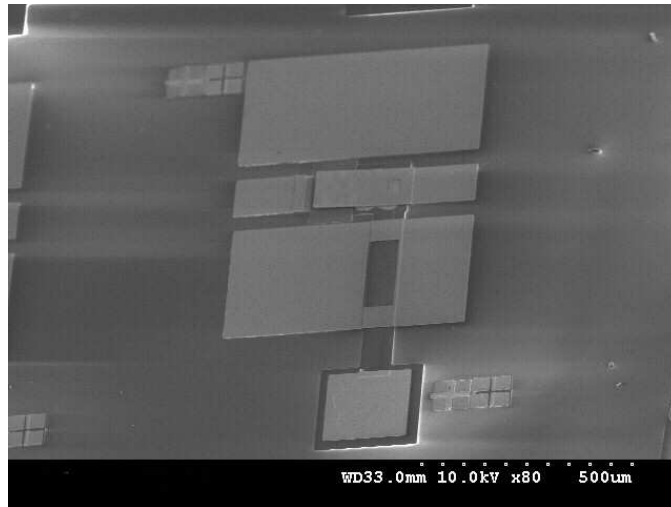


Figure 69: SEM of a fabricated Cantilever type CPW switch on sapphire with 200 nm BST layer and 1.2 μm thick Au membrane.

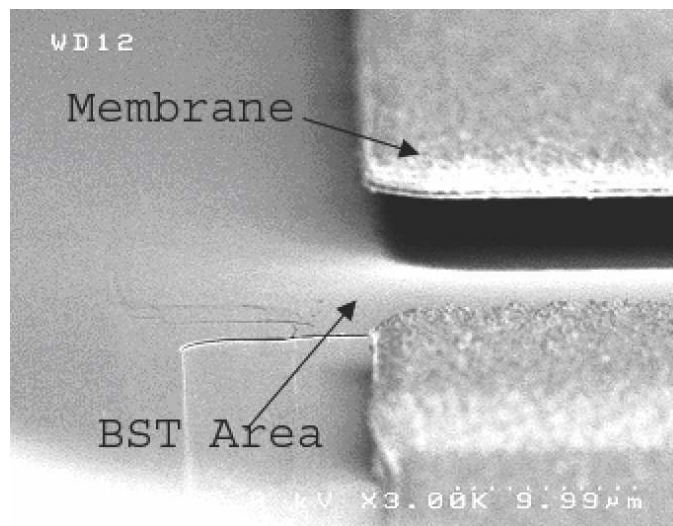


Figure 70: SEM Close-up view of membrane and BST area.

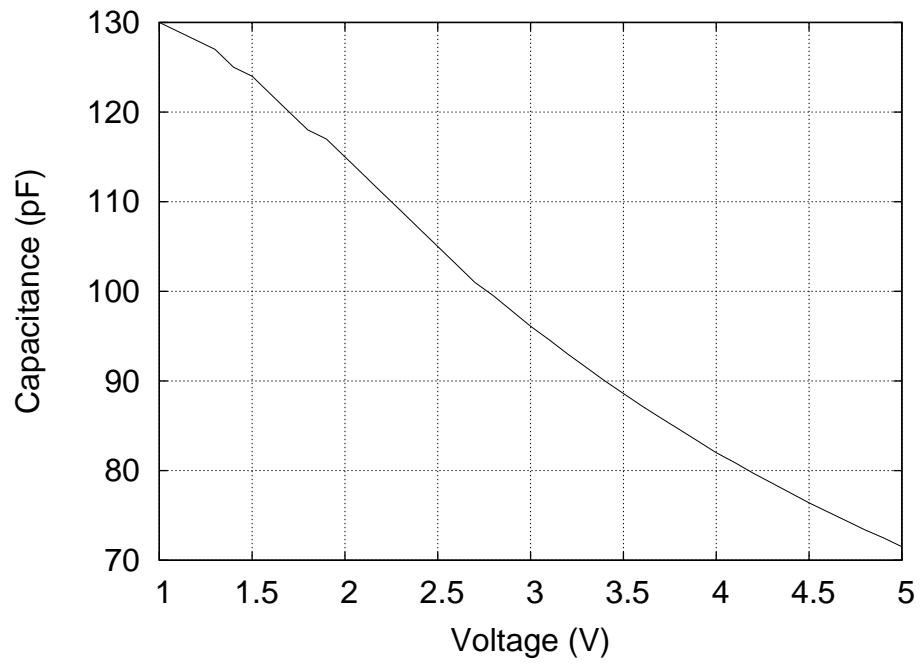


Figure 71: C-V Characteristic of the MEMS switch with BST dielectric layer at the down state.

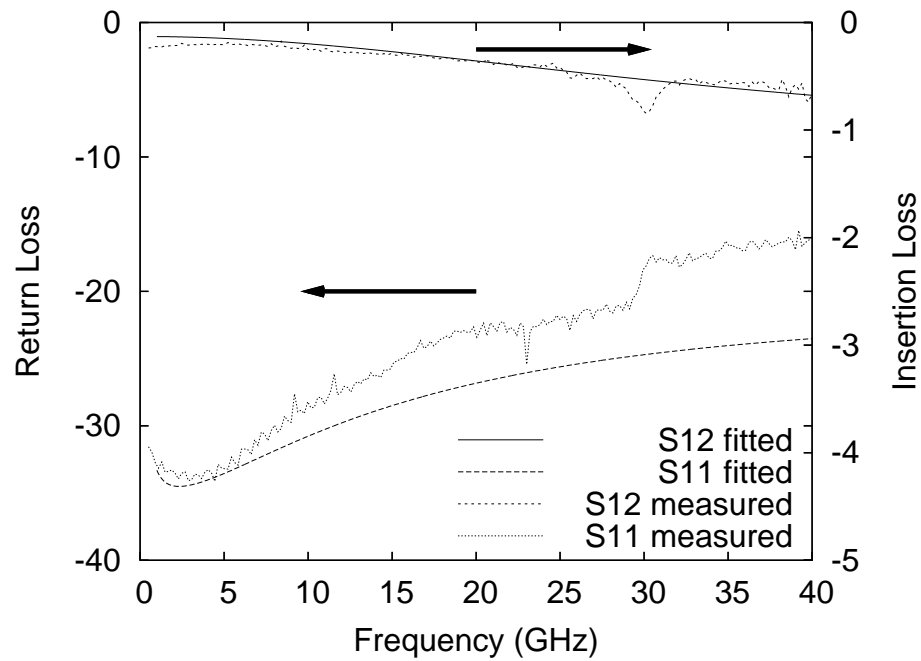


Figure 72: Measured S-parameters of the cantilever BST MEMS switch at down-state position.

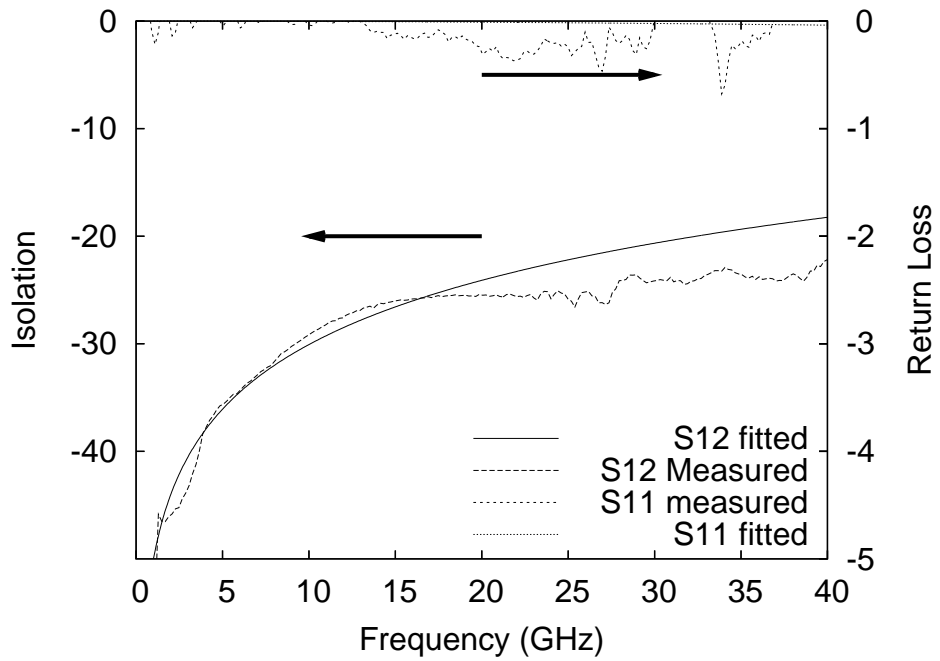


Figure 73: Measured S-parameters of the cantilever BST MEMS switch at up-state position.

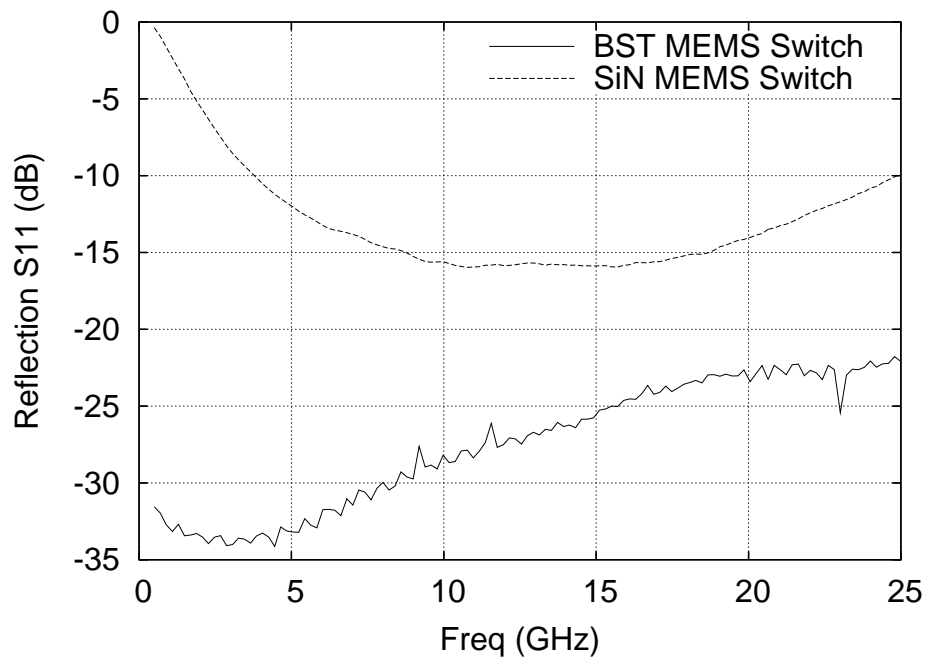


Figure 74: S-parameter comparison between BST and SiN switches at down-state.

5.3 Results

Figure 71 shows the C-V characteristic and the tunability of the BST MEMS series switches (cantilever type) at the down state using the Keithley 590 CV station. The capacitance changes from 130 pF to 71.2 pF when the applied voltage ranges from 1 to 5 volts. The tuning ratio is 1.82:1. The measured Q-factor is 260 at 20 GHz. A different capacitance range can be achieved with a different area. S-parameter measurements of the cantilever switch were taken using an Agilent 8510 network analyzer. A thru, reflect line (TRL) calibration with three delay lines at 10 GHz, 20 GHz and 30 GHz was performed to de-embed the coplanar line and transition losses. Measured results of the switch at both the "up" and the "down" state positions are shown in Figures 72-73. The pull-down voltage was measured to be 45 to 50 volts. The return loss in the up state is -0.3 dB at 20 GHz and -0.4 dB at 40 GHz, while the isolation is -25 dB at 20 GHz. An equivalent LCR circuit was used to fit the measured data. The fitted up state capacitance is 10 fF, while the series inductance and the series resistance of the switch are 5 pH and 0.5 Ω , respectively. The up state capacitance is smaller than that of theoretical calculation; this is due to the fact that the membrane is curled up as shown in the figure 6 which is caused by the residual stress inside the membrane. In the down state position, the insertion loss is -0.6 dB up to 40 GHz with a small resonance at around 30 GHz. The small resonance is due to the parasitic effects of the pull-down electrode and the DC bias line, which is not a highly-resistive material. To avoid this issue, a new geometry of the pull-down electrode and a DC bias line made of highly-resistive material (eg. Tin-doped Indium Oxide) should be used. A return loss more than 20 dB is achieved from DC up to 30 GHz. The fitted down-state capacitance and series inductance are 130 pF and 5 pH, the series resistance is 0.3 Ω . The optical profilometer result shows that the surface roughness of 200 nm thick BST thin film is less than 10 nm; this does not have any significant impact on the measured capacitance. The insertion loss is slightly higher when compared with other MEMS switches, because the signal lines of the switch are only 1000 Å thick. A much lower loss can be achieved by increasing the thickness of the Pt layer.

To further understand the BST MEMS switch performance, switches of the same physical structure and size with silicon nitride as the dielectric layer were fabricated and measured. Figure 74 shows the down state return loss of both BST and Si₃N₄ MEMS switches. From the comparison we can see that BST switches have higher return loss than that of the Si₃N₄ switches. This is because the BST switch capacitance is much higher due to the higher dielectric constant. In addition, the switch presented here has better isolation than that of [55].

5.4 Conclusions

In this work, MEMS capacitors with superior tunability with a new MEMS design have been developed, and MEMS switches with continuous(analog) tunability were investigated utilizing emerging BST thin film technology. For the developed switch, an excellent insertion loss of 0.6 dB was obtained in a frequency range from 0.5 GHz to 40 GHz, while the return loss is higher than 20 dB up to 30 GHz. Measured continuous tunability of the BST switches was also achieved for the first time. The results show that the down state capacitance of BST MEMS switch can change 182%, when the applied voltage ranges from 1 to 5 volts. The tunable RF MEMS switch can be used for the development of compact, low loss tunable digital capacitor banks for reconfigurable microwave circuits. The hybrid scheme of tunability (digital and analog) is expected to provide more design flexibility for compact reconfigurable RF front ends.

CHAPTER VI

TEMPERATURE STUDY OF THE DIELECTRIC POLARIZATION EFFECTS OF CAPACITIVE RF-MEMS SWITCHES

This chapter investigates both theoretically and experimentally the dielectric charging effects of capacitive RF MEMS switches with silicon nitride as the dielectric layer. Dielectric charging caused by charge injection under voltage stress was observed. The amphoteric nature of traps and its effect on the switch operation were confirmed under both positive and negative control voltages. It has been confirmed that charging is a complicated process, which can be better described through the stretched exponential relaxation. This mechanism is thermally activated with an activation energy being calculated from the temperature dependence of the capacitance transient response. The charging mechanism, which is responsible for the pull-out voltage and the device failure, is also responsible for the temperature induced shift of the capacitance minimum bias.

6.1 Introduction

Capacitive RF MEMS switches are one of the most promising applications in microelectromechanical systems (MEMS) [125], but their commercialization is currently hindered by reliability problems [22, 31, 51, 87, 101, 122, 129]. The most important problem is charging of the dielectric, causing erratic device behavior. The development of reliable switches requires a good analytical model that will describe the way charge accumulates in the dielectric and how it influences the device behavior. An analytical model explaining the influence of charging on the MEMS capacitive devices failure has been initially proposed by Wibbeler et al [122]. Improved models including charge distribution in the insulator volume and surface as well as taking into account large deflections and pull-in/pull-out phenomena, were

further proposed by M. Van Spengen et al. in [101] and X. Yuan et al. in [129].

In spite of these modeling efforts the knowledge on the dielectric charging mechanism is still limited. Here it must be pointed that it is well known that the deposited insulating films, typically Si_3N_4 , contain a large density of traps [51, 129] associated with dangling bonds [51]. These traps are of amphoteric nature, so they can be negatively or positively charged. Under high field conditions it is possible for charges to be injected and further being trapped in the dielectric film. Furthermore, due to the absence of convenient conducting paths in SiO_2 or Si_3N_4 the recovery time can be of the order of seconds to days.

Even though the exact mechanisms for the transfer and trapping of charge are not known, the effects are measurable [31, 101]. This is because when charge becomes trapped within the dielectric, it tends to screen [14, 72] the applied electric field that is used to control the actuation and release of the switch. As the charge builds up, the screening voltage detracts from the actuation voltage and until there is no longer enough force pulling on the membrane to cause it to actuate. The opposite occurs when the actuation voltage is removed; the trapped charges provide enough potential to stick down the membrane, hence leading to one of the most common failure mechanisms. Another issue is the effect of temperature on the switch pull-in voltage. Experimental studies [53] and simulations [131] have shown that a moderate temperature increase may cause the buckling of the switch structure, leading to premature failure. In spite of this no study has been performed on the temperature effect on the charging mechanism. Here it must be pointed out that the knowledge of the temperature effect is of critical importance since issues such as environmental temperature changes, temperature changes due to power dissipation that affect the switch reliability can be predicted .

The aim of the present work is to investigate the charging effect in RF MEMS capacitive switches with silicon nitride as dielectric layer in order to obtain a better insight on the dielectric charging mechanisms with an emphasis on the temperature effect. An initial investigation of the dielectric charging effects without any temperature considerations was presented in [71, 72]. The investigation presented herein includes the effect of temperature for the first time, thus, allowing the determination of thermally activated charging processes.

This is achieved by exploiting both the capacitance-voltage characteristic and the screening effect of the electric field, which is applied to control the switch actuation.

6.2 Theoretical Analysis

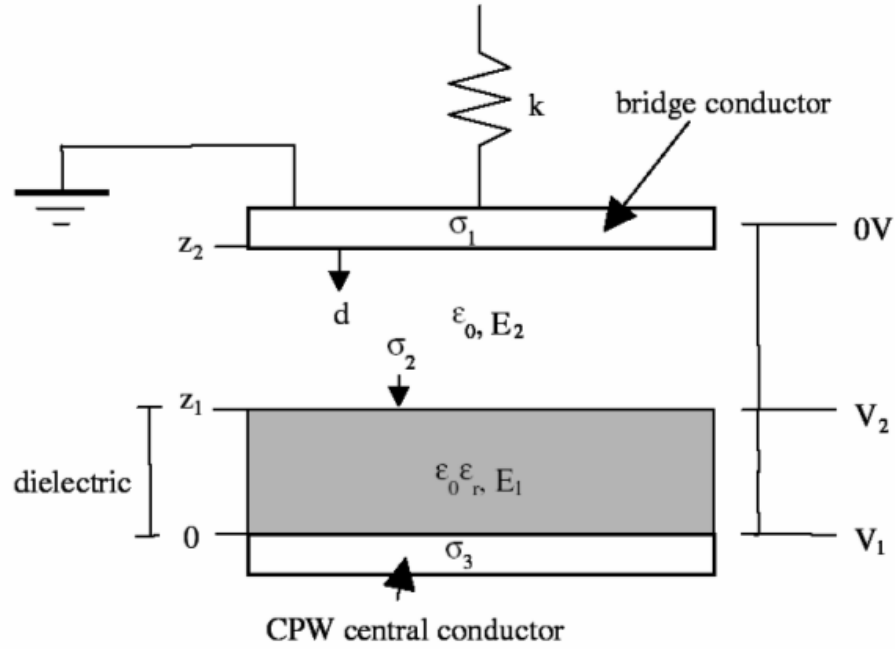


Figure 75: Simplified geometry of the switch structure and charging model [72].

A typical example of a capacitive RF MEMS switch based on the models proposed in [101,122], is shown in Figure 75. It consists of a freestanding plate suspended by a beam above a coplanar waveguide (CPW). Under this 'bridge', a high- ϵ_r dielectric is present. When a dc voltage is applied between the coplanar waveguide's (CPW) central conductor and the surrounding ground plane, the bridge is attracted electrostatically, and when the dc actuation voltage is high enough, it collapses and lands on top of the dielectric. Figure 75 shows the distribution of charges σ_1 to σ_3 , potential and electric fields in the insulator and the gap. The positions of sheets that are used are defined with z_1 and z_2 . The bridge of the switch has a spring force k , the bridge movement is indicated with the displacement d , the permittivity of free space is ϵ_0 and the dielectric has a relative permittivity ϵ_r . Although the parasitic charge can be modeled with sheets containing charges that can be at different

positions z , we have assumed for the sake of simplicity that σ_2 constitutes the interface charge at z_1 . For this reason, any bulk charge is assumed to be included in σ_2 , too. When the actuation voltage V_1 is applied, the 'bridge' is attracted by an electrostatic force [101]:

$$\frac{A\sigma_1^2}{2\epsilon_0} = -kd \quad (15)$$

The distance of the gap decreases by d and σ_1 will become a function of z_2-d [6].

$$\sigma_1 = -\frac{\epsilon_0 V_1 + \frac{z_1}{\epsilon_r} \sigma_2}{(z_2 - z_1 + \frac{z_1}{\epsilon_r}) - d} \quad (16)$$

Substituting $z_2 - z_1 + \frac{z_1}{\epsilon_r}$ with z , the switch capacitance will be given by

$$C = \frac{\epsilon_0 A}{z - d} \quad (17)$$

The device capacitance is minimized ($d=0$) under zero bias when there is no trapped charge or when the trapped charge electric field cancels the applied one. Around the capacitance minimum the bridge displacement is much smaller than the air gap ($z_2 - z_1$); that is the capacitance difference, with respect to its minimum value is [101]

$$\Delta C(V) \cong \frac{A^2}{2kz^2} \cdot (\epsilon_0 V + \frac{z_1}{\epsilon_r} \sigma_2)^2 \quad (18)$$

In this case the trapped charge, assuming to be accumulated at the dielectric surface, can be calculated from the offset of the capacitance-voltage characteristic minimum:

$$\sigma_2 = \frac{\epsilon_r \epsilon_0 \Delta V_{min}}{z_1} \quad (19)$$

When charge becomes trapped within the dielectric, σ_2 tends to screen the applied electric field that is used to control the actuation. This results in a decrease of σ_1 and so does the attracting force. Then the capacitance will relax to a lower value and if we restrict the investigation on small variations of the switch capacitance [72], we can be led to a rather simplified relation between C and σ_2 through differentiation of equation 17 and equation 15 and by substituting equation equation 16.

$$\Delta C = -B \cdot \Delta \sigma_2 \quad (20)$$

where

$$B = \frac{\sigma_1}{k\varepsilon_0^2} \cdot \frac{z_1}{z-d} \cdot C^2 \quad (21)$$

Therefore, for small values of ΔC , the transient behavior of the "ON" capacitance will represent the trapping/charging mechanism process.

In order to obtain a better insight on the transient behavior of the "ON" capacitance we must bring in mind that upon the application of an electric field the insulating layer of a MEMS capacitor is polarized. The polarization occurs by a number of mechanisms involving either microscopic and/or macroscopic charge displacements [112]. The electron and atomic polarization mechanisms are very fast processes. On the other hand, the dipolar, space charge and interfacial polarization mechanisms are processes that may require time that can last from milliseconds to years. Thus, when an electric field is applied the insulating film is almost instantly polarized through the first two mechanisms. The polarization is further increased, but with a slower rate, through the dipolar, space charge and interfacial polarization. Hence, the polarization build up, expressed by the surface charge density σ_2 , will consist of two components a very fast one and a much slower one that may be described by an exponential function, according to the elementary theory of dielectrics:

$$P(t) = P_S \cdot [1 - \exp(-\frac{t}{\tau})] \quad (22)$$

where P_S is the steady state polarization. Finally, it must be taken into account that the insulating materials used in RF-MEMS switches are amorphous and the polarization effects arising from the dipole orientation or the space charge polarization may not follow the ideal Debye model, thus the transient depolarization current may not follow the exponential decay relation of equation 22.

6.3 MEMS Switch Fabrication and Measurement

The MEMS switches used in this study were of air-bridge type and fabricated with a standard lithographic process on high resistivity silicon wafers ($\rho > 2000$ Ohm-cm). A 2500 Å thick layer of Si₃N₄ was deposited with the PECVD technique. The sacrificial layer was removed with resist stripper and the switches were dried using a critical point dryer. A

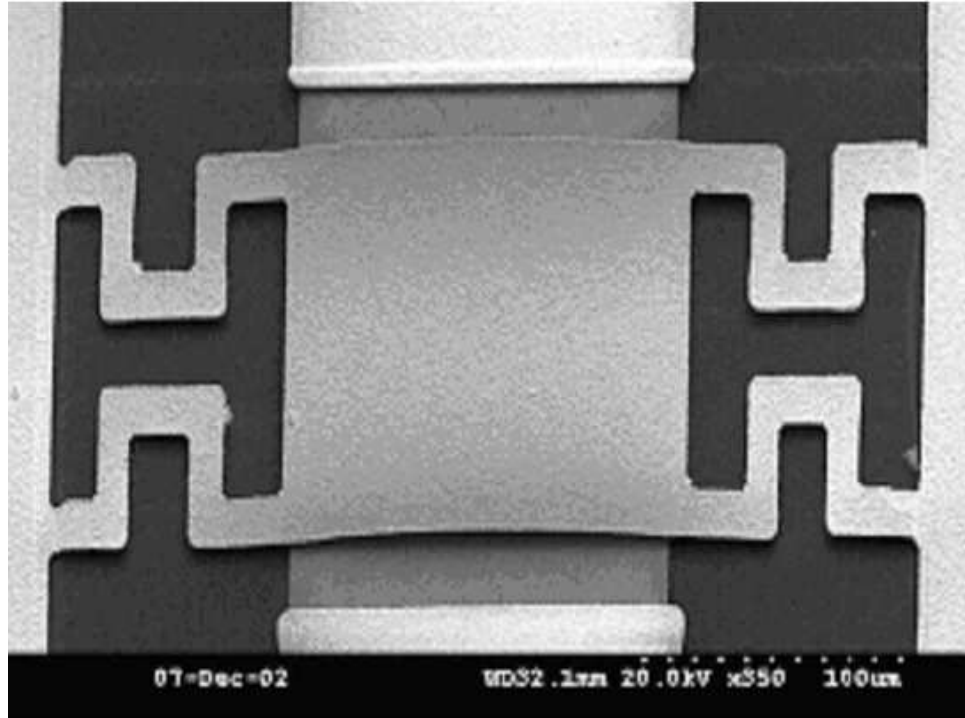


Figure 76: SEM photo of MEMS switch used in this chapter.

photo of the fabricated switch is shown in Figure 76.

The CV measurement of the switches were performed at the University of Athens, Greece. The capacitance of the RF MEMS switches was monitored with a Boonton 72B capacitance bridge. Capacitance-voltage measurements were performed by scanning the device bias in a closed loop of -20V to 20V with a step of 0.5V at 1MHz. More than twenty switches were tested and all exhibited the same performance, which is inherent to insulator and not the switch performance. No life tests were performed because the phenomenon under investigation was related to insulator behavior. In contrast after each transient the device was allowed to relax for at least two hours because repeated tests shifted the minimum value of capacitance (at V_{min}). The pull in voltage was estimated to be 20-35V. We applied a voltage step for transient experiments and the sweep for C-V was slow enough (0.1V/sec) in order to reach quasi-equilibrium. The minimum voltage offset was calculated by fitting equation 18 to the experimental data in the vicinity of the minimum. Furthermore, the transient response of the capacitance was recorded for a time duration of 200 secs and under positive or negative bias (20V) alternatively. The bias was applied after a relaxation

time of 40 secs under zero bias. All measurements were performed under vacuum and in the temperature range of 300K to 440K. In each case the capacitance was measured at a 1 sec time step.

6.4 Results and Discussion

6.4.1 Capacitance-Voltage Characteristics

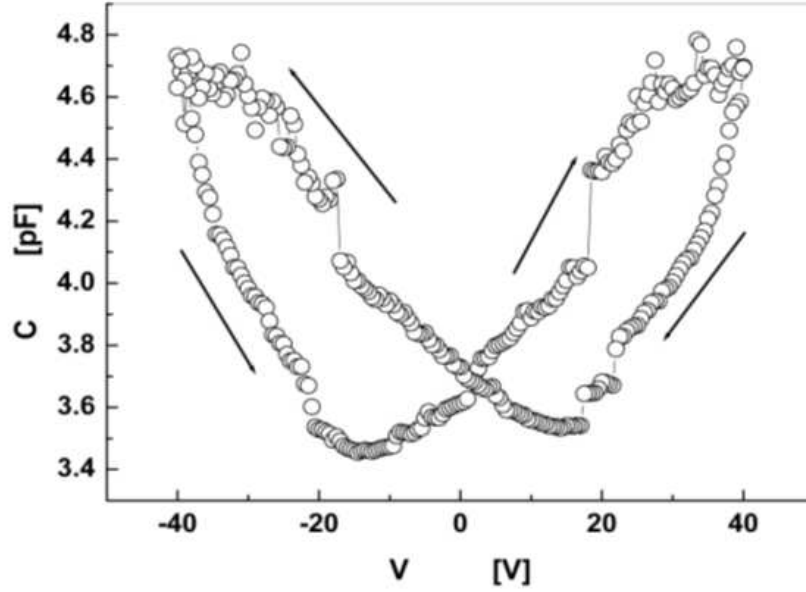


Figure 77: Typical C-V characteristic of a capacitive MEMS switch at room temperature. The probe-station parasitic capacitance was about 2.8 pF [71].

All MEMS capacitive switches exhibited the typical capacitance-voltage characteristic at room temperature (Figure 77), when the voltage was swept from -40V to 40V and back to -40V. A hysteresis in the C-V characteristic is introduced by charge trapping and subsequent dielectric charging, during both the positive and negative cycle. From the shift of the capacitance minimum bias (ΔV_{min}) (Figure 77), the dielectric surface induced charge was calculated and found to have a magnitude of about $2 \times 10^{12} \text{cm}^{-2}$. By decreasing the magnitude of the bias sweep to 20V the shift of the capacitance minimum was reduced indicating a decrease of trapped charge. In both cases, the shift is practically symmetrical indicating

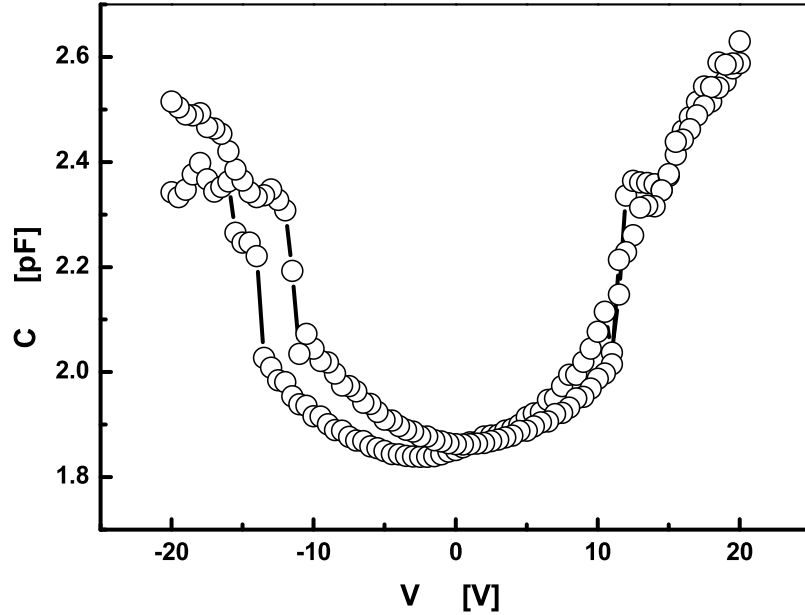


Figure 78: Typical C-V characteristic of a capacitive MEMS switch at 340 K [71].

that the residual polarization, due to fabrication processes and storage environmental effects is small enough. Furthermore, in each sweep, ascending or descending, the capacitance minimum lies on the same side with the starting bias polarity (Figure 77). Taking this into account we are led to the conclusion that the trapped charge has the same polarity with the capacitor bridge. Similar behavior was observed at higher temperatures (Figure 78 and Figure 79) when the actuation voltage was swept from -20V to 20 V and back to -20V.

Regarding the temperature of the capacitance minimum bias, this was calculated by fitting equation 18 to experimental data, as already mentioned above. In each case, ascending or descending, the magnitude of V_{min} was found to decrease with temperature (as shown in Figure 78 and Figure 79) and a polarity reversal was observed above 390K indicating that above this temperature the trapped charge σ_2 has an inverse polarity with the capacitor bridge (Figure 80). This behavior cannot be interpreted on the context of thermo-electrostatic-structural coupled simulations and the membrane buckling presented

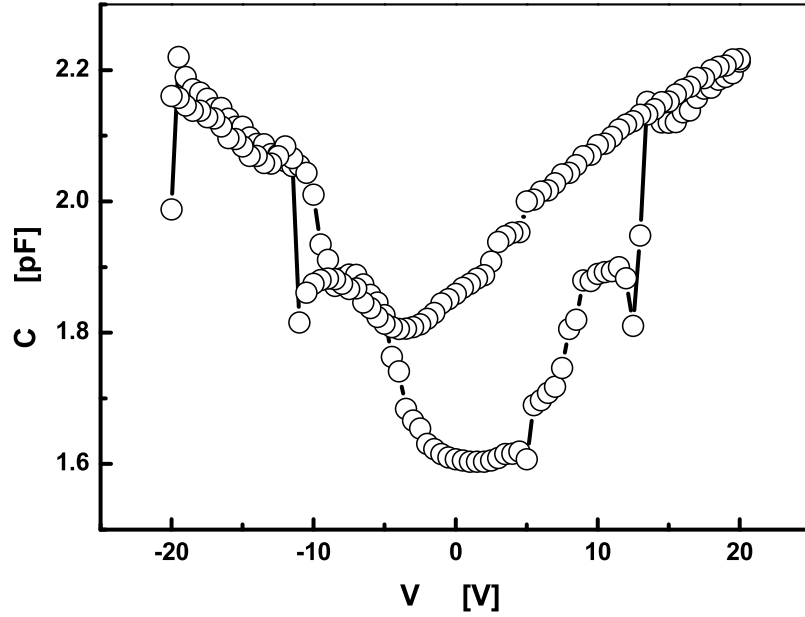


Figure 79: Typical C-V characteristic of a capacitive MEMS switch at 440 K [71].

in [131]. So, the polarity change of V_{min} must be attributed to a competition between several polarization mechanisms such as the free charge redistribution, charge injection and the decrease of dipole orientation friction. We must emphasize that all these mechanisms are temperature dependent [112]. Therefore we can interpret the data of Figure 80 in the following way [71]:

1). During actuation, charges are injected from the contacting bridge. The free charges and dipoles in the dielectric are redistributed and oriented, respectively. The resulting net surface charge (σ_2), according to ΔV_{min} , has the same polarity with the injected one, hence showing the dominance of the charge injection.

2). At higher temperatures, the charge redistribution is fast enough so that within the time scale of the experiment to cancel practically the injected one. Thus the contribution to the surface charge (σ_2) seems to come from the oriented dipoles leading to a polarity reversal of V_{min} .

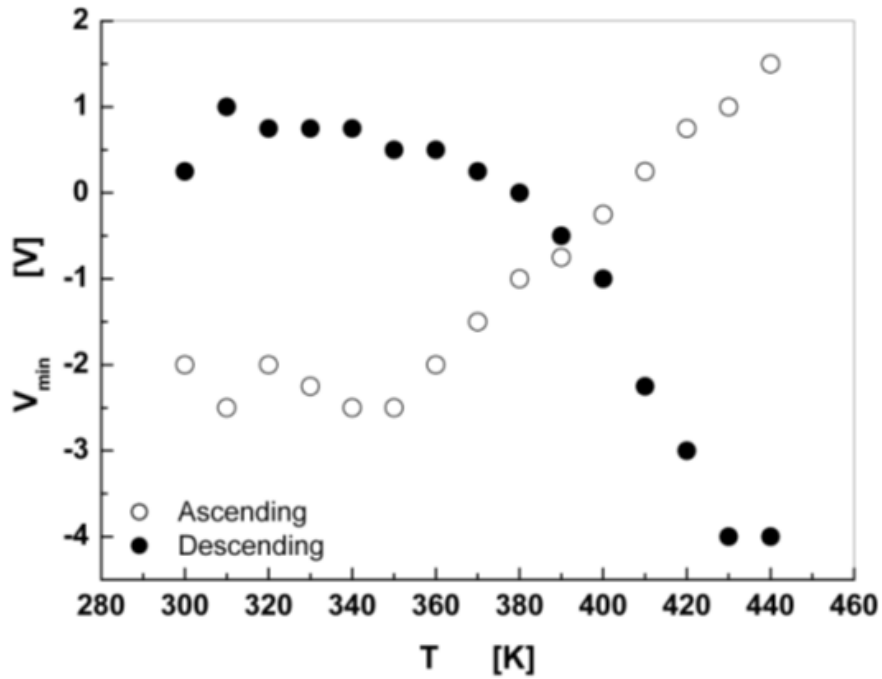


Figure 80: Temperature dependence of the offset voltage obtained by ascending and descending the C-V characteristic [71].

3). At the appropriate temperature, where the offset voltage crosses zero, the most probable reason is the compensation between the redistributed charge and the dipole orientation. This is the most reasonable explanation because the dipole orientation cannot be excluded. So, we are left with rather slow oriented dipoles and fast-redistributed charges. In fact it is a matter of experiment time scale. This is a first time presented result and needs to be further investigated with repeated runs, that is reliability-aging experiments. This probably cannot be exploited for most practical applications such as power devices which work at elevated temperatures.

This is important information that, although it needs further investigation, leads to useful conclusions that may be used for the prediction of (power) RF-MEMS switches performance at elevated temperatures.

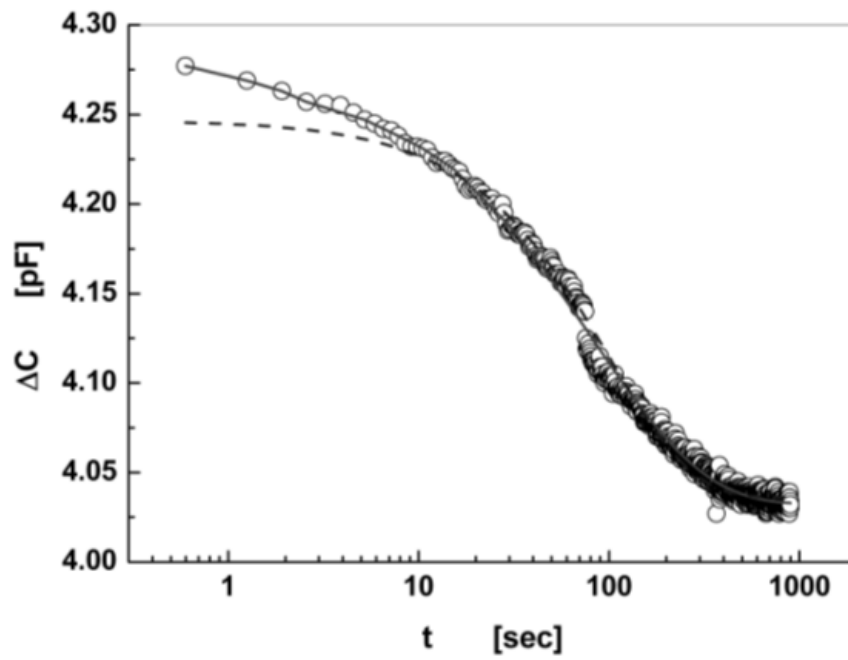


Figure 81: The transient response of a capacitive MEMS switch upon the application of a positive actuation voltage of 20V at room temperature [71].

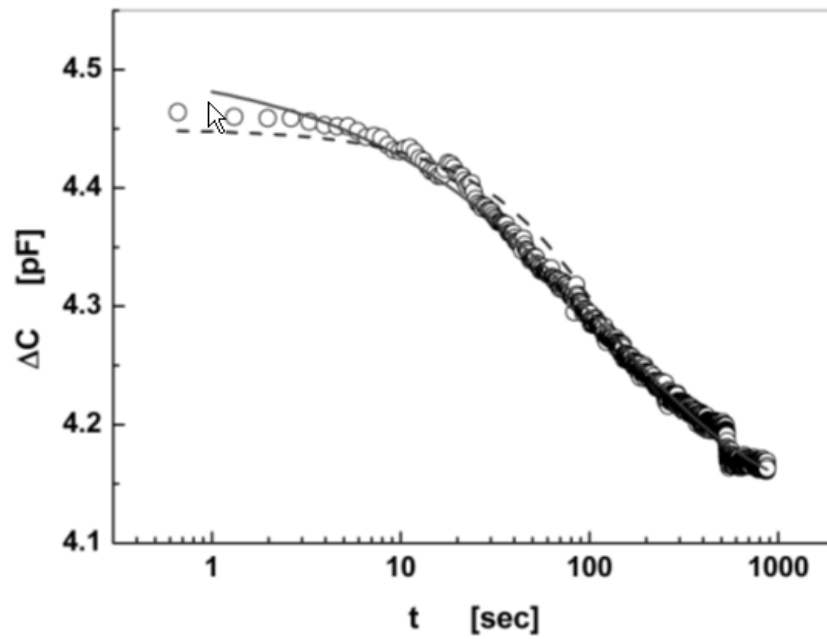


Figure 82: The transient response of a capacitive MEMS switch upon the application of a negative actuation voltage of 20V at room temperature [71].

6.4.2 Capacitance Transients

The temporal charging leads to transient response of the capacitive RF MEMS switch, when an actuation voltage of +20V is applied as shown in Figure 81. The decay resembles the exponential one but a fitting to the experimental data (dashed line) reveals a significant deviation in the short time range. In order to investigate the mechanism that may be responsible for such a transient behavior we must bring in mind the quality of the insulating film. As already mentioned, the dielectric film is rather a disordered material with a defect concentration of 10^{18}cm^{-3} [31,51]. A figure of the uncertainty of the composition lies also on the fact that the deposited silicon-nitride film is often labeled as SiN_x . It must be pointed also that the structure is asymmetrical since the insulating film is deposited on a metal substrate while the other surface is free. Furthermore the concentration of defects at the insulator-metal interface will be strongly affected by the growth conditions.

In such a system, a multi-exponential relaxation may be adopted, it is more appropriate to assume that the stretched exponential relaxation mechanism is the one that describes better the situation. The choice is based on the fact that the multi-exponential relaxation arises from a linear combination of independent contributions. This model, although simple, leaves us confronted with the lack of ability to determine both the actual number of processes and the weight of each contribution. Moreover, in disordered materials, the multi-exponential relaxation can hardly be applied because couplings among the atoms, clusters or degrees of freedom always exist. On the other hand, the stretched exponential relaxation constitutes a convenient tool, although the known models give no clear answer on the underlying properties of the medium responsible for the stretched behavior and the universality of the process. Furthermore, the fitting of stretched exponential relaxation is simple and the few fitting parameters can be used more effectively as indexes for the material improvement.

From the historical point of view, the stretched exponential relaxation was proposed by R. Kohlrausch (1847) for the description of viscoelasticity. Later it was found that it applies in a very wide range of phenomena and materials [67,69]. This type of relaxation is derived assuming a distribution of parallel rates arising from a random distribution of active

centers and microscopic distance-dependent interactions [69]. Regarding the dielectrics, the corresponding phenomenon is called Williams-Watts-Kohlrausch relaxation law [52] being described by theories of spin glasses. An example of the microscopic models that lead to the stretched exponential decay includes the estimation of survival probability of a random walking particle in the presence of a static distribution of random traps [84], the assumption of hierarchy in relaxation levels [69] and the dynamic scaling hypotheses applied for percolation clusters [36]. Microscopic models such as the estimation of survival probability of a random walking particle in the presence of a static distribution of random traps [84], the assumption of hierarchy in relaxation levels [69] and the dynamic scaling hypotheses applied for percolation clusters [36] can explain the stretched exponential decay. In a variety of materials the direct measurements of the discharge current [36] revealed a stretched exponential law for the time decay of the polarization:

$$P(t) = P_0 \exp[-(\frac{t}{\tau(T)})^\beta] \quad (23)$$

where P_0 is the initial polarization, β is the exponent and τ is the time scale of the process. The process time scale is thermally activated with activation energy E_A and a characteristic time τ_0 are obtained from the Arrhenius plot of

$$\tau(T) = \tau_0 \exp(\frac{E_A}{kT}) \quad (24)$$

In this chapter, the transient (ΔC) response is investigated, not the absolute values. All the equations are based on the assumption that the transient component is much smaller than the capacitance during actuation. The capacitance should follow the polarization trend (exponential decay) minus the steady state capacitance. In the present work, the adoption of this model leads to a capacitance that may vary with time as:

$$C(t) = C_\infty + \Delta C_0 \exp[-(\frac{t}{\tau(T)})^\beta] \quad (25)$$

where C_∞ is the steady state capacitance after the application of the actuation voltage and ΔC_0 is the transient amplitude. Since stretched exponential relaxation describes the macroscopic depolarization process, there is no need to refer to specific carriers and the

corresponding time constants. The fitting of equation 25 to the experimental data obtained after the application of an actuation voltage of +20V or -20V to the 'bridge', showed an excellent fitting (continuous line) presented in Figure 81 and Figure 82. Here it must be emphasized that the exponential decay (dashed line) failed in all cases in the short time range.

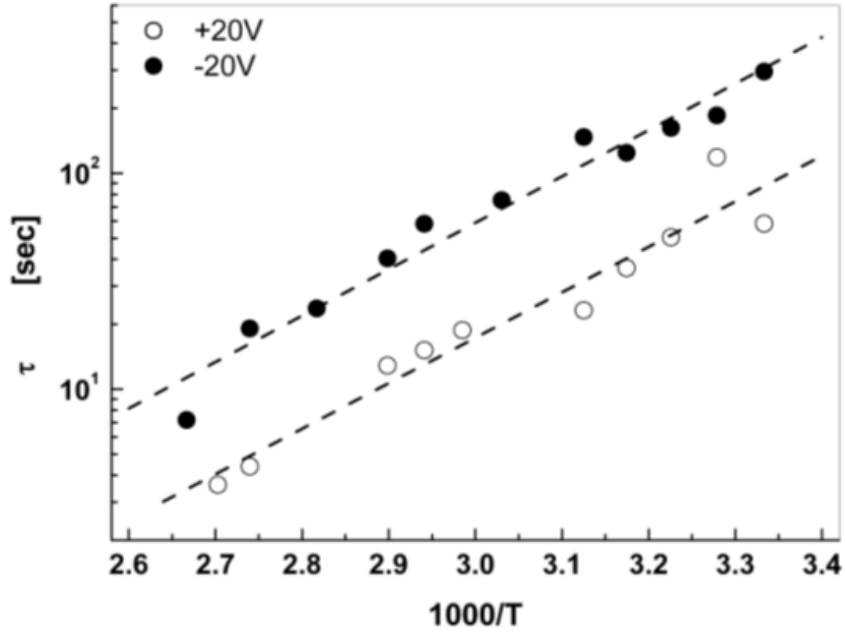


Figure 83: Arrhenius plot of the time scale of the stretched exponential decay process [71].

The capacitance transient response was recorded every 5K in the temperature range of 300K to 440K. The Arrhenius plots of the stretched exponential decay process time scale for positive and negative bridge bias are presented in Figure 83. In both cases the activation energy were found to be about 0.42eV revealing the same thermally activated mechanism. In contrast the characteristic time τ_0 was found depending on the polarity of the applied bias. Given that electrons are injected from metal electrodes, when the electrons are injected from the bottom electrode the characteristic time was found to have a value of 8.4×10^{-6} sec. For opposite polarity, that is when the electrons are injected from the contacting bridge, the characteristic time has a value of 2.1×10^{-5} sec. This disparity has to be attributed to the differences between the lower and the upper metal-insulator interfaces. In RF-MEMS

switches this argument is correct since the upper metal-insulator contact occurs during actuation, the contact area is practically not necessary uniform, and hence the injected current distribution is inhomogeneous. The fact that the activation energy was found to have the same value for both polarities leads to the conclusion that the polarization process arises from a distribution of relaxation times τ_0 [112] around an activation energy, which most probably is connected to the barrier for carrier exchange that is electron injection and trapping or emission. These results are presented experimentally for the first time, to the best of the authors' knowledge.

6.5 Conclusions

The C-V characteristics of electrostatically actuated RF MEMS capacitive switches were measured and analyzed under different temperatures [71]. Dielectric charging caused by charge injection under voltage stress was observed. The amphoteric nature of traps and its effect on the switch operation were confirmed under both positive and negative control voltages. The temperature dependence of the magnitude and the polarity reversal of the trapped charge were revealed from the temperature dependence of the capacitance-voltage characteristic for the first time. Furthermore, it has been confirmed that the charging is a complicated process, which can be better described through the stretched exponential relaxation. The temperature dependence of the transient response of the switch capacitance confirmed the amphoteric nature of traps. Finally, the activation energy of the thermally activated charging mechanism was found to have the same value for both bias step polarities. Since there are several microscopic models that lead to the stretched exponential decay and practically all are applicable to materials possessing a degree of disorder, a systematic investigation involving both experimental processes as well as material growth conditions will lead to a better understanding of the charging mechanism in the near future.

CHAPTER VII

MICROWAVE APPLICATIONS WITH RF MEMS SWITCHES

In this chapter, microwave applications of RF MEMS switches are discussed. Demonstration of two RF circuits are presented. The first is a reconfigurable antenna array with dual frequency and double polarization utilizing RF MEMS capacitive switches on multi-layer LCP layer; the second is a frequency and bandwidth tunable filter with ferroelectric capacitors and MEMS cantilever switches.

7.1 Introduction

Traditional solid-state switches such as p-i-n diodes and FETs introduce performance, or bias-power problems in the typical arrays used for radar and communications (thousands of antenna elements). P-i-n diodes have high insertion loss and consume a significant amount of DC power. Although much more integrable, FETs have higher insertion loss and poorer isolation because they are not very good resistive (on/off) switches. At microwave frequencies, the finite on-resistance typically leads to an insertion loss of 1 dB (i.e., 21%) and, because at least one switch is required for each bit in the time-delay phase shifter, at least half of the transmit power is lost to the switches alone, not accounting for transmission line and other losses. In addition, although solid state electronic devices such as GaAs MESFETs and p-i-n diodes have been used to implement SPDT switching networks that are required for switched line phase shifters in phased arrays or other reconfigurable antenna systems and enabled great leaps in radar and communication technologies, they have several problems. They rely on control of current through a semiconductor junction or a metal semiconductor junction, and there is a resistive loss associated with charge flow that consumes substantial DC and RF power. This consumed power generates heat that must be dissipated, which adds to the system size and complexity. Lastly, linearity is required for

modern, wide band communication systems that must process signals with a wide dynamic range, but transistors and diodes are nonlinear devices. RF-MEMS switches are promising because they can simultaneously provide superior RF performance at lower cost than p-i-n diodes, the circuit integrability of FET's, and bias power consumption much less than either. In general, MEMS have demonstrated substantially improved RF characteristics such as linearity, negligible power consumption, decreased insertion loss and improved isolation. Reconfigurable multi-band phased-array antennas are receiving a lot of attention lately due to the emergence of RF MEMS (micro-electro-mechanical systems) switches [11, 99]. A MEMS-switched reconfigurable multi-band antenna is one that can be dynamically reconfigured within a few microseconds to serve different applications at different polarizations or drastically different frequency bands, such as communications at L-band (1-2 GHz) and synthetic aperture radar (SAR) at X-band (8-12.5 GHz). The Air Force also uses both ground- and airborne- moving target identification (GMTI/AMTI) at these frequencies in order to detect moving targets such as vehicles on the ground and low observable in the air. The RF MEMS switch is attractive because it can achieve excellent switching characteristics [11] over an extremely wide frequency band (DC-40 GHz and upwards). These switches can also be used to develop wide band phase shifters. Although there is currently a tremendous amount of research in RF MEMS devices, reliability and packaging of the switches continue to be a challenge. The switches are also limited in their power handling capability.

7.2 Reconfigurable Dual Frequency Antenna with RF MEMS Switches

7.2.1 Introduction

Many radar and communication systems require antennas equipped with dual polarization capabilities that give a higher capacity of data transfer. In multiple input, multiple output (MIMO) mobile communications systems, dual polarized antennas serve as a means of increasing the number of subchannels [21], while in automotive radar systems, dual polarized antennas can be used to detect potential road hazards, such as black ice [65], that have a

cross section with one dimension being much thinner than the perpendicular direction by receiving signals aligned on both axis contrary to the single polarizations utilized in the past. Moreover, dual-frequency antennas have gained interest in wireless communication systems where different frequency applications, including wireless local area networks (WLANs-802.11a, b,g) and personal communication services (PCS) can be covered in a single design. Over the last thirty years, antenna arrays have been utilized in various applications due to their directive main beam and high gain characteristics for long range communication. Microstrip patch antennas are often desirable antenna elements due to their low cost, low profile, light weight, and ease of fabrication characteristics [28].

Reconfigurable RF MEMS antenna systems were first introduced in 1998 by E. R. Brown [11] and since then have been studied by several research groups. An emphasis has been given in reconfigurable aperture (recap) and microstrip antenna structures, in order to achieve multiple octave tunability [10,17,49,120]. Still, the integration of RF MEMS with the antenna has not been fully demonstrated. In addition, although there have been many reported examples of dual frequency, dual polarization microstrip antenna arrays on substrates, such as Duroid, these designs are not always favorable for a radio frequency (RF) system-on-a-package (SOP) low cost technology due to various undesirable substrate properties. Materials, like Duroid, are often used in conjunction with low dielectric constant foam to realize multilayer configurations. Due to certain constraints, such as physical stress, the dimensions of the structure can be altered. Therefore, as a result, the effective dielectric constant can vary greatly hence changing the performance of the antenna by causing unwanted frequency shifts. In addition, in order to integrate switches and phase shifters to the antenna array, thus taking full advantage of polarization diversity and beam scanning capabilities, there is a need for a laminated substrate that is suitable for packaging RF passive and active components and embedded functions. A promising alternative to mature expensive multilayer substrates with these properties, like LTCC, is liquid crystal polymer (LCP). This material has gained much consideration as a potential high performance microwave substrate and packaging material as discussed in Chapter IV. Its low dielectric constant ($\epsilon_r = 3.0$) and low loss performance ($\tan\delta = 0.002$ to 0.004 for frequency less than

35 GHz), is a key feature in minimizing dielectric and surface wave losses. Moreover, the near hermetic nature of the materials (water absorption less than 0.04%), the flexibility and the relatively low processing temperatures enable the design of conformal antenna arrays, the integration of RF MEMS devices, and the low deployment costs in space applications from rolling antennas on LCP. The low water absorption of LCP makes the material stable in a variety of environmental conditions, hence, preventing changes in the materials' dielectric constant and loss tangent. The multilayer circuitry can be easily realized due to the two types of LCP substrates that have different melting temperatures. The high melting temperature LCP (around 315 °C) is primarily used as the core substrate layer, while the low melting temperature LCP (around 290 °C) is used as a bonding layer. Therefore, vertical integration can be achieved similarly to LTCC. The thickness of readily available LCP substrate layers can vary between 1 and 4 mils and this variance can be proven a significant advantage in complex 3D structures that require more flexibility in designing the total substrate thickness which can better meet strict design requirements. It is true that structures in LTCC can be made more compact due to its high dielectric constant and designing compact dual-polarization arrays on LCP can be a real challenge. However, the low dielectric constant of LCP will result in wider bandwidths and increased efficiencies in comparison to LTCC materials due to the larger physical areas. Furthermore, the low cost of LCP (\$5/sq. ft. for 2 mil, single clad, low melt LCP), 2- 3 times less than LTCC, and multilayer lamination capability makes it appealing for high frequency designs where excellent performance is required for minimal cost.

In this section, fabrication and measurement of dual-frequency (14 GHz and 35 GHz), microstrip antenna arrays with dual-polarization capabilities on LCP multilayer substrates for an SOP RF front-end is presented. These designs can eventually be applied to the remote sensing of precipitation at 14 and 35 GHz. As a first step, each polarization is realized and characterized by the use of RF MEMS switches. Antenna arrays with switch controlled polarizations introduce the possibility of a low-power reconfigurable antenna array design. Measured results of scattering parameter data are showed.

7.2.2 Design and Fabrication

The generic multilayer architecture of the dual polarization, dual frequency microstrip antenna array at 14 and 35 GHz is shown in Figure 84. A detail antenna design is shown in [3] designed by Ramanan Bairavasubramanian at the Georgia Institute of Technology. The metal for the ground plane and the antenna elements was copper and had a thickness of $18 \mu\text{m}$. The total substrate thickness for the design is 18 mils, consisting of three LCP layers, the dimensions and the structure are shown in Figure 85.

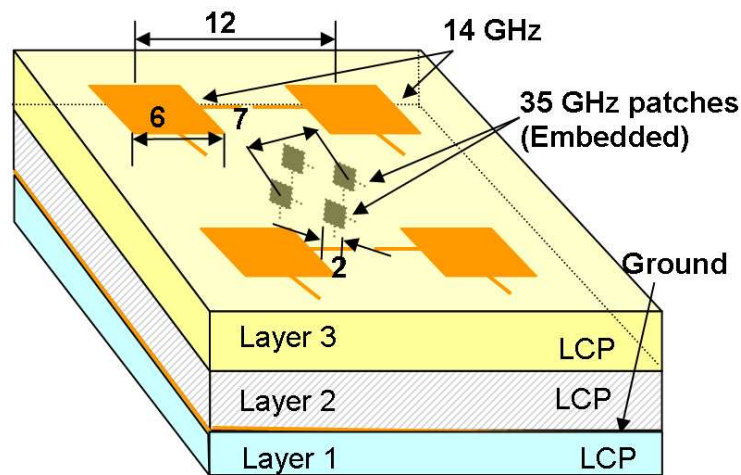


Figure 84: Multilayer antenna architecture [3].

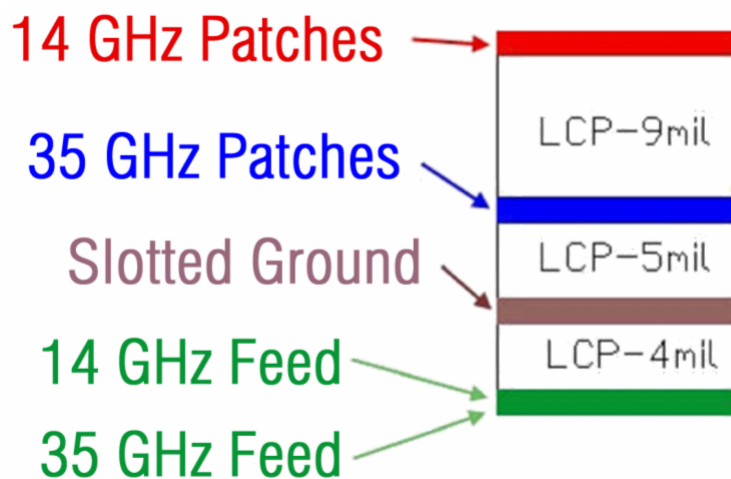


Figure 85: Dimension and side view of the antenna structure.

Figure 86 shows the schematics of the feeding network [3]. The antenna arrays were fabricated with double copper-clad LCP dielectric sheets from Rogers Corporation. The 14 GHz antenna array was fabricated on a 9-mil thick LCP substrate, while the 35 GHz antenna array was fabricated on a 5-mil thick LCP substrate, and a slotted ground was fabricated on the top side of a 4-mil LCP substrate. A standard photolithographic process was used for all the fabrication. Shipley 1827 photoresist was used for pattern definition. Both arrays were then exposed under 16,000 dpi mask transparencies pressed into sample contact with 5" glass mask plate. Photoresist development and a wet chemical etch with ferric chloride were then performed to complete the antenna patterning. Figure 87 shows the fabricated pattern on different layers. The three LCP layers were then bonded together followed the sequence as shown in Figure 85 with thermal compressive bonding technique using Karl Suss Bonder. Before the fabrication of the feeding network, the bottom side of the bonded LCP layers were polished to improve the surface smoothness. A Ti/Au layer was then evaporated and patterned on the polished side of the LCP layer to form the feeding network; the alignment was done through the laser etched alignment holes on the LCP. A 2000 Å silicon nitride was then deposited using plasma enhanced chemical vapor deposition at 150 °C to avoid the melting of the LCP layer. The nitride layer was then patterned and etched with RIE, a 3 μm thick photoresist was then spin coated and patterned to form the airgap for the MEMS switch. After that, Ti/Au/Ti seed layer was evaporated and electroplated to 3 μm thick. The final step is etching the seed layer and release the structure. During the whole fabrication, the other side of the sample was protected with a thick layer of photoresist. Figure 88 shows the pictures of the fabricated feeding network with MEMS switches and Figure 89 shows the close up view of the fabricated switch.

7.2.3 Measured Results

The arrays were mounted on an aluminum fixture that included a coaxial to microstrip connector to facilitate the S-parameter measurement. A short, open, load and thru (SOLT) calibration was performed with the reference planes at the end of the coaxial cables. The S-parameter measurement was done using the Agilent 8510 vector network analyzer. The

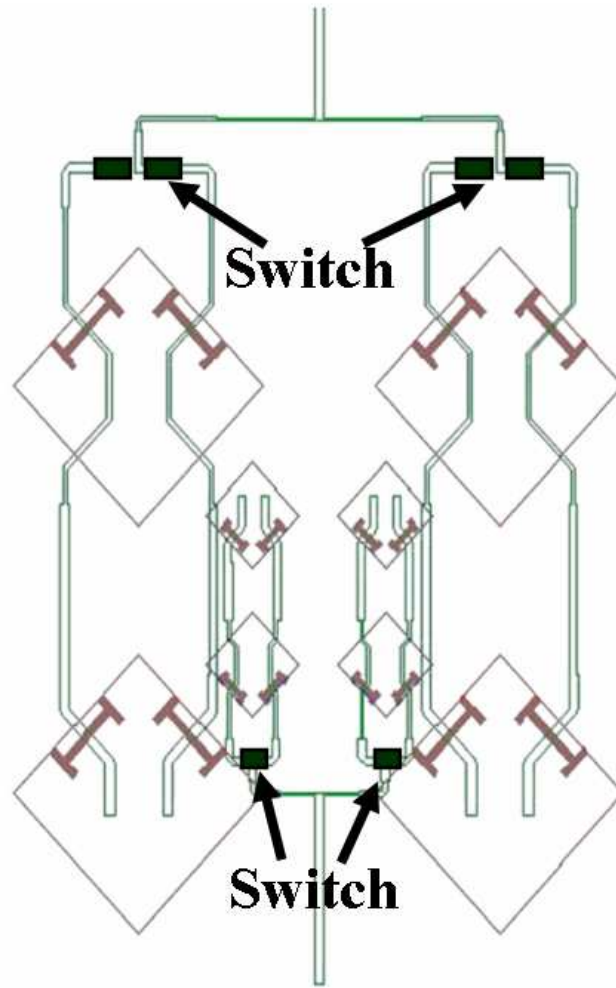


Figure 86: Schematics of the feeding network for both frequencies.

measured S-parameters are shown in Figures 90-91. Three states of the antenna array, all the switches up, polarization I and polarization II have been measured and are shown in the figures. For the 14 GHz antenna array, when all the switches are up, the return loss is about 1 dB at 14 GHz; For the polarization state I, the resonant frequency is around 14.7 GHz and the return loss is 31 dB; For the polarization state II, the measured resonant frequency is around 14.8 GHz and the return loss is 40 dB. For the 35 GHz antenna array, when all the switches are up, the return loss is about 1.2 dB at 35 GHz; For the polarization state I, the resonant frequency is around 36.4 GHz and the return loss is 22 dB; For the polarization state II, the measured resonant frequency is around 36.6 GHz and the return

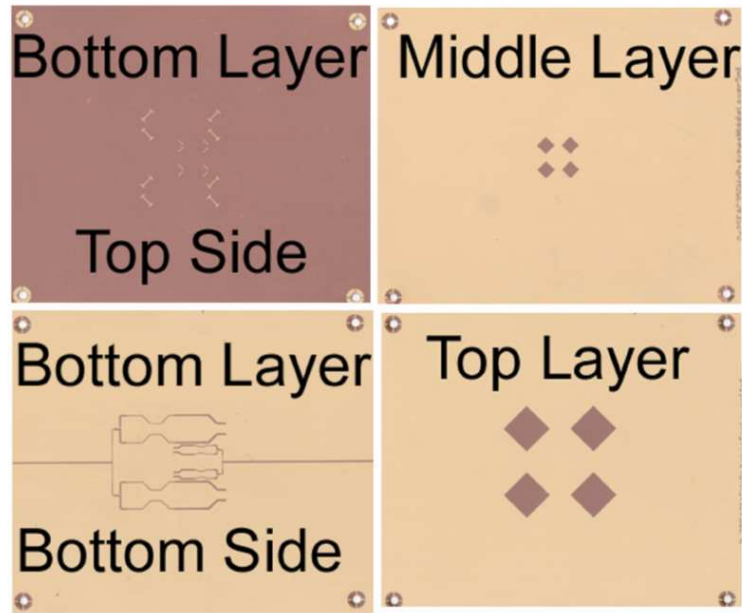


Figure 87: Pictures of the pattern on different layers before bonding.

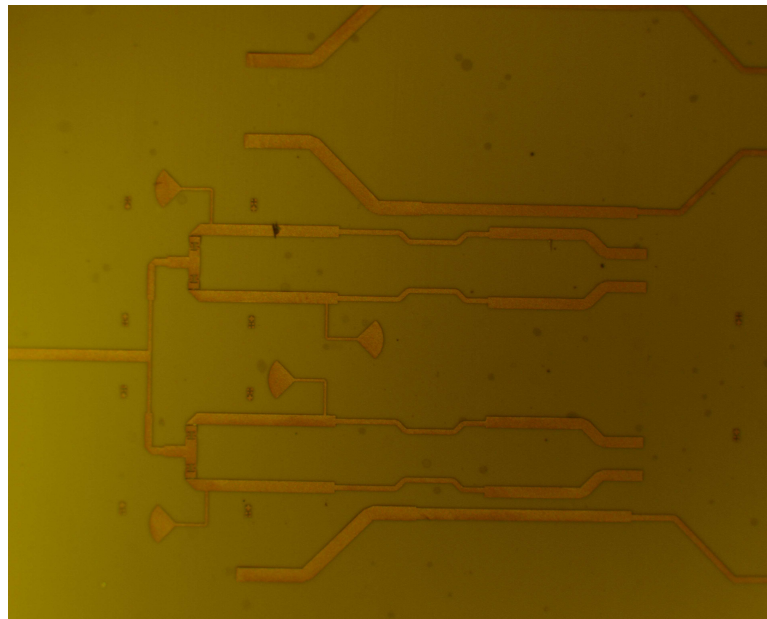


Figure 88: Photo of the fabricated feeding network with MEMS switches.

loss is 16 dB. For antenna arrays on both 14 and 35 GHz, there are frequency shift between the measurement and the desire value, this is because that the dielectric constant of the actual LCP substrate is a little smaller than that of the value used for the design simulation. This is also the reason that the frequency shift for 35 GHz antenna array is larger than that

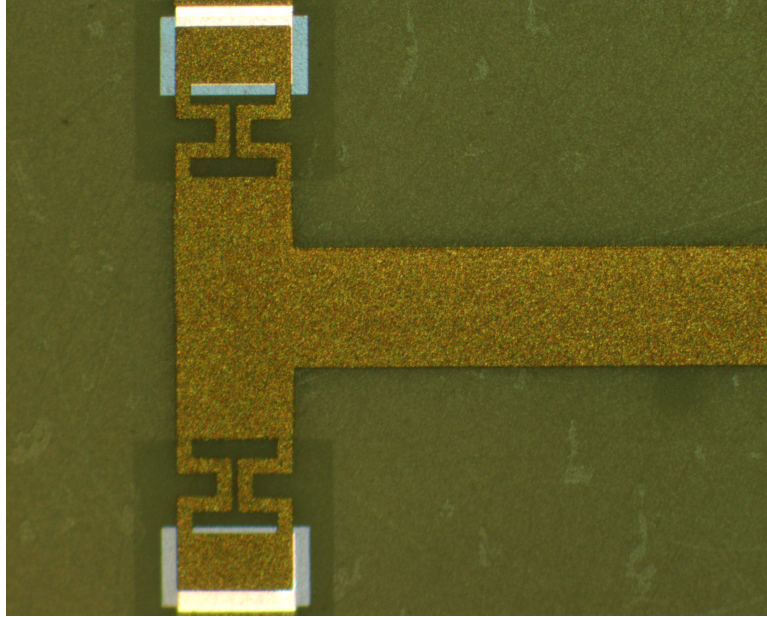


Figure 89: Photo of a fabricated SPDT MEMS switch.

of the 14 GHz antenna array.

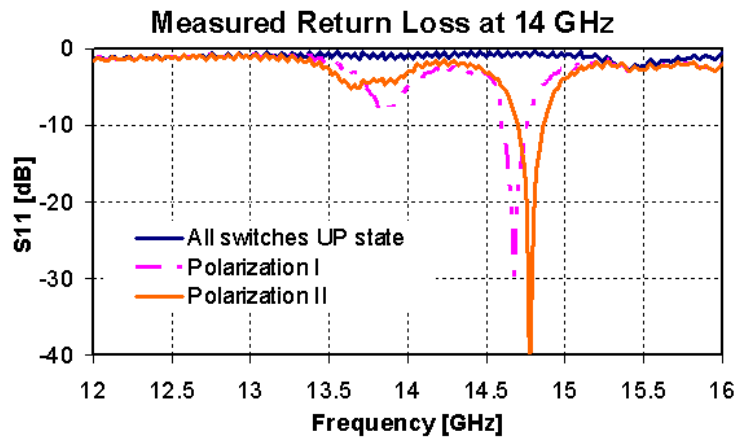


Figure 90: Measured S parameter for 14 GHz antenna array.

7.3 Frequency and Bandwidth Tunable Filter with RF MEMS Switch and Ferroelectric Capacitors

This section demonstrates a tunable bandpass filter with simultaneous frequency and bandwidth control using a combination of ferroelectric Barium Strontium Titanate (BST) capacitors and cantilever MEMS Switches. The center frequency of the filter is tuned in a

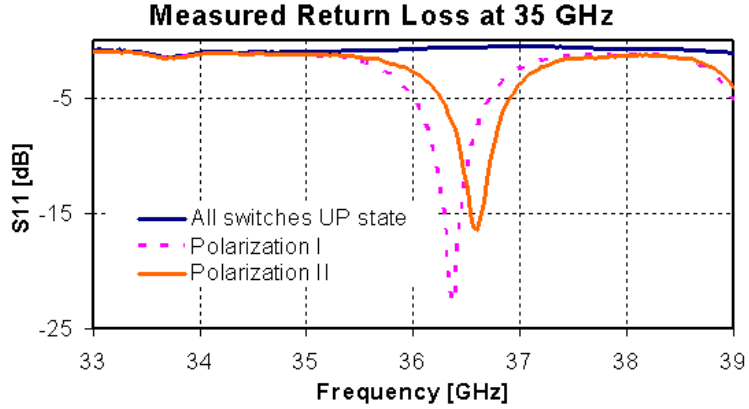


Figure 91: Measured S parameter for 35 GHz antenna array.

continuous fashion from 30 - 35 GHz with insertion loss ranging from 10 to 2.7 dB. Also the fractional bandwidth of the filter can be independently controlled by a tuning scheme that uses MEMS switches to vary the inter-resonator coupling. The 2 pole filter prototypes resulted in fractional bandwidths of 9.6 % (wideband configuration), and 4.8 % (narrow band configuration) for a tuning ratio of approximately 2:1. The third order filters resulted in bandwidths of 7.8 % (wideband configuration) and 3.1 % (narrow band configuration) for a passband tunable ratio of approximately 2.5:1.

7.3.1 Introduction

In recent years, evolving wireless communications have increased the demand for versatile technologies with adaptable frequency behavior. For this reason, components with multi-band coverage and multi-functional capabilities are becoming an important technological trend. This trend has led to the constant analysis of circuits with reconfigurable filtering functions [26, 43]. This is partially due to the fundamental roll of selective filters in RF front end electronics, and partially due to the vast variety of tunable filter applications. For example, a filter capable of selecting different frequency bands may replace a conventional filter bank reducing size and cost. Radar systems, may employ a bandwidth adjustable filter to eliminate out-of-band jamming spectral components. Communication systems with multi-band transceivers, may also adapt a filter capable of synchronizing to different information channels. In addition to the increasing need for filters with agile frequency behavior,

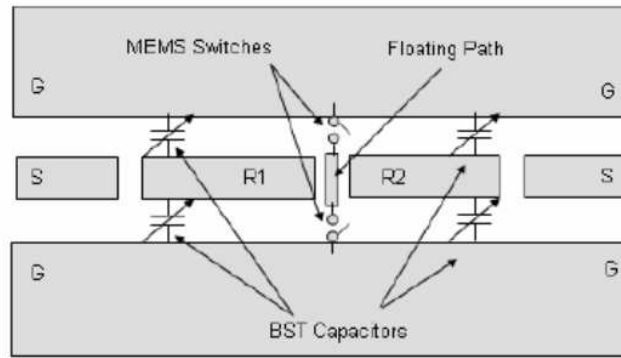
modern systems place stringent requirements in terms of low loss, low cost, small size, in-band phase delay flatness and dynamic range. Many research efforts are now focused in the development of tunable RF filters using variable reactance elements such as varactor diodes [9], p-i-n diodes [85] and MEMS switches [54]. Past efforts have also demonstrated reconfigurable filter topologies based on dual-mode resonators [56]. The present work reports for the first time a hybrid tunable filter topology that combines ferroelectric capacitors and MEMS switches. Ferroelectric materials such as the BST capacitors presented here show high controllable characteristics making them an attractive technology and a major factor in the future generation of tunable components. This section also demonstrates for the first time, a bandwidth tuning scheme that uses MEMS cantilevers to control inter-resonator coupling in a coplanar wave guide (CPW) configuration. The filters design is done by Cesar Lugo at the Georgia Institute of Technology. Detailed description on the filter design is shown in [57]

7.3.2 Design and Fabrication

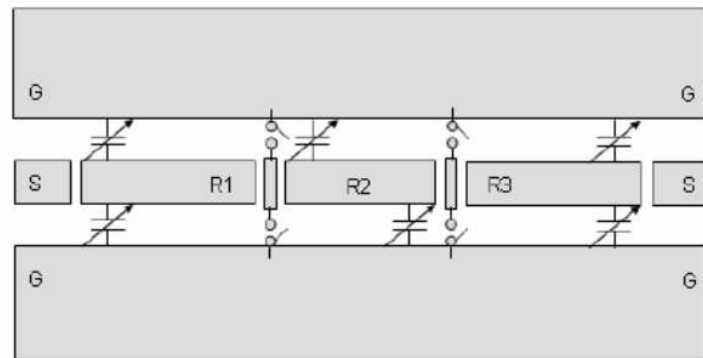
Schematics of the proposed second and third order filters are shown in Figure 92. The filters are designed using a CPW end coupled resonator topology, with a system impedance $Z_o = 50 \Omega$. Given the single plane for signal and ground, this topology avoids the need of via holes and greatly facilitates the introduction of tunable elements such as loading BST capacitors and MEMS switches. The resonator lengths are approximately $\lambda_g/2$ where λ_g is the guided wavelength at the design center frequency $f_0 = 40$ GHz. The goal is to produce a Chebychev bandpass filter with continuously tunable center frequency and adjustable fractional bandwidth.

Initially, when there is no BST capacitors, the center frequency of the designed filter is 40 GHz. Frequency control is achieved when the shunt variable BST capacitors are added at the resonator ends since they increase the electrical length of the resonators causing a frequency shift. When the capacitor is biased, the capacitance reduces and the center frequency will shift to higher frequencies.

The BST capacitors were designed using a planar configuration as shown in Figure 93.



(a)



(b)

Figure 92: Schematics of the 2 pole (a) and 3 pole (b) filter design.

The planar configuration requires fewer lithography steps and enables thicker metal to be deposited for lower metal losses. Most importantly, epitaxial BST thin film can be grown on single crystal substrates ensuring lower dielectric losses.

Important characteristics of a thin film BST capacitor include tunability, quality factor and dielectrics constant. Studies have shown that these electrical properties are strongly affected by crystalline structure, microstructure, dopants, composition, and the thickness of the BST films, as well as electrode material and thickness. The BST films is deposited by nGimat with its proprietary CCVD process as discussed in the previous chapter. The BST film is deposited on sapphire substrate that provides the building blocks for a host of microwave and RF broadband devices.

The spectral separation of the resonant poles in edge coupled resonator filters is directly related to the inter-resonator coupling strength. The coupling between adjacent resonators

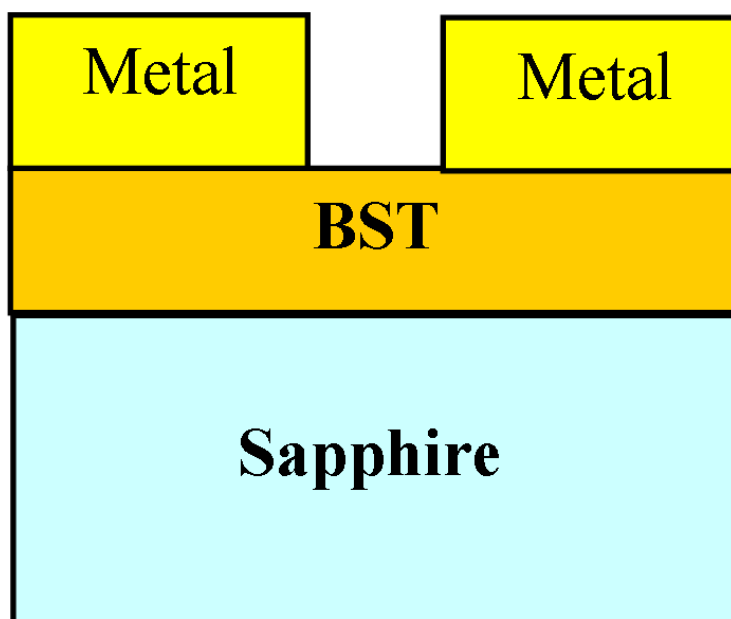


Figure 93: Cross section of a BST gap capacitor.

is due almost entirely to the fringing electric field produced at the resonator edges. A mechanism to control the inter-resonator coupling is achieved by a switchable structure that effectively change the amount of electric field energy coupled from one resonator to the next. This procedure is equivalent to a waveguide adjustable iris and it is demonstrated in a CPW configuration. The tuning structure consists of a conductive path placed between adjacent resonators. The conductive path is connected or isolated to the ground planes through a set of MEMS switch cantilevers. The cantilever switches were designed using the design rules discussed in Chapter III. A meander shape support was designed to get the actuation voltage around 25 Volts.

The 300 nm thick BST film was deposited first using the CCVD process, then the BST film was patterned using a diluted HF solution, following which high resistive bias lines were deposited and patterned by wet etching. Metallizations were then carried out using a lift-off process to form the capacitors, the CPW lines, and the activation pads for the MEMS switches. A Ti/Cu/Au metal stack was used with a total thickness of 2 μm for the former two structures and 0.8 μm for the latter. The filter was later passivated using BCB photosensitive polymers. The last step before MEMS fabrication was a metal layer forming

the bias pads and lines, which were on top of the BCB layer. The MEMS switch fabrication followed the same procedure as discussed in Chapter III. The detail fabrication process flow is shown in Figure 94. Figure 95 shows a picture of the fabricated 2 pole filter, Figure 96 shows a picture of the fabricated 3 pole filter, and Figure 97 shows the close up view of the fabricated switch for the filter.

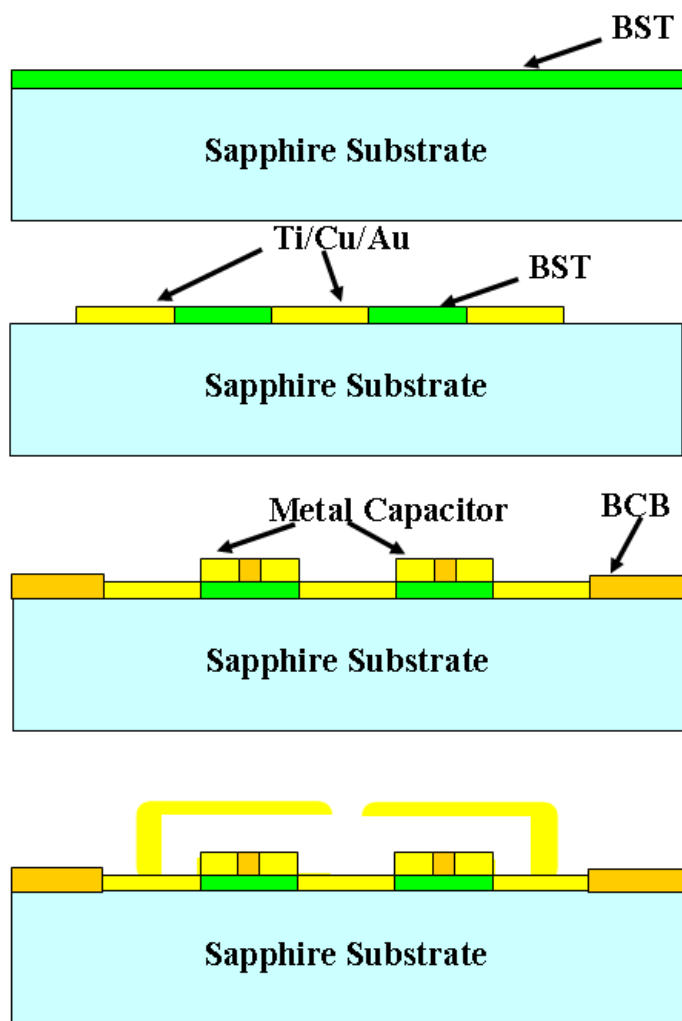


Figure 94: Fabrication process flow for the tunable filter with BST capacitors and MEMS switches.

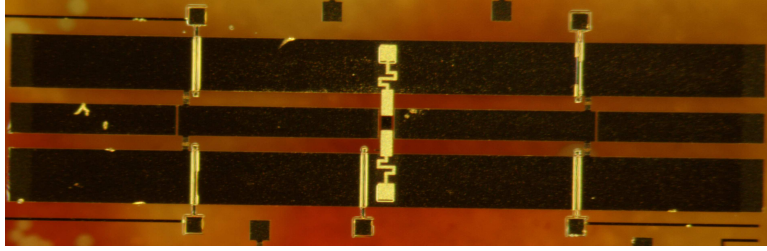


Figure 95: Picture of a fabricated 2 pole filter.

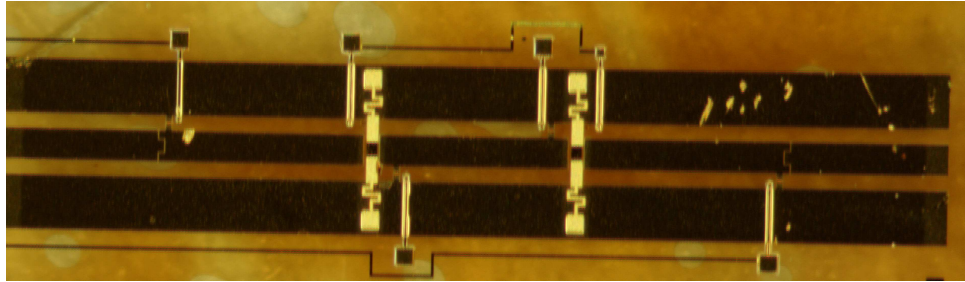


Figure 96: Picture of a fabricated 3 pole filter.

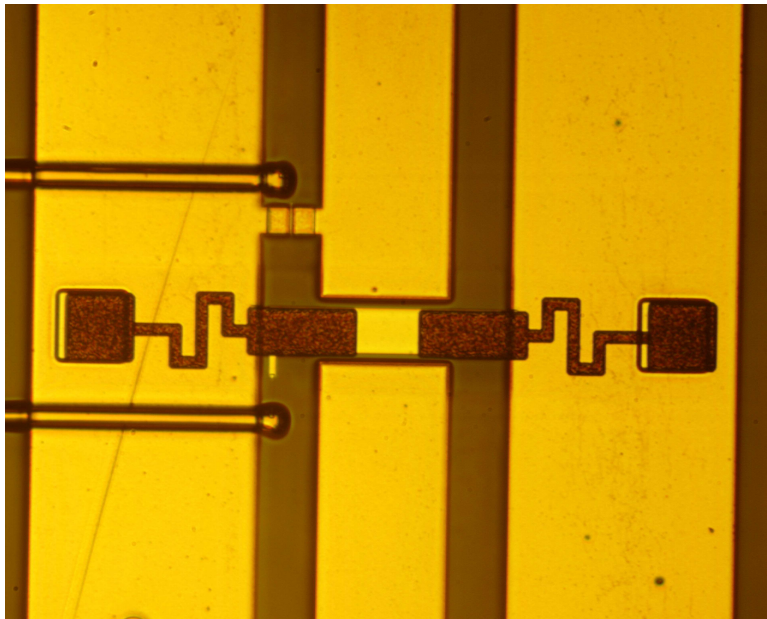


Figure 97: Fabrication process flow for the tunable filter with BST capacitors and MEMS switches.

7.3.3 Results and Discussion

The filters were measured using an Agilent HP 8510 vector network analyzer. An on-wafer short, open, load and thru (SOLT) standard calibration was done. The wide band (the cantilever switch is on the up state) and narrow band (the cantilever switch is on the down

state) 2 pole filter measured results are shown in Figures 98-99 respectively. The insertion loss of the wide band state ranges from 10 dB ($V_{bias}=0$ V) to 2.7 dB ($V_{bias}=40$ V). The narrow band state has a higher loss ranging from 17 dB ($V_{bias}=0$ V) to 5 dB ($V_{bias}=40$ V). The bandwidth change of the 2 pole filter is 9.6% for the wide band state and 4.8% for the narrow band state.

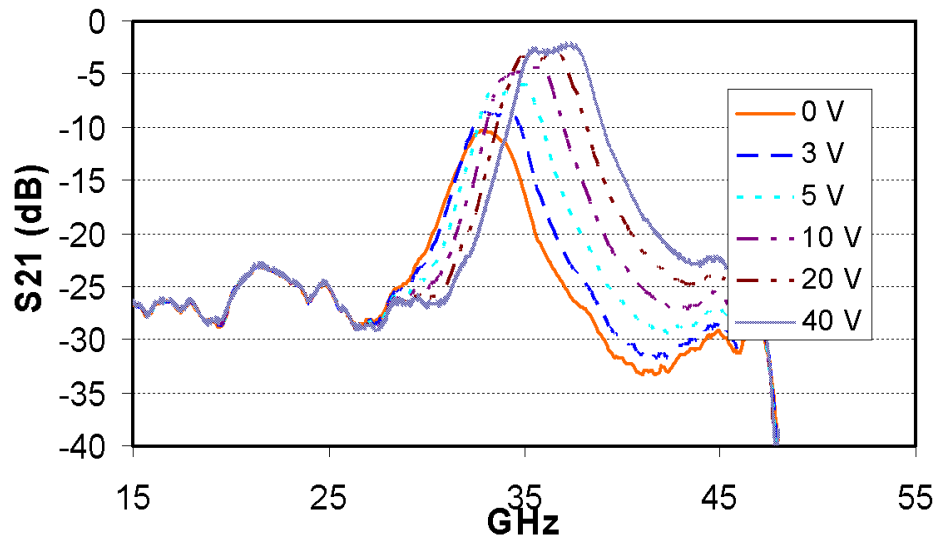


Figure 98: Measured results for the 2 pole filter (MEMS switch is on the Up position).

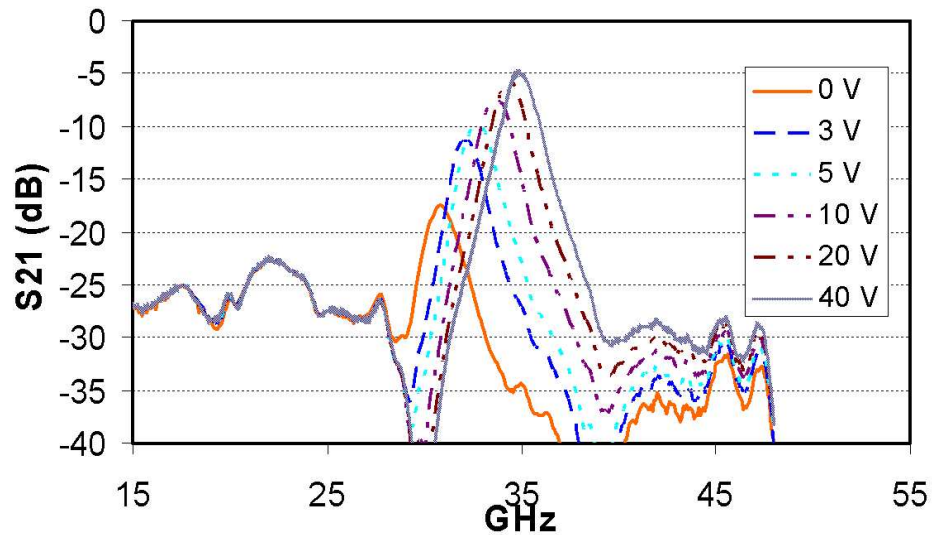


Figure 99: Measured results for the 2 pole filter (MEMS switch is on the Down position).

The wide band and narrow band 3 pole filter measured results are shown in Figures 100-101 respectively. The insertion loss of the wide band state ranges from 22 dB ($V_{bias}=0$ V) to 7.4 dB ($V_{bias}=40$ V). The narrow band state has a higher loss ranging from 25 dB ($V_{bias}=0$ V) to 8.6 dB ($V_{bias}=40$ V). The bandwidth change of the 2 pole filter is 7.8% for the wide band state and 3.1% for the narrow band state.

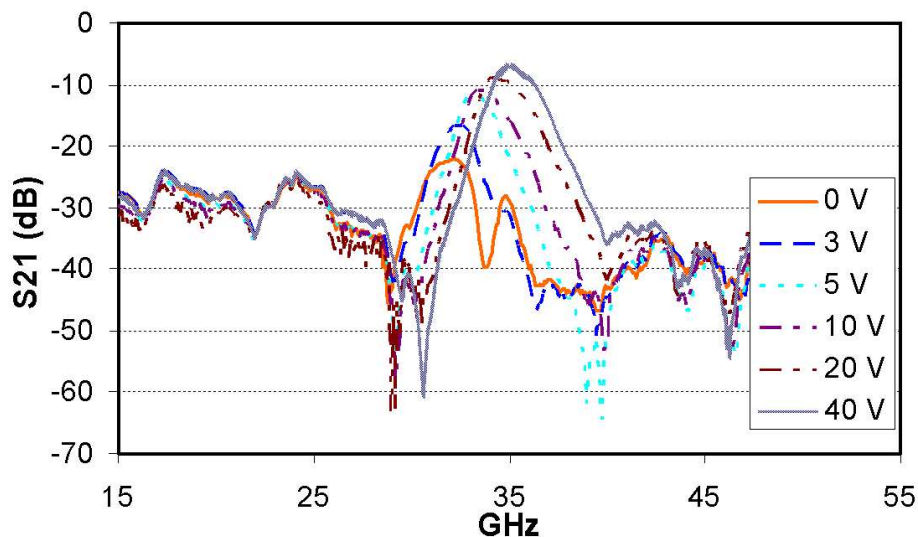


Figure 100: Measured results for the 3 pole filter (MEMS switch is on the Up position).

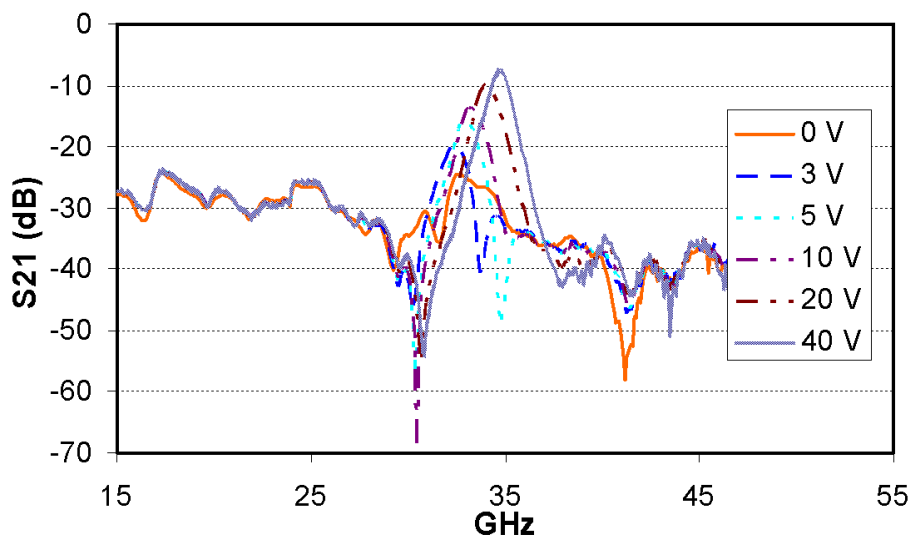


Figure 101: Measured results for the 3 pole filter (MEMS switch is on the Down position).

7.4 Conclusions

RF MEMS switches have superior advantages over traditional p-i-n diodes and GaAs FETs, they can be widely used to build revolutionary RF and microwave circuits which can utilize the benefits of RF MEMS switches. In this chapter, demonstration of two RF circuits with RF MEMS switches have been done. Development of a dual frequency with double polarization antenna array with MEMS switches is presented on a multilayer LCP substrate, the antenna arrays have been measured for both frequencies (14 and 35 GHz) and different polarizations, good return loss have been achieved. The developed antenna array can be integrated with remote sensing applications operating in the Ku and millimeter wave frequency bands. RF MEMS switches can be used to switch polarizations, hence, introducing the possibility of realization of low power reconfigurable antenna arrays. In addition, agile center frequency and bandwidth tunable filters using ferroelectric capacitors and cantilever MEMS switches are also demonstrated in this chapter. The measured center frequency can be tuned in a continuous fashion from 30-35 GHz with insertion loss ranging from 10 to 2.7 dB. Also the passband tuning ratio achieved is 2:1 for the 2 pole filter design and 2.5:1 for the 3 pole filter design.

REFERENCES

- [1] www.ngimat.com, May 2006.
- [2] ABBASPOUR-TARNIJANI, A., DUSSOPT, L., and REBEIZ, G. M., “A High Performance MEMS Miniature Tunable Bandpass Filter,” in *IEEE MTT-S International Microwave Symposium Digest*, vol. 3, pp. 1785–1788, 2003.
- [3] BAIRAVASUBRAMANIAN, R., HOMPSON, D., DEJEAN, G., PONCHAK, G., TENTZERIS, M., and PAPAPOLYMEROU, J., “Development of mm-wave dual-frequency multilayer antenna arrays on liquid crystal polymer (LCP) substrate,” in *Antennas and Propagation Society International Symposium*, vol. 1B, pp. 393–396, July 2005.
- [4] BARKER, N. S. and REBEIZ, G. M., “Distributed MEMS Truetime Delay Phase Shifters and Wide-bands Switches,” *IEEE Transaction on Microwave Theory Techniques*, vol. 46, pp. 1881–1890, Nov. 1998.
- [5] BARSTOW, S. J., JEYAKUMAR, A., and HENDERSON, C. L., “Direct Photopatterning of Metal Oxide Materials using Photosensitive Organometallic Precursor Films,” in *Proc. SPIE Emerging Lithographic Technologies*, vol. 1, pp. 421–430, 2002.
- [6] BARSTOW, S., *Use of photosensitive metal-organic precursors to deposit metal-oxides for thin-film capacitor applications*. PhD thesis, Georgia Institute of Technology, Atlanta, GA, 2003.
- [7] BELARAMAN, D., BHATTACHARYA, S., AYAZI, F., and PAPAPOLYMEROU, J., “Low Cost, Low Actuation Voltage Copper RF MEMS Switches,” in *IEEE International Microwave Symposium Digest*, pp. 1225–1228, 2002.
- [8] BLONDY, P., CHAMPEAUX, C., TRISTANT, P., CROS, D., and CATHERINOT, C., “Tunable Interdigital Filters using MEMS Capacitors,” in *European Microwave Conference Digest*, pp. 801–804, Sept. 2002.
- [9] BROWN, A. and REBEIZ, G., “A Varactor Tune RF Filter,” *IEEE Trans. on Microwave Theory Tech.*, vol. 48, pp. 1157–1160, 2000.
- [10] BROWN, E., “On the Gain of a Reconfigurable Aperture Antenna,” *IEEE Trans. on Antenna and Propagation*, vol. 10, pp. 1211–1223, 2001.
- [11] BROWN, E. R., “RF MEMS Switches for Reconfigurable Integrated Circuits,” *IEEE Trans. Microwave Theory Tech.*, vol. 46, pp. 1868–1880, Nov. 1998.
- [12] BROWNLEE, K., BHATTACHARYA, S., SHINOTANI, K., WONG, C. P., and TUMMALA, R., “Liquid Crystal Polymers (LCP) for High Performance SOP Applications,” in *8th Int. Adv. Packag. Materials Symp.*, pp. 249–253, Mar. 2002.
- [13] BUCHNER, R., BARTHEL, J., and STAUBER, J., “The Dielectric Relaxation of Water Between 0°C and 35°C,” *Chemical Physics Letters*, vol. 306, pp. 57–63, June 1999.

- [14] CHAN, E. K., GARIKIPATI, K., and DUTTON, R. W., "Characterization of Contact Electromechanics through Capacitance-Voltage Measurements and Simulations," *J. Microelectromechanical Systems*, vol. 8, pp. 208–217, 1998.
- [15] CHANG, C. H., QIAN, J. Y., CETINER, B. A., XU, Q., BACHMAN, M., DEFLAVIIS, F., and LI, G., "RF MEMS Capacitive Switches Fabricated with HDICP CVD SiN_x," in *IEEE MTT-S International Microwave Symposium Digest*, vol. 1, pp. 231–234, 2002.
- [16] CHEN, L., CRNIC, M., ZONGHE, L., and LIU, J., "Process Development and Adhesion Behavior of Electroless Copper on Liquid Crystal Polymer (LCP) for Electronic Packaging Application," *IEEE Transaction on Components Packaging and Manufacturing Technology*, vol. 25, pp. 273–278, Oct. 2002.
- [17] CHIAO, J. C., FU, Y., CHIO, J. M., DELISIO, M., and LIN, L. Y., "MEMS Reconfigurable Antenna," in *IEEE MTT-S International Microwave Symposium Digest*, vol. 2, pp. 1515–1518, June 1999.
- [18] COLLANDER, P., "Packaging technologies cellular phones," *Advanced Microelectronics*, vol. 26, pp. 6–13, 1999.
- [19] CULBERTSON, E. C., "A New Laminate Material for High Performance PCBs: Liquid Crystal Polymer Copper Clad Films," in *IEEE Electronic Components and Technology Conf.*, pp. 520–523, May 1995.
- [20] DEC, A. and SUYAMA, K., "RF Micromachined Varactors with Wide Tuning Range," in *IEEE MTT-S International Microwave Symposium Digest*, pp. 357–360, 1998.
- [21] DEGEN, C. and KEUSGEN, W., "Performance Evaluation of MIMO Systems using Dual-polarized Antennas," in *10th International Conference on Telecommunications, ICT2003*, Mar. 2003.
- [22] DENATALE, J., MIHAILOVICH, R., and WALDROP, J., "Techniques for Reliability Analysis of RF MEMS Switch," in *Proc. IEEE Int. Reliability Physics Symp.*, pp. 116–121, 2002.
- [23] FANG, W. and WICKERT, J. A., "Determining Mean and Gradient Residual Stresses in Thin Film using Micromachined Cantilevers," *Journal of Micromechanical and Microengineering*, vol. 6, pp. 301–309, Sept. 1996.
- [24] FARRELL, B. and LAWRENCE, M. S., "The Processing of Liquid Crystalline Polymer Rrinted Circuits," in *IEEE Electronic Components and Technology Conf.*, pp. 667–671, May 2002.
- [25] FENG, Z., ZHANG, W., SU, B., HARSH, K., GUPTA, K. C., BRIGHT, V., and LEE, Y. C., "Design and Modeling of RF MEMS Tunable Capacitors using Electro-thermal Actuators," in *IEEE MTT-S International Microwave Symposium Digest*, pp. 1507–1510, 1999.
- [26] FOURN, E., POTHIER, A., CHAMPEAUX, C., TRISTANT, P., CATHERINOT, A., BLONDY, P., TANNE, G., RIUS, E., PERSON, C., and HURET, F., "MEMS Switchable Interdigital Coplanar Filter," *IEEE Trans. on Microwave Theory Tech.*, vol. 51, pp. 320–324, 2003.

- [27] FUKUOKA, Y., SHIH, Y. C., and ITOH, T., “Analysis of Slow-wave Coplanar Waveguide for Monolithic Integrated Circuits,” *IEEE Transaction on Microwave Theory and Techniques*, vol. 31, no. 7, pp. 567–573, 1983.
- [28] GARG, B., *Microstrip Antenna Design Handbook*. New York, NY: Wiley, 2001.
- [29] GERE, J., *Mechanics of Materials, Fifth Edition*. Thompson-Engineering, 2003.
- [30] GOLDSMITH, C., “Lifetime Characterization of Capacitive RF MEMS Switches,” in *IEEE MTT-S International Microwave Symposium Digest*, pp. 227–230, 2001.
- [31] GOLDSMITH, C., EHMKE, J., MALCZEWSKI, A., PILLANS, B., ESHELMAN, S., YAO, Z., BRANK, J., and EBERLY, M., “Life time characterization of capacitive RF MEMS switches,” in *IEEE MTT S Int Microwave Symp Dig*, pp. 227–230, May 2001.
- [32] GOLDSMITH, C., LIN, T. H., POWERS, B., WU, W. R., and NORVELL, B., “Micro-machined Membrane Switches for Microwave Applications,” in *IEEE MTT-S International Microwave Symposium Digest*, pp. 91–94, May 1995.
- [33] GOLDSMITH, C., MALEZEWSKI, A., YAO, Z. J., CHEN, S., EHMKE, J., and HINZEL, D. H., “RF MEMS Variable Capacitors for Tunable Filters,” vol. 9, pp. 362–374, Nov. 1999.
- [34] GOLDSMITH, C., YAO, Z., ESHELMAN, S., and DENNISTON, D., “Performance of Low Loss RF MEMS Capacitive Switches,” *IEEE Microwave and Guided Wave Letters*, vol. 8, pp. 269–271, Aug. 1998.
- [35] HENDERSON, R. M., *Silicon Based Micromachined Packaging Techniques for High Frequency Applications*. PhD thesis, The University of Michigan, Ann Arbor, MI, 1999.
- [36] HENLEY, C. L., “Critical ising spin dynamics on percolation clusters,” *Physical Review Letters*, vol. 54, pp. 2030–2033, 1985.
- [37] HIGGINS III, L. M., “Hermetic and Optoelectronic Packaging Concepts using Multi-layer and Active Polymer Systems,” *Advancing Microelectronics*, vol. 30, pp. 6–13, July 2003.
- [38] HUNT, A. T., CARTER, W. B., and COCHRAN, J. K., “Combustion Chemical Vapor Deposition: A Novel Thin Film Deposition Techniques,” *Applied Physics Letter*, vol. 63, no. 2, pp. 266–273, 1993.
- [39] HUNT, A. T., COCHRAN, J. K., and CARTER, W. B., “Combustion Chemical Vapor Deposition of Films and Coatings,” in *U.S. Patent 5652021*, 1997.
- [40] HUNT, A. T., COCHRAN, J. K., and CARTER, W. B., “Method for the Combustion Chemical Vapor Deposition of Films and Coatings,” in *U.S. Patent 5863604*, 1999.
- [41] HUNT, A., COCHRAN, J. K., and CARTER, W. B., “Method for the Combustion Chemical Vapor Deposition of Films and Coatings,” in *U.S. Patent 6013318*, 2000.
- [42] HUNT, A., HWANG, T., and SHAO, H., “Combustion Chemical Vapor Deposition of Phosphate Films and Coatings,” in *U.S. Patent 5858465*, 1999.

- [43] HUNTER, I. and RHODES, J., “Electronically Tunable Microwave Bandpass Filters,” *IEEE Trans. on Microwave Theory Tech.*, vol. 30, pp. 1354–1360, 1982.
- [44] INOUE, H., FUKUTAKE, S., and OHATA, H., “Liquid Crystal Polymer Film Heat Resistance and High Dimensional Stability,” in *Proc. Pan Pacific Microelect. Symp.*, pp. 273–278, Feb. 2001.
- [45] JAYARAJ, K., NOLL, T. E., and SINGH, D. R., “A Low cost Multichip Packaging Technology for Monolithic Microwave Integrated Circuits,” *IEEE Journal of Advanced Packaging*, vol. 43, pp. 992–997, Sept. 1995.
- [46] JAYARAJ, K., NOLL, T. E., and SINGH, D. R., “RF Characterization of a Low Cost Multichip Packaging Technology for Monolithic Microwave and Millimeter Wave Integrated Circuits,” in *URSI Int. Signals, Systems, and Electronics Symp.*, pp. 443–446, Oct. 1995.
- [47] KHOO, C., BROX, B., NORRHEDE, R., and MAURER, F., “Effect of Copper Lamination on the Rheological and Copper Adhesion Properties of a Thermotropic Liquid Crystalline Polymer used in PCB Applications,” *IEEE Trans. Comp., Packag, Manufact., Technol.*, vol. 20, pp. 219–226, July 1997.
- [48] KINGSLEY, N., WANG, G., and PAPAPOLYMEROU, J., “Comparative Study of Analytical and Simulated Doubly-Supported RF MEMS Switches for Mechanical and Electrical Performance,” *The Applied Computation Electromagnetics Society Journal*, vol. 21, pp. 9–15, Mar. 2006.
- [49] KIRIAZI, J., GHALI, H., RAGAIE, H., and HADDARA, H., “Reconfigurable Dual-band Dipole Antenna on Silicon Using Series MEMS Switches,” in *Proceedings of Antennas and Propagation Society International Symposium*, pp. 403–406, June 2003.
- [50] KIVILAHTI, J., LIU, J., MORRIS, J. E., SUGA, T., and WONG, C. P., “Panel-size Component Integration (PCI) with Molded Liquid Crystal Polymer (LCP) substrates,” in *IEEE Electronic Components and Technology Conf.*, pp. 955–961, May 2002.
- [51] KRICK, D. T., LENAHAN, P. M., and KANICKI, J., “Electrically Active Point Defects in Amorphous Silicon Nitride: An Illumination and Charge Injection Study,” *J. Appl. Phys.*, vol. 64, no. 7, p. 3558, 1988.
- [52] KRIZA, G. and MIHALY, G., “Stretched-Exponential Dielectric Relaxation in a Charge-Density-Wave System,” *Physical Review Letters*, vol. 56, pp. 2529–2532, 1986.
- [53] LAFONTAN, X., TOUZE, C. L., WENK, B., KOLESNIK, I., PRESSECQ, F., and PEREZ, G., “Environmental Test Influence of the Temperature on RF Switches with Metallic Membranes,” in *Proc. SPIE*, pp. 624–628, June 2002.
- [54] LAKSHMINARAYANAN, B. and WELLER, T., “Tunable Bandpass Filter using Distributed MEMS Transmission Lines,” in *IEEE MTT-S, Int. Microwave Symp. Dig.*, pp. 1789–1792, June 2003.
- [55] LIU, Y., “High Isolation BST MEMS Switches,” in *IEEE MTT-S International Microwave Symposium Digest*, vol. 1, pp. 227–230, 2002.

- [56] LUGO, C., HADRICK, J., and PAPAPOLYMEROU, J., “Dual Mode Reconfigurable Filter for 3D System on Package (SOP) Integration,” in *IEEE Electronic Components and Technology Conf.*, pp. 532–535, June 2005.
- [57] LUGO, C., WANG, G., PAPAPOLYMEROU, J., ZHAO, Z., WANG, X., and HUNT, A., “Frequency and Bandwidth Agile mm-Wave Filter using Ferroelectric Capacitors and MEMS Cantilevers,” *IEEE transactions on Microwave Theory and Techniques*, vol. 58, pp. 3467–3473, 2006.
- [58] LUY, J. F., “Si/SiGe MMICs,” *IEEE Transaction on Microwave Theory Techniques*, vol. 43, no. 4, pp. 705–714, 1995.
- [59] MADOU, M., *Fundamental of Microfabrication*. New York: CRC Press, 1997.
- [60] MALUF, N., *An Introduction to Microelectromechanical Systems Engineering*. Boston, MA: Artech House Publishers, 2000.
- [61] MANNION, P., “Cellular/PCS Systems Take the Globe by Storm,” *Electronic Digest*, vol. 9, pp. 8–63, 1999.
- [62] MARGOMENOS, A., VALAS, S., HERMAN, M. I., and KATEHI, L. P., “Isolation in Three Dimensional Integrated Circuits,” in *IEEE MTT-S International Microwave Symposium Digest*, pp. 1875–1878, June 2000.
- [63] MCGRUER, N., ZAVRACKY, P., MORRISON, R., MAJUMDER, S., POTTER, D., and SCHIRMER, M., “RF and Current Handling Performance of Electro-statically Actuated Microswitches,” in *The Sensor Expo*, 1999.
- [64] MULDAVIN, J. and REBEIZ, G., “High Isolation MEMS Shunt Switches; Part 2: Design,” *IEEE Trans. Microwave Theory Tech.*, vol. 48, pp. 1053–1056, June 2000.
- [65] MURA, S. and GEARHART, S., “Dual-polarized Slotcoupled Patch Antennas on Duroid with Teflon Lenses for 76.5-GHz Automotive Radar Systems,” *IEEE transactions on Antennas and Propagation*, vol. 47, pp. 1836–1842, 1999.
- [66] MURPHY, C. Rogers Corporation, private communication. Jan. 2004.
- [67] NGAI, K. L., “Universality of low-frequency fluctuation, dissipation and relaxation properties of condensed matter. I,” *Solid State Physics*, vol. 9, no. 4, pp. 127–140, 1979.
- [68] PACHECO, S., PEROULIS, D., and KATEHI, L. P. B., “MEMS Single-Pole Double-Throw (SPDT) X and K-band Switching Circuit,” in *IEEE MTT-S International Microwave Symposium Digest*, June 2001.
- [69] PALMER, R. G., STEIN, D. L., ABRAHAMS, E., and ANDERSON, P. W., “Models of Hierarchically Constrained Dynamics for Glassy Relaxation,” *Physical Review Letters*, vol. 53, pp. 958–961, 1984.
- [70] PANCHEO, S. P., KATEHI, L. P. B., and NGUYEN, T. C., “Design of Low Actuation Voltage RF MEMS Switch,” in *IEEE MTT International Microwave Symposium Digest*, pp. 165–168, 2000.

- [71] PAPAIOANNOU, G., EXARCHOS, M., THEONAS, V., WANG, G., and PAPAPOLYMEROU, J., "Temperature study of the dielectric polarization effects of capacitive RF MEMS switches," *IEEE transactions on Microwave Theory and Techniques*, vol. 53, pp. 3467–3473, 2005.
- [72] PAPAIOANNOU, G. J., EXARCHOS, M., THEONAS, V., WANG, G., and PAPAPOLYMEROU, J., "On the Dielectric Polarization Effects Capacitive RF-MEMS switches," in *IEEE MTT-S International Microwave Symposium Digest*, pp. 761–764, June 2005.
- [73] PAPAPOLYMEROU, J., LANGE, K. L., GOLDSMITH, C. L., MALCZEWSKI, A., and KLEBER, J., "Reconfigurable Double Stub Tuners using MEMS Switches for Intelligent RF Front-ends," *IEEE Transaction on Microwave Theory Techniques*, vol. 51, pp. 1878–1885, Jan. 2003.
- [74] PIETERS, P., VAESEN, K., CARCHON, G., BREBELS, S., RAEDT, W. D., BEYNE, E., and MERTENS, R., "High Q Spiral Inductor for High Performance Integrated RF Front Ends Subsystems," in *IMAPS*, Sept. 2000.
- [75] PONCHAK, G. E., "RF Transmission Lines on Silicon Substrates," in *29th European Microwave Conference Digest*, pp. 158–161, Oct. 1999.
- [76] PONCHAK, G. E. and DOWNEY, A. N., "Characerization of Thin Film Microstrip Lines on Polyimide," *IEEE Transaction on Components, Packaging and Manufacturing Tech. Part B*, vol. 21, no. 2, pp. 171–176, 1998.
- [77] PONCHAK, G. E. and KATEHI, L. P. B., "Measured Attenuation of Coplanar Waveguide on CMOS Grade Silicon Substrates wiht a Polymide Interface Layer," *IEEE Electronics Leters*, vol. 34, no. 13, pp. 1327–1329, 1998.
- [78] PONCHAK, G. E., MAGOMENOS, A., and KATEHI, L. P. B., "Low Loss CPW on Low Resistivity Silicon Substrates with a Micromachined Polyimide Interface Layer for RFIC Interconnects," *IEEE Transaction on Microwave Theory and Techniques*, vol. 49, no. 5, pp. 866–870, 2001.
- [79] POPOV, E. P., *Mechanics of Materials, Second Edition*. Prentice-Hall Inc., 1976.
- [80] POZAR, D. M., *Microwave Engineering*. New York, NY: Wiley, 1998.
- [81] PULSFORD, N., "Passive Integration Technology: Targeting Small Accurate RF Parts," *RF Digest*, no. 11, pp. 8–40, 2002.
- [82] R. E. MIHAILOVICH AND M. KIM AND J. B. HACKER AND E. A. SOVERO AND J. STUDER AND J. A. HIGGINS AND AND J. F. DENATALE, "MEMS Relay for Reconfigurable RF Circuits," *IEEE Microwave Wireless Components Leter*, vol. 11, pp. 53–55, Feb. 2001.
- [83] RAMESHAM, R. and GHAFFARIAN, R., "Challenges in Interconnection and Packaging of Micromechanical Systems MEMS," in *IEEE Electronic Components and Technology Conf.*, pp. 666–675, May 2002.
- [84] RAMMAL, R., "Random walks of a particle on fractal lattices with traps," *Physical Letters*, vol. 102, no. 3, pp. 117–120, 1984.

- [85] RAUSCHER, C., “Reconfigurable Bandpass Filter with a Three-to-one Switchable Passband Width,” *IEEE Trans. on Microwave Theory Tech.*, vol. 51, pp. 573–577, 2003.
- [86] REBEIZ, G. M., *RF MEMS Theory, Design, and Technology*. New York: Wiley, 2003.
- [87] REBEIZ, G. M. and MULDAVIN, J. B., “RF MEMS Switches and Switch Circuits,” *IEEE Microwave Magazine*, vol. 27, pp. 59–71, Dec. 2001.
- [88] REBEIZ, G. M. and MULDAVIN, J. B., “RF MEMS Switches and Switch Circuits,” *IEEE Microwave Magazine*, vol. 12, pp. 59–71, 2001.
- [89] REICHL, H. and GROSSER, V., “Overview and Development Trends in the Fields of MEMS Packaging,” in *Proc. IEEE MEMS 2001 Conference*, pp. 1–5, 2001.
- [90] RIEH, J. S., “X and Ku band Amplifiers Based on Si/SiGe HBTs and Micromachined Lumped Components,” *IEEE Transaction on Microwave Theory Techniques*, vol. 46, no. 4, pp. 685–694, 1998.
- [91] RIEH, J. S., JAGANNATHAN, B., CHEN, H., SCHONENBERG, K. T., ANGELL, D., CHINTHAKINDI, A., FLORKEY, J., GOLAN, F., GREENBERG, D., JENG, S., KHATER, M., PAGETTE, F., SCHNABEL, C., SMITH, P., STRICKER, A., VAED, K., VOLANT, R., AHLGREN, D., FREEMAN, G., STEIN, K., and SUBBANNA, S., “SiGe HBTs with cut-off frequency of 350 GHz,” in *International Electron Devices Meeting Technical Digest*, pp. 771–774, Dec. 2002.
- [92] SANTOS, D. L., *Introduction to Microelectromechanical (MEM) Microwave Systems*. Boston, MA: Artech House Publishers, 1999.
- [93] SARKAR, S., PALAZARRI, V., WANG, G., PAPAGEORGIOU, N., THOMPSON, D., LEE, J. H., PINEL, S., TENTZERIS, E., PAPAPOLYMEROU, J., and LASKAR, J., “LCP and RF MEMS SOP Technology for Reconfigurable and Multi-band RF and mm-Wave Integrated Module,” in *IEEE MTT-S International Microwave Symposium Digest*, pp. 567–570, June 2004.
- [94] SCHPPEN, A., ERBEN, U., GRUHLE, A., KIBBEL, H., SCHUMACHER, H., , and KNIG, U., “Enhanced SiGe Heterojunction Bipolar Transistors with 160 GHz f_{max} ,” in *IEEE Intl. Electron Devices Meeting (IEDM ‘95) Tech. Dig.*, pp. 30.4.1–30.4.4, 1995.
- [95] SENTURIA, S., *Microsystem Design*. Kluwer Academic Publisher, 2001.
- [96] SHEN, S. C. and FENG, M., “Low Actuation Voltage RF MEMS Switches with Signal Frequencies from 0.25 GHz to 40 GHz,” in *Electron Devices Meeting, IEDM Technical Digest. International*, pp. 689–692, 1999.
- [97] SHI, F., “Dynamic Analysis of Micro-electro-mechanical Systems,” *Int. J. Number. Methods Eng.*, vol. 39, pp. 1119–1136, 1996.
- [98] SHIBATA, T. and SANO, E., “Characteristics of MIS Structure Coplanar Transmission Lines for Investigation of Signal Propagation in Integrated Circuits,” *IEEE Transaction on Microwave Theory and Techniques*, vol. 38, no. 7, pp. 881–889, 1990.

- [99] SMITH, J. K., “MEMS and Advanced Radar,” in *Antenna Applications Symposium*, Sept. 1999.
- [100] SORRENTINO, R., LEUZZI, G., and SILBERMANN, A., “Characteristics of Metal Insulator Semiconductor Coplanar Waveguide for Monolithic Microwave Circuits,” *IEEE Transaction on Microwave Theory and Techniques*, vol. 32, no. 4, pp. 410–416, 1984.
- [101] SPENGEN, M. V., PUERS, R., MERTENS, R., and DEWOLF, I., “A Comprehensive Model to Predict the Charging and Reliability of Capacitive RF MEMS Switches,” *J. Micromech. Microeng.*, vol. 14, p. 514, 2004.
- [102] SUGA, T., TAKAHASHI, A., HOWLANDER, M., SAIJO, K., and OOSAWA, S., “A Lamination Technique of LCP/Cu for Electronic Packaging,” in *2nd Intl. IEEE Conference on Polymers and Adhesives in Microelectronics and Photonics*, pp. 177–182, June 2002.
- [103] SUGA, T., TAKAHASHI, A., SAIJO, K., and OOSAWA, S., “New Fabrication Technology of Polymer/Metal Lamination and its Application in Electronic Packaging,” in *IEEE 1st Int. Polymers and Adhesives in Microelectronics and Photonics Conf.*, pp. 29–34, Oct. 2001.
- [104] T. ZHANG, W. JOHNSON, B. F. and LAWRENCE, M. S., “The Processing and Assembly of Liquid Crystalline Polymer Printed Circuits,” in *2002 Int. Symp. on Microelectronics*, pp. 177–182, 2002.
- [105] TAIT, R. N., “An IC Compatible Process for Fabrication of RF Switches and Tunable Capacitors,” *Journal of Elect and Comp. Eng.*, vol. 25, pp. 245–253, Jan. 2000.
- [106] TARNIJANI, A. A., DUSSOPT, L., and REBEIZ, G. M., “Miniature and Tunable Filters using MEMS Capacitors,” *IEEE Transaction on Microwave Theory Techniques*, vol. 51, pp. 1878–1885, July 2003.
- [107] THOMPSON, D., KINGSLEY, N., WANG, G., PAPAPOLYMEROU, J., and TENTZERIS, M. M., “RF characteristics of thin film liquid crystal polymer (LCP) packages for RF MEMS and MMIC integration,” in *IEEE MTT-S Int. Microwave Symp. Dig.*, pp. 857–860, June 2005.
- [108] THOMPSON, D., KIRBY, P., PAPAPOLYMEROU, J., and TENTZERIS, M. M., “W-band characterization of finite ground coplanar transmission lines on liquid crystal polymer (LCP) substrates,” in *IEEE Electronic Components and Technology Conf.*, pp. 1652–1655, May 2003.
- [109] THOMPSON, D. C., TANTOT, O., JALLAGEAS, H., PONCHAK, G. E., TENTZERIS, M. M., and PAPAPOLYMEROU, J., “Characterization of Liquid Crystal Polymer (LCP) Material and Transmission Lines on LCP Substrates from 30-110 GHz,” *IEEE J. MTT*, vol. 52, pp. 1343–1352, Apr. 2004.
- [110] THORNTON, J. A. and HOFMAN, D. W., “Stress Related Effects in Thin Films,” *Thin Solid Films*, vol. 171, pp. 5–31, Apr. 1989.
- [111] TILMANS, H., RAEDT, W. D., and BEYNE, E., “MEMS for Wireless Communications: from RF MEMS Components to RF MEMS SIP,” *J. Micromech. Microeng.*, vol. 13, pp. 139–163, 2003.

- [112] VANDERSHUEREN, J. and CASIOT, J., *Thermally stimulated relaxation in solids*. Berlin, Germany: Springer-Verlag, 1979.
- [113] VINOY, K. and VARADAN, V. K., “Design of Reconfigurable Fractal Antennas and RF-MEMS for Space-based systems,” *Smart Materials and Structures*, vol. 10, pp. 1211–1223, 2001.
- [114] WANG, G., BACON, A., ABDOLVAND, R., AYAZI, F., PAPAPOLYMEROU, J., and TENTZERIS, E., “Finite Ground Coplanar Lines on CMOS Grade Silicon with a Thick Embedded Silicon Oxide Layer Using Micromachining Techniques,” in *European Microwave Conferences*, pp. 25–28, Oct. 2003.
- [115] WANG, G., BARSTOW, S., JEYAKUMAR, A., PAPAPOLYMEROU, J., and HENDERSON, C., “Low Cost RF MEMS Switches Using Photodefinable Mixed Oxide Dielectrics,” in *IEEE MTT-S International Microwave Symposium Digest*, pp. 1633–1636, June 2003.
- [116] WANG, G., JEYAKUMAR, A., PAPAPOLYMEROU, J., and HENDERSON, C., “Photodefinable metal oxide dielectrics: A novel method for fabricating low cost rf capacitive mems switches,” in *Proceedings of 2003 Materials Research Society Fall Meeting*, vol. 783, pp. 91–96, Dec. 2003.
- [117] WANG, G., POLLEY, T., HUNT, A., and PAPAPOLYMEROU, J., “A High Performance Tunable RF MEMS Switch Using Barium Strontium Titanate (BST) Dielectrics for Reconfigurable Antennas and Phased Arrays,” *IEEE Antennas and Wireless Propagation Letters*, vol. 4, pp. 217–220, 2005.
- [118] WANG, G., THOMPSON, D., PAPAPOLYMEROU, J., and TENTZERIS, E. M., “Low Cost RF MEMS Switch Using LCP Substrate,” in *European Microwave Conferences*, pp. 1441–1444, Oct. 2004.
- [119] WANG, X., ENGEL, J., and LIU, C., “Liquid Crystal Polymer (LCP) for MEMS: Processes and Applications,” *J. Micromech. Microeng.*, vol. 13, pp. 628–633, Sept. 2003.
- [120] WEEDON, W., PAYNE, W., REBEIZ, G., HERD, J., and CHAMPION, M., “MEMS Switched Reconfigurable Multi-band Antenna: Design and Modeling,” in *Proceedings of the antenna applications symposium*, June 1999.
- [121] WEI, Z. and PHAM, A., “Liquid crystal polymer (LCP) for microwave/millimeter wave multi-layer packaging,” in *IEEE MTT-S Int. Microwave Symp. Dig.*, pp. 2273–2276, June 2003.
- [122] WIBBELER, J., PFEIFER, G., and HIETSCHOLD, M., “Parasitic Charging of Dielectric Surfaces in Capacitive Microelectromechanical Systems (MEMS),” *Sensors and Actuators A*, vol. 71, p. 74, 1998.
- [123] WU, H. D., HARSH, K. F., and IRWIN, R. S., “MEMS Designed for Tunable Capacitors,” in *IEEE MTT-S International Microwave Symposium Digest*, pp. 126–129, 1998.
- [124] X. WANG, L. L. and LIU, C., “Micromachining Techniques for Liquid Cystal Polymer,” in *14th IEEE Intl. Conf. on MEMS*, pp. 21–25, Jan. 2001.

- [125] YAO, J. J., “RF MEMS from a Device Perspective,” *J. Micromech. Microeng.*, vol. 10, p. 9, 2000.
- [126] YOUNG, D. J. and BOSER, B. E., “A Micromachined Variable Capacitor of Monolithic Low Noise VCOs,” in *Tech. Dig. 1996 Solid State Sensor and Actuator Workshop*, pp. 86–89, June 1996.
- [127] YOUNG, D. J. and BOSER, B. E., “A Micromachined Based RF Low Noise VCOs,” in *IEEE Custom Integrated Circuits Conference*, pp. 431–434, 1997.
- [128] YU LIU, *MEMS and BST Technologies for Microwave Applications*. PhD thesis, UNIVERSITY OF CALIFORNIA, Santa Barbara, 2002.
- [129] YUAN, X., CHEREPKO, S., HWANG, J., GOLDSMITH, C., NORDQUIST, C., and DYCK, C., “Initial Observation and Analysis of Dielectric Charging Effects of Capacitive Switches,” in *IEEE MTT-S International Microwave Symposium Digest*, pp. 1943–1946, June 2004.
- [130] ZHENG, G., *Low Power Reconfigurable Microwave Circuits using RF MEMS Switches for Wireless Systems*. PhD thesis, Georgia Institute of Technology, 2005.
- [131] ZHU, Y. and ESPINOSA, H. D., “Effect of Temperature on Capacitive RF MEMS Switch Performance a Coupled-Field Analysis,” *J. Micromech. Microeng.*, vol. 14, pp. 1270–1279, 2004.
- [132] ZOU, G., GRONQVIST, H., STARSKI, J. P., and LIU, J., “Characterization of liquid crystal polymer for high frequency system-in-a-package applications,” *IEEE J. ADVP*, vol. 25, pp. 503–508, Nov. 2002.
- [133] ZOU, G., GRONQVIST, H., STARSKI, P., and LIU, J., “High Frequency Characteristics of Liquid Crystal Polymer for System in a Package Application,” in *IEEE 8th Int. Advanced Packaging Materials Symp.*, pp. 337–341, Mar. 2002.